Distribution Agreement

In presenting this thesis or dissertation as a partial fulfilment of the requirements for an advanced degree from Emory University, I hereby grant to Emory University and its agents the non-exclusive license to archive, make accessible, and display my thesis or dissertation in whole or in part in all forms of media, now or hereafter known, including display on the world wide web. I understand that I may select some access restrictions as part of the online submission of this thesis or dissertation. I retain all ownership rights to the copyright of the thesis or dissertation. I also retain the right to use in future works (such as articles or books) all or part of this thesis or dissertation.

Signature:

_____ _____

Lewen Yang Date

Line tension assisted membrane permeation at the transition temperature in mixed phase lipid bilayers

By

Lewen Yang
Doctor of Philosophy

Chemistry

_____
James T. Kindt
Advisor

_____
Joel Bowman
Committee Member

_____
Michael C. Heaven
Committee Member

Accepted:

_____
Lisa A. Tedesco, Ph.D.
Dean of the James T. Laney School of Graduate Studies

_____
Date

Line tension assisted membrane permeation at the transition temperature in mixed phase lipid bilayers

By

Lewen Yang

Chemistry, Emory University, 2016
B.S. University of Science and Technology of China, 2010

Advisor: James T. Kindt

An Abstract of
A dissertation submitted to the Faculty of the James T. Laney School of Graduate Studies of Emory University in partial fulfillment of
the requirements for the degree of
Doctor of Philosophy in Chemistry

2016

ABSTRACT

Line tension assisted membrane permeation at the transition temperature in mixed phase lipid bilayers

This dissertation is focused on molecular dynamics simulation and the theoretical analysis of coarse-grain lipid models.

The permeability of lipid bilayers to a variety of permeants shows a peak at the transition temperature, when melting from an ordered gel phase to a disordered fluid phase. To explore this anomalous behavior, a five-site lipid membrane model that exhibits a phase transition upon expansion or compression was studied to determine how the permeation rate of a simple particle depends on the phase composition in the two-phase region and on particle size. For large permeants and system sizes, an anomalous behavior is found where permeability increases upon compression of the bilayer. By tracking the environment of each permeation event, and by normalizing the statistics to each phase's area fraction, we found that the permeation rate is not enriched in the interfacial regions, contradicting the prediction from the "leaky interface" hypothesis. However, as the ratio of the fluid phase went down, its local permeation rate was increased with a corresponding increase in the area per lipid. This result motivated a model for the decrease in effective permeability barrier through fluid phase domains arising from a decrease in the length of the gel/fluid interface at

the midpoint of a permeation event.

A specially-designed large permeant moving through the DPPC bilayer (represented by the MARTINI 2.0 model) was used to study the effect of line-tension-assisted membrane permeation. The umbrella sampling method has been used to evaluate the free energy profile for these permeation processes. At the lipid phase transition temperature, the permeation barrier for passage through an enclosed fluid domain embedded in a patch of gel was significantly lower than for passage through a fluid stripe domain. This difference in free energy barrier was produced from the interfacial free energy as there is a significant change in interfacial length due to the lipids' phase shift. The permeation through a fluid domain in a stripe geometry has a free energy barrier nearly identical to that of a gel-free fluid bilayer, when the phase shift is not accompanied by a change in the interfacial length. The interfacial line tension can be estimated to be between 10 and 13 *pN* from these two different systems. The permeation barrier was shown to drop even further in simulations performed at temperatures below the transition temperature. The results suggest a mechanism to explain the experimentally observed anomalous peak in the temperature-dependent permeability of lipid bilayers near their transition temperatures. The contribution of this mechanism toward the permeability of a gel phase containing a thermal distribution of fluid-phase domains is estimated using a simple statistical thermodynamic model.

The dynamics of the pore closure was studied under the permeant-free condition while using the same forcefield. The melting rate constant of the lipids at the transition temperature was estimated from a stripe system with approximately equal amount of the gel and fluid lipids, upon which the temperature is set to slightly deviated from the phase transition temperature. For the system of the fluid domain surrounded by gel, the pore size at a certain time can be shown to behave consistently with that of uniform fluid systems, by using the estimated melting rate constant and the value of interfacial line tension.

Line tension assisted membrane permeation at the transition temperature in mixed phase lipid bilayers

By

Lewen Yang

Chemistry, Emory University, 2016
B.S. University of Science and Technology of China, 2010

Advisor: James T. Kindt

A dissertation submitted to the Faculty of the James T. Laney School of Graduate Studies of Emory University in partial fulfillment of the requirements for the degree of Doctor of Philosophy in Chemistry

2016

Acknowledgement

I would like to express the deepest appreciation to Professor Kindt. He continually and convincingly conveyed a spirit of adventure in regard to research, and an excitement in regard to teaching. Without his guidance and persistent help this dissertation would not have been possible.

I would like to thank my committee members, Professor Bowman and Professor Heaven, who are dedicated in the academic field, for offering me valuable guidance with my research for years.

Finally, I would like to thank my parents and friends who are supportive to my Ph. D. career.

Table of contents

List of figures

List of tables

Chapter 1

General Introduction

1.1 Lipid membranes and lipid bilayers

Phospholipids, a major structural component of cell membranes,[1] are a group of naturally occurring molecules that contain both hydrophobic and hydrophilic parts.[2] They can be aggregated in an aqueous system because the polar heads of lipids align towards the water molecules while the hydrophobic tails minimize its contact with water and tends to cluster together, known as the "hydrophobic effect".[3] Depending on the concentration of lipids, the clustering can be in the form of micelles, vesicles (liposomes) or lipid bilayers.[4] A lamellar phase of lipid bilayers refers to sheets of bilayers separated by fluid. In this thesis, the dipalmitoylphosphatidylcholine (DPPC) bilayer has been extensively studied. The chemical structure of a DPPC molecule is shown in Figure 1. The zwitterionic property of this molecule is produced by the positively charged choline group and a negatively charged phosphate group. These head groups are connected to a glycerol backbone, which is also attached to two saturated palmitoyl chains (16 carbon chains).

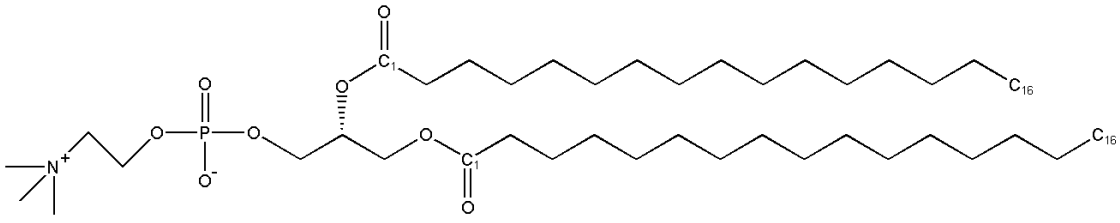

Figure 1. The structure of a dipalmitoylphosphatidylcholine (DPPC) molecule

1.2 Outline of this thesis

Lipids undergo phase transition at a certain temperature, in which the lipids melt from an ordered gel phase to a disordered fluid phase. As the temperature is increased through the phase transition range, the lipid permeability to a range of substances shows a peak instead of a continuous increase. Such an anomaly is explained by two main hypotheses. The first one is the “leaky interface” hypothesis which assumes that the interfacial regions between the gel and fluid domains is even more permeable than the bulk fluid phase. An alternative explanation relates the permeability anomaly to the lateral compressibility, which is also at its maximum around the phase transition range. The main goal of this thesis is to provide direct simulation proof to these hypotheses.

The distribution of the domain size and number around the phase transition temperature is critical in explaining the permeability anomaly. In the remaining part of the main introduction (chapter 1), the thermodynamics of the lipid phase transitions and the line tension of lipid bilayers will be introduced, and the relationship of these properties to the lipid domain size will be demonstrated. After that, I will present a detailed introduction of experimental findings and hypotheses to the lipid permeability peak around the phase transition, together with its clinical applications.

Since the literatures that provide direct simulation proof to the two hypotheses are scarce, the introduction will be focused on the ideas of how the coarse-grain simulations are set up. In the end, I will present several simulation methods that relate to this thesis.

In chapter 2, a simple coarse-grain model for membrane permeability will be introduced.[5] This five-site lipid model used Lennard-Jones interactions to retain gel-fluid phase transition behavior, and single-site permeants for the statistics of permeation rate.[5] The identification of the position of each permeation event (gel phase, fluid phase or interface) allows a direct test of the "leaky interface" hypothesis. After introducing several basic simulation methods, I will discuss the considerate detailed design of this model, the method for phase separation, the relationship between permeation rate and permeability, the size effect of both the lipid membrane and the permeant, and a new explanation towards the permeability anomaly in terms of the line tension.

In chapter 3, the new explanation is tested with the MARTINI force field, with a specially designed permeant. Since the reasoning is originated from intrinsic physical properties of membranes, it should not lose generality. I will first introduce the MARTINI force field and the design of the permeant in great details, and then discuss the simulation results and make extensive connections to the previous five-site

coarse-grained model. This includes the determination of T_m using a gel-fluid alternating stripe system, the investigation of permeability at different temperatures, and the confirmation of the model by extracting a line tension that agrees with other calculations.

In chapter 4, I will introduce atomistic simulations and 2d-umbrella sampling methods. Then, I will show the result of the translocation of a Na^+ across a DPPC bilayer. 2d-umbrella sampling is aimed at finding the true reversible reaction path for the sodium permeation. Although, our simulation has a much smaller simulation error compared with previous works[6] using 1d-umbrella sampling, a 20 *kJ/mol* hysteresis in the free energy barrier has been observed.

In chapter 5, the pore closure dynamics is studied with the MARTINI force field. Compared to chapter 2, the permeant free environment allows us to test the mechanisms more easily. I will first show the simulation results of a size-dependent study, followed by the dynamics of pore closure of a uniform fluid and an enclosed fluid domain surrounded by gel. A theory in terms of the free energy of line tension has been developed to explain the different dynamic behaviors between these two types of fluid.

1.3 Thermodynamics of lipid phase transitions

Lipid membrane melts from gel phase to liquid crystalline (fluid) phase at a certain temperature, which is called the phase transition temperature (T_m). Usually, such a transition is considered as the first-order phase transition. However, as the temperature gets near to the transition temperature from either side, there will be local fluctuations that look like the other phase. In other words, there will be transient gel-like micro-domains in the fluid phase and transient fluid-like micro-domains in the gel phase, at equilibrium.

In Figure 2, the phase transition behavior of DPPC bilayer is shown. Other than the gel and fluid phase, a ripple phase is also captured. The dilatometric measurements revealed a jump in molecular volume at 41-42°C, with a sudden change in heat capacity at the same temperature, captured by calorimetric measurements.[7] This latent heat is an indication of the main phase transition. Unless otherwise mentioned, the study of this thesis did not consider the ripple phase.

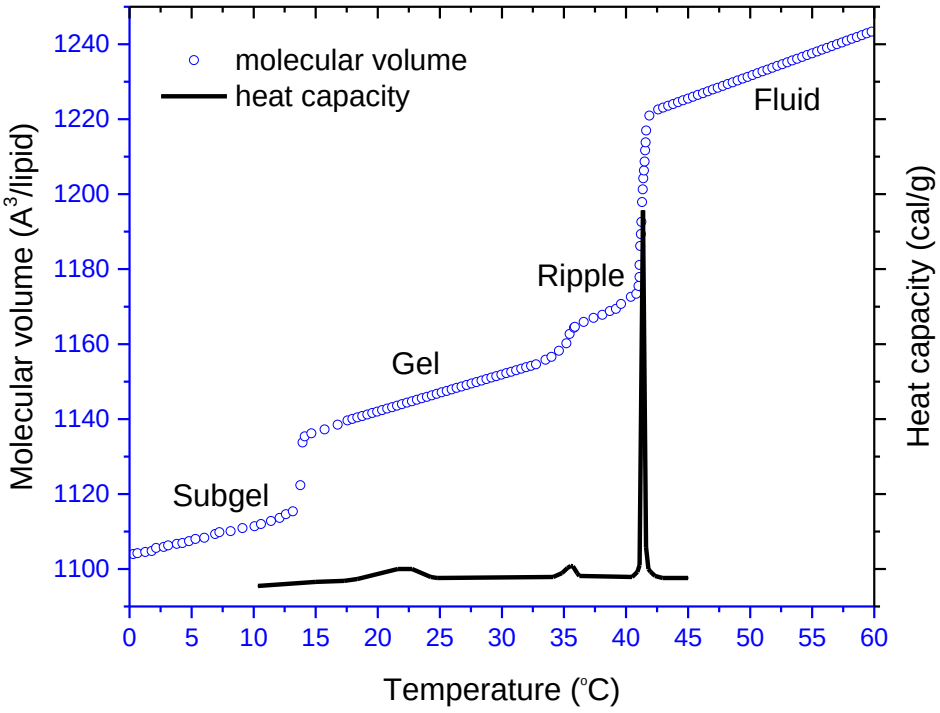

Figure 2. Molecular volume (circles) and heat capacity (solid line) vs. temperature for DPPC bilayers in excess water. (This figure is reproduced from reference[7].)

When the temperature is near T_m, some fraction of lipids in each phase will be in a microdomain of the other phase. Therefore, we choose to calculate the enthalpy per lipid of the gel-fluid transition (Δh), other than the total enthalpy change of a phase transition (ΔH), in an attempt to exclude these lipids. This can be achieved by choosing a small system, whose size prevents the formation of stable fluid-gel domains, and varying its initial conditions to form different ratios of gel phase lipids at T_m. Δh is then modeled as $\Delta h = \Delta H / \Delta N_{g-f}$, where ΔN_{g-f} is the number of lipid molecules that undergo phase shift.

Right at T_m, the free-energy cost to move a lipid from the gel phase to fluid phase is zero, since the chemical potential difference $\Delta\mu_{g\text{-}f}(T_m) = \mu_g(T_m) - \mu_f(T_m) = 0$, as must be true when the phases are at equilibrium. This is the same as $\Delta h - T\,\Delta s = 0$, where Δs and Δh are the entropy and enthalpy per lipid of the gel-fluid transition, respectively. Since we are only interested in a small temperature range near T_m, the estimate for $\Delta\mu_{g\text{-}f}(T)$ assumes that Δs and Δh do not change with temperature. When the temperature T is slightly deviated from T_m, $\Delta\mu_{g\text{-}f}(T)$ is estimated to be:

$$\Delta\mu_{g-f}(T) = \Delta s \cdot (T - T_m) = \frac{\Delta h}{T_m}(T - T_m) \quad (1)$$

Thus, the free energy cost for a total of N lipids to undergo phase transition can be estimated as: $\Delta G = \Delta\mu_{g-f}(T) \cdot N$.

1.4 Line tension of lipid bilayers

The thermodynamic line tension is defined as the free energy cost of formation per unit length of a new linear interface: $\tau = -\frac{\partial F}{\partial l}$. The line combining different surfaces will have different values. In simulations, a ribbon-like membrane can be used to estimate the line tension using the pressure tensor.[8] Consider a ribbon membrane in which its surface normal is along z direction, and the membrane-water interface is along y direction, the line tension can be calculated as:[8]

$$\tau = \frac{1}{2}\langle L_x L_z [\frac{1}{2}(P_{xx} + P_{zz}) - P_{yy}]\rangle \quad (2)$$

Where L_x and L_z are the box dimensions of x and z direction, and P_{xx}, P_{yy} and P_{zz} are the diagonal elements of the pressure tensor. For this thesis, we are interested in two types of line tensions. One is the line tension between the lipid gel domain and fluid domain which we will denote as Λ; the other is the line tension between the fluid phase bilayer and the solvent (water), usually being referred to "edge tension", noted as τ.

1.5 Critical domain size

Suppose the temperature T is slightly below T_m, we can derive the critical domain size above which a gel phase is kinetically stable, when nucleating within bulk fluid. For simplicity, assuming a circular domain with radius R, the interfacial free energy is $\Lambda \cdot 2\pi R$. The free-energy penalty in terms of chemical potential is: $\Delta\mu_{g-f}(T) \cdot \Delta N_g = \Delta\mu_{g-f}(T) \cdot 2\pi R^2/a_g$, where a_g is the area per lipid of the gel phase. Therefore, the total free energy has the form:

$$G = \Lambda \cdot 2\pi R + \Delta\mu_{g-f}(T) \cdot 2\pi R^2/a_g \tag{3}$$

By setting $\frac{dG}{dR} = \Lambda \cdot 2\pi + \Delta\mu_{g-f}(T) \cdot \frac{4\pi R}{a_g} = 0$, $R_c = -\frac{1}{2} \cdot \frac{\Lambda \cdot a_g}{\Delta\mu_{g-f}(T)}$. Here, $\Delta\mu_{g-f}(T) < 0$ since the temperature is lower than T_m. Therefore, when the radius of the gel domain gets bigger than R_c, the overall free energy will continue to favor its growth.

1.6 The permeability of lipid bilayers

The method to obtain experimental membrane permeability usually includes NMR, osmotic measurements, and radio-tracer experiments.[9-11] The reported value has a rather broad range, due to the different temperatures and different estimations on membrane area. For the permeability coefficient of water, the reported value is 6.32×10^{-4} cm/s at 315 K,[12] and 1.7×10^{-3} cm/s at 317 K,[13] using the osmotic measurements on DPPC vesicles. Osmotic measurements on black film for EggPC membrane yield 4.2×10^{-3} cm/s at 309 K,[14] $(7\text{-}10) \times 10^{-3}$ cm/s at 309 K,[15] and 3.7×10^{-3} cm/s at 298 K.[16] According to Fick's law, the permeability can be written as:

$$P = \frac{dn/dt}{\Delta C \cdot A_{tot}} \tag{4}$$

where dn/dt is the total unidirectional crossing rate, ΔC is the effective permeant concentration and A_{tot} is the total area of the membrane surface.

There are several models to describe the permeation processes through lipid membranes. The first is homogeneous solubility-diffusion model.[17-18] It treats the membrane as a homogeneous phase with well-defined boundaries, separating it from the water phase. In this model, to facilitate the permeation process, the molecule must first dissolve into the membrane, then diffuses through the membrane interior, and finally should dissolve again into the water phase. This model is good at describing the permeation processes of small molecules such as water.[19] Usually, the insertion of these small molecules will not induce a distinct distortion to the bilayer. The

permeability of the molecule across the bilayer (P) is given by:

$$P = \frac{KD}{d} \tag{5}$$

Where K is the permeant partition from aqueous to organic phase, D is the diffusion coefficient of this permeant within the bilayer and d is the thickness of the bilayer. In most cases, this model is oversimplified by assuming an isotropic and homogeneous environment of the membrane interior, and a sharp boundary between the water and membrane phase.

A more widely used model is the inhomogeneous solubility-diffusion model.[19] Comparing to the previous model, the permeability has to take an integrated form along the membrane surface normal. Assuming the normal direction is z and z = 0 corresponds to the bilayer center, the permeability can be written as:[20]

$$P = \left[\int_{-\frac{d}{2}}^{\frac{d}{2}} \frac{1}{K(z)D(z)}\, dz\right]^{-1} \tag{6}$$

Where d is the thickness of the bilayer, $K(z)$ and $D(z)$ are the partition function and diffusion coefficient at a given z position, respectively. The permeability is usually calculated using the potential of mean force method.[20] By constraining the permeant at a given z position, the force exerted on it $F(z,t)$ can be computed. Using the force autocorrelation function, $D(z)$ in equation (6) can be written as:

$$D(z) = \frac{(RT)^2}{\int_0^\infty \langle \Delta F(z,t) \Delta F(z,0) \rangle\, dt} \tag{7}$$

Where R is the gas constant, T is temperature, <> denotes the average, and

$\Delta F(z,t) = F(z,t) - \langle F(z,t)\rangle$. *K(z)* can be computed through:

$$K(z) = exp\left[\frac{-\Delta G(z)}{k_B T}\right] \quad (8)$$

$$\Delta G(z) = -\int_{|z|>\frac{d}{2}}^{z} \langle F(z',t)\rangle \, dz' \quad (9)$$

Where ΔG is the potential of mean force, k_B is the Boltzmann factor, and $\langle F(z',t)\rangle$ is the average force over time. A limitation of this model is that the reaction coordinate is assumed to be along the membrane normal. It will not account, for instance, for barriers to reorientation of the permeant or the lipids that might accompany the translation along the normal.

An advanced theory that addresses these issues is the milestoning algorithm.[21-25] It estimates the overall kinetics and thermodynamics of a complex system by accumulating short time trajectories. The advantage that it is not limited by one-dimensional coordinate allows for the study of large permeants whose permeation processes often involves rotational or internal motions of the permeant or complex rearrangements of the lipids. A milestoning calculation first identifies anchors, which are the sets of points in phase space that coarsely cover the accessible configurations and momenta for the system. Milestones are the directional interfaces that separate anchors. By estimating the fluxes through these interfaces, one can estimate the stationary probabilities, which correspond to the free energy profile.[26] Milestoning is a kinetic model in which the transitional trajectories are computed explicitly. This is different from the inhomogeneous diffusion model which estimates the local diffusion

coefficient for the overdamped system through the integration of a force at this position that is thermodynamically averaged, as indicated in equation (6) and (7).

1.7 Liposome technology in drug delivery

As the first closed phospholipid shells (liposomes) were proposed as a drug delivery agent back in 1965, researchers have devoted great efforts and advanced clinically applicable drug delivery systems, such as ligand-targeted liposomes, long-circulating liposomes and triggered release liposomes,[27] some of which have already been matured clinically. For example, Doxil, is the anti-cancer drug doxorubicin[28] encapsulated in a closed lipid sphere. The outer lipid shell can be made to be thermosensitive, which is the case for ThermoDox,[29] an anti-cancer drug developed by Celsion corporation. Its outer shell contains a small portion of lysolipids together with dipalmitoylphosphatidylcholine (DPPC) lipids. The Lyso-Thermosensitive Liposomal Doxorubicin (LTLD) can be rapidly released at 39-42 °C, with hyperthermia treatment[30-31] at the targeted tumor sites. The high concentration of drugs can be localized at affected spots and leaving normal tissues unimpaired. It is due to the rapid increase in the permeability of the lipid shell under a temperature range that triggers the lipids' phase transition.

1.8 Permeability anomaly during phase transition

DPPC, the main liposomal lipid in ThermoDox, has a T_m of 41 °C, which is just 4 °C above the body temperature.[32-33] An interesting and important phenomenon that relates to the LTLD development is that the lipid permeability to a range of water-soluble substances showed a peak, instead of a monotonous increase, as the temperature is increased over the range of T_m.[34] The magnitude of this permeability peak is dependent on both the permeant and the type of lipids, according to previous experimental studies on lipid vesicles.[35] For instance, the permeation rate of ions or polar molecules tends to have a distinct peak with temperature. This includes Na^+,[34, 36] Rb^+,[37] ANS (8-anilino-1-naphthalenesulfonate),[38] and others.[39-41] Several other types of molecules only show a continuous increase during the gel to fluid phase transition, such as water,[42] tetracycline, and pyrene.[38]

Through theoretical studies on this issue, two main explanations have been proposed for the permeability anomaly. The "leaky interface" model suggests that the local permeability of the interfacial region between the gel and fluid domains (interface), is much greater than that of either bulk phase.[34, 39] Such an explanation is supported by another independent simulation of chain-melting transition using a simple lattice model.[43] By assigning different local permeation rate at gel domains, fluid domains and interfaces, the total permeation rate can be fit with experimental values at different temperatures.[43] When assuming the interface has a local permeability that is approximately 10 times larger than that of fluid phase, the gel-fluid boundaries

lengths are well-correlated with experiments.[43] The other explanation relates such a permeability peak to the lateral compressibility peak of the bilayer, also appeared at $T = T_m$.[44] It can be proven thermodynamically, that the area density fluctuation reaches its maximum at the compressibility peak position.[44-45] As both explanations yield good fits to the same experimental data, the mechanism is still debatable after decades due to a lack of direct evidence in simulations of "leaky interface", or the implicit connection between the area fluctuations and permeability.

1.9 The approach of this thesis

In this thesis, we describe computational studies on lipid membrane systems that undergo gel-fluid phase transition. More precisely, we run molecular dynamics (MD) simulations to elucidate the mechanism of membrane permeability anomaly during the phase transition region. A MD simulation numerically solves Newton's equations of motion for a system of interacting atoms or molecules, where forces between the particles are determined by inter-atomic potentials. Commonly, we use two descriptions: atomistic simulations or coarse-grain simulations. Atomistic simulations can model the biological molecule at the level of atoms. Course-grain simulations, developed for investigating longer time or larger scale dynamics, replace an atomistic description of a molecule with a lower-resolution coarse-grained model that smoothes away fine details.

To provide direct evidence to either of the hypotheses, atomistic simulations are extremely challenging. For example, the T_m of a stable two-phase system of a one component lipid membrane is difficult to calculate to high precision.[46] Also, the rate of nucleation and growth of a new phase near T_m is much slower than the typical simulation time scale (hundreds of nanoseconds).[47-48] Therefore, it is impossible to sample the equilibrium distribution of domain sizes and shapes, not to mention to localize permeation events. Even for a uniform fluid phase lipid, it requires microseconds long trajectories to assess the permeation rate of water molecules,[49] and much longer for ions or large polar molecules. A more applicable atomistic approach to test the "leaky interface" hypothesis may be to use biasing techniques to calculate the free-energy barrier of permeation as a function of distance from a gel-fluid interface. However, the typical precision obtained for barrier height is 2-4 kJ/mol,[50] not sufficient enough to resolve the differences of interest. Also, the interface position may not remain still during the simulation. Last but not least, the kinetic prefactor[19] may also account for the difference in permeation rate.

For the above reasoning, a coarse-grain simulation is more promising. Fortunately, the apparent generality of this phenomenon suggests that the fine details of molecular interactions may not be essential to explain it. Such an approach has been performed by Winter and Schatz, using the MARTINI coarse-grained force field, to address the permeability anomaly.[51] They found a peak in solvent permeability at the phase

transition when a single-tailed lysolipid was incorporated within the DPPC bilayer, but not for the pure DPPC.[51-52] The presence of this peak was attributed to the increased free volume fraction in the bilayer induced by the lysolipid.[51] Although, the MARTINI force field simulations are 3-4 orders of magnitude faster than atomistic simulations,[53] it is still not sufficient to sample good statistics of permeation rate.

1.10 Simulation methods

1.10.1 Stochastic Langevin dynamics

Stochastic Langevin dynamics adds a friction and a noise term to Newton's equations of motion. Considering the i^{th} particle with mass m_i and position vector $\boldsymbol{r}_i$, the equation of motion has the form of:

$$m_i \frac{d^2\boldsymbol{r}_i}{dt^2} = \boldsymbol{F}_i(\boldsymbol{r}) - m_i\gamma_i \frac{d\boldsymbol{r}_i}{dt} + \boldsymbol{R}_i(t) \tag{10}$$

where γ_i is the friction constant, and $R_i(t)$ is a noise process (with zero means) that satisfies: $\langle R_i(t)R_i(t+s)\rangle = 2m_i\gamma_i k_B T\delta(s)\delta_{ij}$, where k_B is the Boltzmann constant, T is temperature, and $\delta(s)$ is the Dirac delta function. In the high friction limit, the stochastic dynamics is reduced to Brownian dynamics:

$$\frac{d\boldsymbol{r}_i}{dt} = \frac{1}{\gamma_i}\boldsymbol{F}_i(\boldsymbol{r}) + \boldsymbol{r}_i(t) \tag{11}$$

where $r_i(t)$ is a noise process that satisfies: $\langle r_i(t)r_i(t+s)\rangle = 2k_B T\delta(s)\delta_{ij}/\gamma_i$.

1.10.2 Temperature coupling method

The temperature control is of great importance in molecular dynamics studies because

most quantities we wish to calculate are coming from constant temperature ensemble, instead of a NVE (constant number, constant volume and constant energy) ensemble. One of the temperature control is the Berendsen temperature coupling.[54] Given a desired temperature T_0, a deviation of the systems temperature is slowly corrected as:

$$\frac{dT}{dt} = \frac{T_0 - T}{\tau} \tag{12}$$

Which states that the temperature deviation decays exponentially with a time constant τ. Although Berendsen temperature coupling allows fast equilibration processes, the fluctuation of the kinetic energy is suppressed. In other words, the Berendsen thermostat does not generate a correct canonical ensemble.

To solve this problem, a velocity rescaling thermostat[55] is used in this study. A time dependent factor λ is used control the system's heat flow, by scaling the velocities of each particle every n_c step.

$$\lambda = \sqrt{1 + \frac{n_c \Delta t}{\tau_T}\left[\frac{T_0}{T(t - \frac{1}{2}\Delta t)} - 1\right]} \tag{13}$$

Where Δt is the time step, and τ_T is the time constant which is related to the Berendsen temperature coupling time constant τ through the following equation:

$$\tau_T = \frac{\tau k_B N_f}{2C_v} \tag{14}$$

where k_B is the Boltzmann's constant, N_f is the total number of degrees of freedom, and C_v is the total heat capacity of the system. We could relate λ to the kinetic energy K, and the kinetic energy at the targeted temperature ($\overline{K} = N_f T_0/2k_B$) through the

following equation:

$$\lambda = \sqrt{\frac{\overline{K}}{K}} \tag{15}$$

However, for the actual thermostat, a stochastic process is involved and $\overline{K}$ is modified to K_t which is drawn from the canonical equilibrium distribution for kinetic energy:

$$\bar{P}(K_t)dK_t \propto K_t^{(\frac{N_f}{2}-1)} e^{-\beta K_t} dK_t \tag{16}$$

Such an approach ensures the correct kinetic energy distribution.

$$dK = (K_0 - K)\frac{dt}{\tau_T} + 2\sqrt{\frac{KK_0}{N_f}}\frac{dW}{\sqrt{\tau_T}} \tag{17}$$

Where *K* is the kinetic energy, and *dW* is a stochastic Brownian motion process.

1.10.3 Pressure coupling methods

Similar to temperature coupling, the system's pressure can be controlled by coupling to a "pressure bath". The methods used in this work is Berendsen pressure coupling. Given a referenced pressure $\boldsymbol{P}_0$, the coordinates and box vectors are rescaled so that the corresponding pressure $\boldsymbol{P}$ has a first-order relaxation towards it.

$$\frac{d\boldsymbol{P}}{dt} = \frac{\boldsymbol{P}_0 - \boldsymbol{P}}{\tau_p} \tag{18}$$

The Berendsen pressure can be done isotropically, semi-isotropically and anisotropically. The most commonly used one is anisotropic pressure coupling, which allow the box dimensions to scale independently.

1.10.4 Free-energy calculations

The umbrella sampling[56-57] and weighted histogram analysis method (WHAM)[58] were used for free energy calculations. In molecular dynamics runs using canonical ensemble, a system in which the configurations are separated by a high-energy barrier may suffer from poor sampling. Umbrella sampling greatly improves the sampling of the inaccessible configurations and provides a method to "bridge the energy gap". The common case is accomplished by applying external harmonic potentials at different positions. Usually such a harmonic potential can cause a sufficient bias of the free energy, but still maintains a relatively broad distribution width. For each umbrella sampling simulation, the plot of the harmonic-potential-biased distribution is called an umbrella histogram. An umbrella histogram should overlap with its neighbors to ensure sufficient sampling of all positions. In the study of this thesis, a series of harmonic potentials was applied with their minima distributed along the bilayer surface normal (z direction). The permeant's z position was defined as the Z coordinate of the center of mass of the permeant, relative to that of the DPPC bilayer ($z = 0$).

The WHAM algorithm gives an optimized estimate on the unbiased probability distribution based on all the umbrella histograms.[59] The full expressions for WHAM are:[60]

$$p(z) = \frac{\sum_{i=1}^{N} h_i(z)}{\sum_{j=1}^{N} n_j f_j \ exp[-\beta \omega_j(z)]} \tag{19}$$

$$\frac{1}{f_j} = \sum_z p(z)\, exp\left[-\beta\omega_j(z)\right] \tag{20}$$

where N is the total number of umbrella histograms used, $p(z)$ is the unbiased probability distribution, $\omega_j(z) = \frac{1}{2}K_j(z - z_j)^2$ is the biasing potential, $h_i(z)$ is the number of data points of histogram i at position z, n_j is the total number of data points of histogram j and f_j is a normalization factor for the biased probability distribution of the j^{th} simulation. The WHAM equations should be solved iteratively until reaching self-consistency. After solving $p(z)$, the free energy curve can be constructed by choosing the center of solvent layer z_0 as the reference position:

$$\Delta G(z) = G(z) - G(z_0) = -k_B T \cdot ln\frac{p(z)}{p(z_0)} \tag{21}$$

Chapter 2

The five-site lipid model*

When a range of lipid bilayers are melted to the disordered fluid phase from the (much less permeable) ordered gel phase, their permeability to a variety of permeants shows a peak at the transition temperature and drops off with increasing temperature, rather than just rising as melting proceeds. To explore this anomalous behavior, a simulated coarse-grained lipid membrane model that exhibits a phase transition upon expansion or compression was studied to determine how the permeation rate of a simple particle depends on the phase composition in the two-phase region and on particle size. The permeation rate and each phase's area fraction and area density could be directly calculated, along with the probability that the permeant would cross in either phase or at interfacial regions. For large permeants and system sizes, conditions could be found where permeability increases upon compression of the bilayer. Permeation was negligible in the gel phase and, in contrast to the predictions of the "leaky interface" hypothesis, was not enriched in interfacial regions. The anomalous effect could instead be attributed to an increase in the area per lipid of fluid phase domains. This result motivated a model for the decrease in effective permeability barrier through fluid phase domains arising from a decrease in the length of the gel/fluid interface at the midpoint of a permeation event.

* Adapted from reference [5].

2.1 Backgrounds

A long-term goal of experimental and computational studies of lipid bilayers has been the elucidation of permeabilities for a range of ions or molecules.[19, 35, 61-63] One particular topic of interest in this field is the permeability anomaly during the lipid phase transition region.[35] As the temperature is increased over the range of the gel to liquid-crystalline (fluid) phase transition, the permeability of phospholipid bilayers towards a range of water-soluble substances may present a peak at the main phase transition temperature (T_m).[34] This phenomenon has found a recent application in the development of temperature-sensitive liposomes for drug delivery.[31] The concept is that a vesicle composed of a lipid bilayer whose T_m is only several degrees above body temperature[32] can be used to direct the release of an encapsulated drug at the targeted positions using localized heating.[30-31] Aside from the clinical application, many experiments have been performed to study the magnitude of the permeability peak in lipid vesicles, which is dependent on both the permeant and the type of lipids.[35] A distinct peak at T_m in the temperature-dependent permeability could be found during the permeation of ions or polar molecules, such as Na^+,[34, 36] Rb^+,[37] and ANS (8-anilino-1-naphthalenesulfonate),[38] etc.[39-41] Some other types of molecules only show a continuous increase during the transition from gel to fluid phase, such as water,[42] tetracycline, and pyrene.[38]

Two main hypotheses have been advanced to explain the permeability peak. The

"leaky interface" model suggests that the interfacial region between the gel and fluid domains, which coexist only at temperatures near T_m, is more permeable than either bulk phase.[34, 39] Support for this explanation could be found in the simulation of a chain-melting transition using a simple lattice model, where the fluid-gel boundary lengths were well-correlated with experimental permeabilities.[43] Alternatively, the permeability peak has been attributed to the maximum observed in the lateral compressibility of the bilayer at $T=T_m$, and the accompanying maximum in area fluctuations, whose dependence on the compressibility is dictated by thermodynamic principles.[44-45] As both explanations are reasonable, and both have yielded remarkably good fits to the same experimental data set, the challenge remains to settle the question in favor of one or the other - or perhaps to find an explanation that reconciles features of both.

Given the debate about its mechanism, simulation studies using a molecular model for the bilayer could be helpful to understand and illustrate this phenomenon. Such an undertaking faces considerable challenges. Setting up a stable two-phase system in an atomistic simulation is difficult given that even the transition temperature is difficult to calculate to high precision.[46] The slow rate of nucleation and growth of new phases near T_m (slower than the typical simulation timescale of 100's of nanoseconds[47-48]) makes sampling of an equilibrium distribution of domain sizes and shapes difficult. Even for a single-phase fluid bilayer, direct calculation of permeation rates from an

atomistic MD simulation for as small and plentiful a permeant as water requires microsecond-long trajectories.[49] Much longer simulations would be needed to assess permeation rates for ions or large polar molecules. The leaky interface hypothesis could be tested in principle by calculating free energy barriers to permeation as a function of distance from a gel-fluid interface (using *e.g.* umbrella sampling methods). There are several foreseeable complications to this approach: the precision typically achieved in the barrier height (± 2-4 kJ/mol[50]) may not be sufficient to resolve the differences of interest; the location of the interface might not remain fixed over the sampling; and even if the free energy barriers can be established, further steps to reach an approximation of the kinetic prefactor[19] would be needed to obtain a rate.

For all these reasons, a computationally inexpensive model is useful. Fortunately, the apparent generality of the phenomenon suggests that specific details of molecular interactions may not be essential to explain it, particularly if the explanation lies in the thermodynamics of area fluctuations. In the only (to our knowledge) simulation work addressing the permeation anomaly using off-lattice simulations, Winter and Schatz performed a simulation using the MARTINI coarse-grained forcefield and found a peak in permeability to solvent at the phase transition when a single-tailed lysolipid was incorporated within the DPPC bilayer,[51-52] but not for the pure DPPC membrane. The peak's presence was attributed to the increased free volume fraction in the bilayer in the presence of the lysolipid.[51]

In the present study, an even simpler model was used. Each lipid molecule is represented by a chain of five sites whose ends are restrained to parallel planes, forming a single-layer membrane. (As the major hypotheses discussed above are based on phenomena that do not depend on the existence of a two-leaflet structure, a single-layer model was adopted for simplicity.) Single-site permeant molecules are kept near the membrane under a weak harmonic restraint in order to facilitate better sampling of permeation events. Simulations were performed over a range of fixed areas, spanning an ordering transition. Results from this study show a type of anomalous behavior: permeability passes through a peak as the system is compressed or expanded through the two-phase region at constant temperature. Identifying the locations of permeation events allows for a test of the “leaky interface” hypothesis. Careful examination of changes in the local area density of the fluid phase points to a different explanation for the anomaly within the simulation model. The insights drawn from the simulation results, while not enough to settle the question of a general origin for the anomaly, lead to a simple way to predict an enhancement to the permeability through a fluid domain embedded within a gel, driven by the interfacial line tension between the two phases.

2.2 Simulation methods

2.2.1 Two-phase system construction

In this model system (Figure 3), lipids are represented by a group of neutral, five-site molecules. Molecular dynamics simulations were performed using Gromacs[64] version 4. The stochastic Langevin molecular dynamics method[65] was used to maintain a fixed temperature in the constant NVT ensemble and to mimic the drag and thermalization effects of solvent on the permeant. Numerical values for all potential parameters discussed below, as well as the integration timestep and the coupling time associated with the Langevin thermostat, are given in Table 1. Values are presented in terms of both reduced units (based on the lipid site-site Lennard-Jones radius σ^*, the thermal energy k_BT, the particle mass m^*, and the reduced time unit $t^*=\sigma^*\cdot[m^*/(k_BT)]^{1/2}$) and in the explicit units used to set up Gromacs calculations (σ^*=0.4 nm, ε^* =1 kJ·mol^{-1}, m^*=14.03 amu).

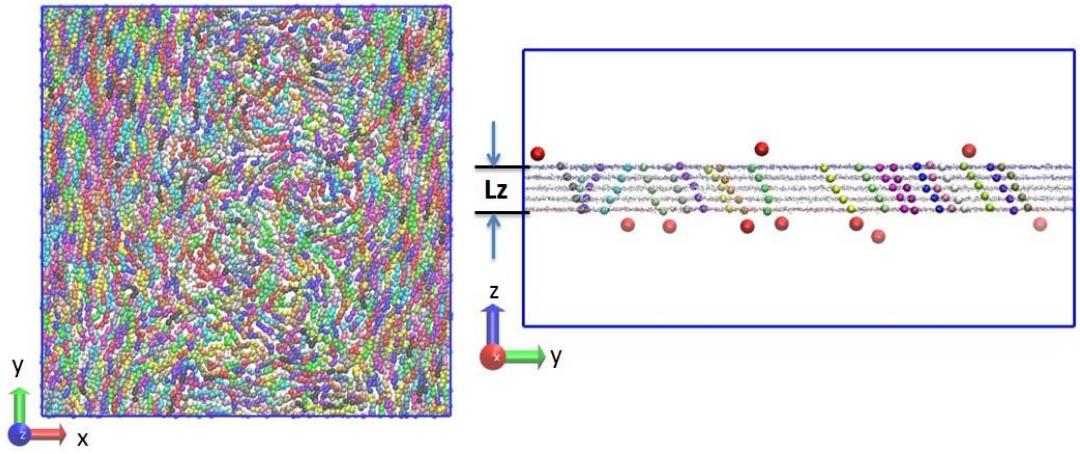

Figure 3. Top view (left) and side view (right) of the model system following equilibration at a lipid area density of 0.728 $(\sigma^*)^{-2}$. Permeants are depicted as red spheres. Lipid sites are colored according to molecule to distinguish one from another. Snapshots of several molecules are shown on the side view, with less ordered ones on the left side and ordered ones on the right side.

Harmonic potentials with force constant K_{bond} and K_{angle} were used to restrain all bonds and angles close to r_{bond} and θ_0, respectively. The simplicity of the lipid interactions and the absence of solvent meant that external restraint potentials were needed to maintain a planar membrane structure. The first and the last atom of each molecule were restrained through strong harmonic potentials of force constant K_{strong} to the planes z=0.5 L_Z and z= -0.5 L_Z, respectively, as:

$$U_{restraint}(z) = \frac{1}{2} K_{strong}(z \pm 0.5L_z)^2 \quad (22)$$

Restraining the Z position of the lipids at both ends enforces a monolayer structure of thickness L_z with flat interfaces on both sides and with its midplane coinciding with z=0. The thickness was set to L_Z=4·r_{bond}·cosθ_{tilt}, where the optimized tilt angle θ_{tilt} for a fully extended chain with respect to the membrane surface normal is 32˚, the same as the experimental tilt angle of the DPPC molecule in the $L_{\beta'}$ gel phase.[66] Restraining both ends rather than one end of the lipid molecules prevented unpredictable lipid behaviors (either an uniform 1:1 distribution of lipids above and below the plane, or some domains forming above and some below) that would be likely to introduce complications. The choice of a high value for K_{strong}, which suppresses undulations and thickness fluctuations in the membrane, was made because weaker constraints were found to shift the phase transition discussed below to higher lipid area densities. At these higher densities, permeation events were too infrequent to evaluate permeation rates with confidence and precision.

The initial simulation structures were created from a regular hexagonal array of perfectly straight chains at a number density of $0.92(\sigma^*)^{-2}$ with a tilt angle of 32°. For the standard system size of $50\sigma^* \times 50\sigma^*$, the initial packing consisted of 2304 chains (Figure 4a). A randomly selected subset of molecules was then removed to give the desired density of the system (Figure 4b). This random selection was performed independently for each density point.

(a)

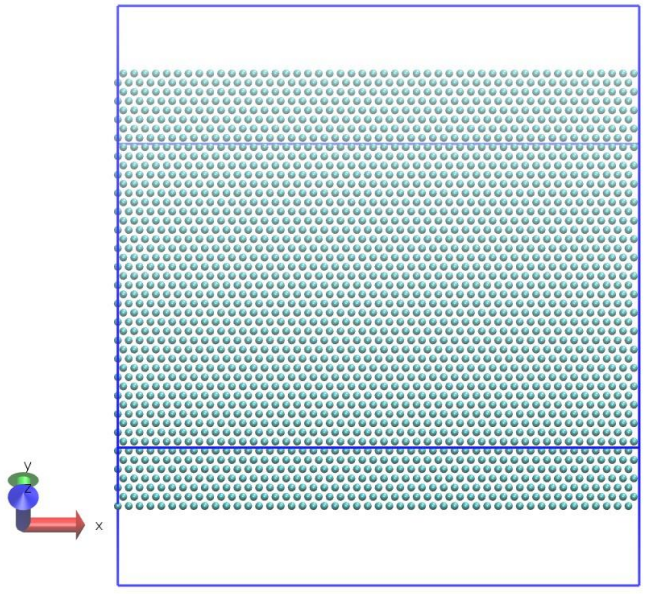

(b)

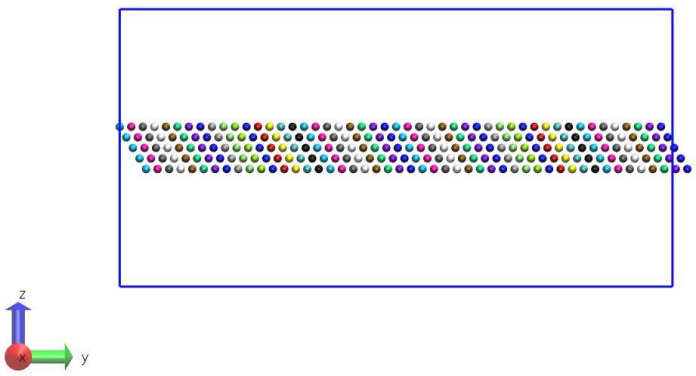

Figure 4. The tilted-angle view (a) and side view (b) of the engineered gel structure. In this example, the packing consists of 2304 chains.

Over the course of an equilibration period of $3.338\times10^4 t^*$, lipids rearranged into regions of high area density, orientational and packing order (similar to a gel phase) and regions of lower density with lower orientational and packing order (similar to a fluid phase). Trajectory lengths of $6.341\times10^5\, t^*$ (950 ns) were used for simulations at the standard system area; for investigation of system size effects with $25\sigma^*\times25\sigma^*$ and $100\sigma^*\times100\sigma^*$ boxes, trajectory lengths of $3.338\times10^5 t^*$ ($500ns$) and $1.669\times10^5 t^*$ ($250ns$) were used, respectively.

Permeants are represented by neutral single-site molecules. Non-bonded interactions among lipid and permeant sites are represented through Lennard-Jones (L-J) potentials. The L-J radius σ of the permeant atoms is set slightly larger than that of the lipid atoms; several size ratios were studied. The attractive r^{-6} term of the L-J interaction between two permeant atoms has been excluded to prevent permeants from clustering. The L-J attraction is switched smoothly to zero over the range $2\sigma^*$ to $2.5\sigma^*$. Each permeant is subject to an additional weak external harmonic potential of force constant K_{weak},

$$U_{weak}(z) = \frac{1}{2} K_{weak} z^2 \tag{23}$$

This potential allows permeants to move away from close contact with the lipids and to freely diffuse parallel to the membrane plane, while preventing them from diffusing

too far away from the bilayer and from crossing the periodic boundary normal to the bilayer. Solvent is not represented explicitly.

Potentials between:	Gromacs Unit	Reduced unit (σ^*, ε^*, m^*, t^*)
two lipid sites	σ = 0.4 *nm*, ε = 1 $kJ{\cdot}mol^{-1}$	σ = 1, ε = 1
a permeant site and a lipid site	σ = 0.5 *nm*, ε = 1 $kJ{\cdot}mol^{-1}$	σ = 1.25, ε = 1
two permeant sites	σ = 0.5 *nm*, ε = 1 $kJ{\cdot}mol^{-1}$	σ = 1.25, ε = 1
A_{tot}	400 nm^2	2500
L_Z	1.523 *nm*	3.808
Time step (*dt*)	0.01 *ps*	6.675×10^{-3}
r_{bond}	0.4490 *nm*	1.112
K_{bond}	121.2 $kJ{\cdot}mol^{-1}{\cdot}nm^{-2}$	19.39
θ_0	180˚	180˚
K_θ	12.12 $kJ{\cdot}mol^{-1}{\cdot}rad^{-2}$	12.12
K_{strong}	830 $kJ{\cdot}mol^{-1}{\cdot}nm^{-2}$	132.8
K_{weak}	3 $kJ{\cdot}mol^{-1}{\cdot}nm^{-2}$	0.48
Temperature (*T*)	200 *K*	1.662
Thermostat time constant (τ)	2 *ps*	1.335

Table 1. Parameters of the model system.

2.2.2 Calculating the permeation rate

The following protocol was used to define a crossing (permeation) event. If a permeant enters the membrane and reaches the center line (Z = 0), a crossing event is recorded when it comes out from either side (when $Z_{permeant} > 0.5\ L_Z$ or $Z_{permeant} < -0.5\ L_Z$). The average permeation rate was obtained from the number of crossing events per permeant by dividing by the trajectory time and multiplying by one-half; it is equally likely for the permeant to go to either side from the center. The calculated

crossing rate per permeant of this system is directly proportional to both the unidirectional flux and the permeability. To relate this unidirectional permeation rate to the actual permeability, one should consider the effective concentration on both sides of the membrane. According to Fick's law, the permeability can be written as:

$$P = \frac{dn/dt}{\Delta C \cdot A_{tot}} \tag{24}$$

where dn/dt is the total unidirectional crossing rate, ΔC is the effective permeant concentration and A_{tot} is the total area of the membrane surface. For this system, considering the symmetry, the effective concentration on each side can be calculated by:

$$\Delta C = \frac{n/2}{A_{tot} \cdot Z_{eff}} \tag{25}$$

where n = 10 and Z_{eff} = 0.43σ^* which is the full width at half maximum of the Gaussian fit to the Z coordinate distribution of the permeant. After substituting equation (25) into equation (24), the permeability is written as:

$$P = 2Z_{eff} \cdot \frac{dn/dt}{n} \tag{26}$$

where $\frac{dn/dt}{n}$ is the measured average permeation rate.

2.2.3 Quantifying the phase composition

Each molecule at any time in the simulation was assigned to either the gel phase or fluid phase according to its orientational ordering relative to its neighbors. For each lipid membrane molecule, its ordering can be expressed by the nematic order parameter (S),[31]

$$S = \langle \frac{3 \cdot cos^2\theta - 1}{2} \rangle \tag{27}$$

where θ is the angle between the end-to-end vector of this molecule and that of its neighbor molecule, and the brackets denote the average over neighboring molecules whose center of mass are within a radius of 3.75 σ^* from the molecule of interest. When S is close to 1, the molecule's vector is almost parallel with its neighbors', indicating an ordered structure. Upon analyzing the distribution of S over all molecules at different area densities (Figure 5) a distinctly bimodal distribution becomes apparent at area densities between 0.7 and 0.76. A value of S=0.9 was selected as the dividing point between the disordered and ordered populations.

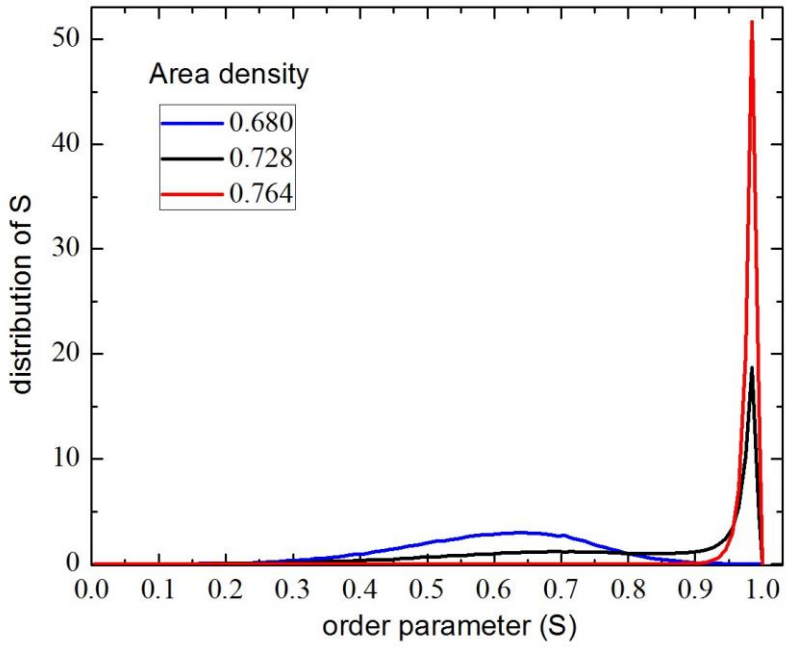

Figure 5. The normalized probability distributions of the nematic order parameter S at the area density of 0.680 (pure fluid phase), 0.728 (the middle of the phase transition) and 0.764 (pure gel phase).

After each molecule is classified as gel or fluid based on *S*, a second round of analysis was performed to identify molecules at the boundary region between the gel and fluid domains. These were classified as interfacial. For this classification, the composition of each molecule's neighbor list within a radius of $3.75\sigma^*$ was determined. If a molecule's neighbors are approximately equally divided between gel and fluid phases in their original designation (specifically, if the fraction of gel neighbors is between 0.3 and 0.7), then this molecule is defined as an interface molecule. Since the interface definition is overlaid on the order parameter definition, the original phase of an interfacial molecule can also be traced, as indicated in Figure 6. In a snapshot of a mixed-phase system viewed down the common orientational axis of the gel phase lipids (Figure 7), it is evident that the demarcation between the gel and fluid phases based on orientational order coincides with the demarcation between regions of packing order and disorder as well, confirming that the analysis is successful (with few scattered outliers) at identifying lipids in two distinct environments.

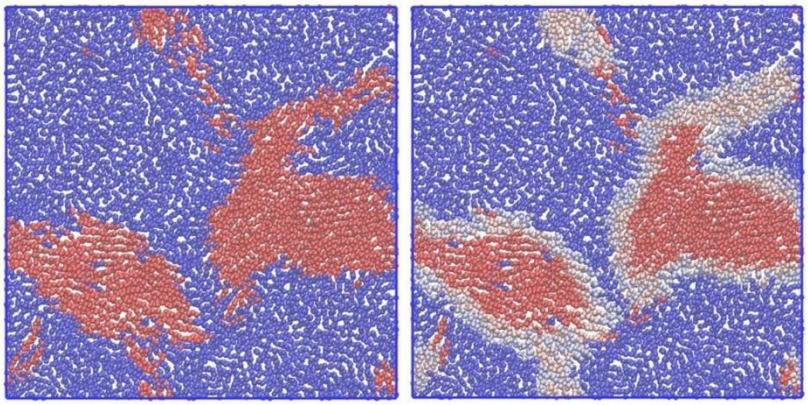

Figure 6. Illustration of the classification of lipids according to phase based on the criteria described in Simulation methods, using a simulation snapshot at area density $0.716\sigma^{*-2}$. (a) Lipids color-coded according to nematic order parameters (red: gel phase; blue: fluid phase). (b) As in (a), but with interfacial lipids colored a lighter color (light pink: fluid-phase molecule at interface; light blue: gel-phase molecular at interface).

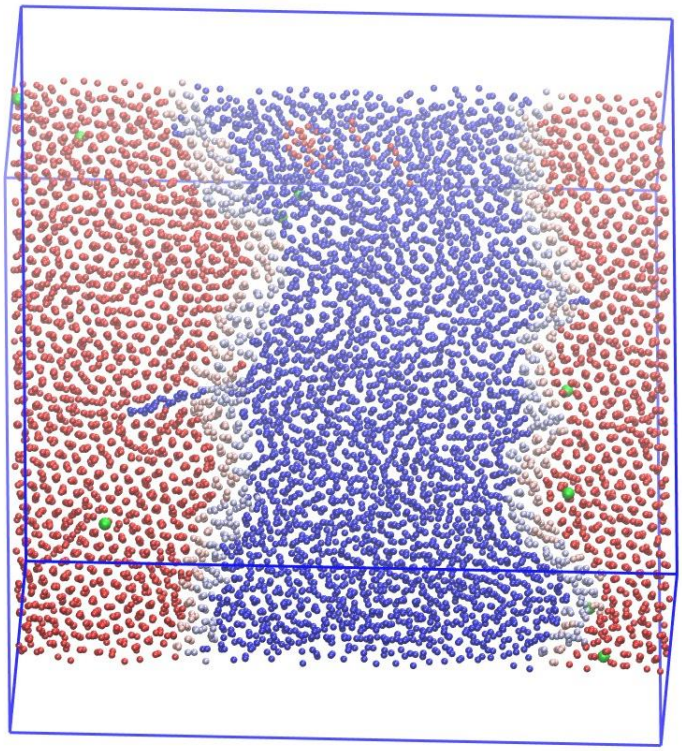

Figure 7. Two-phase system viewed down the molecular tilt axis of the gel phase. Permeants are colored in green. Lipids are color-coded according to nematic order parameters (red: gel phase; blue: fluid phase; light pink: fluid-phase molecule at interface; light blue: gel-phase molecular at interface).

2.2.4 Calculating the total area and area per lipid of the fluid phase

To define the area of the fluid phase and the local area per lipid within the fluid phase, care was taken to exclude interfacial regions, whose locations evolved over the trajectory. A series of configurations at time intervals of $1669t^*$ were extracted to perform the analysis. To calculate the fluid phase area of a configuration, the system's total area was equally divided into 400 grid squares. Each square whose fluid phase lipid fraction remained greater than 80% over five consecutive configurations in the series was considered to contain pure fluid lipids. The number N_g of these grid squares and the number of lipids ($\bar{n}_i$) they contained (averaged over the five configurations) were then recorded and incorporated into the area per lipid calculation as:

$$a_f = \frac{N_g \cdot a_g}{\sum_{i=1}^{N_g} \bar{n}_i} \tag{28}$$

where a_g denotes the area of each grid square. The final average a_{fluid} is the average of all data points of a_f. The total area of the fluid phase in a trajectory is calculated using: $A_{fluid}=a_{fluid} \cdot N_{fluid}$, where N_{fluid} denotes the total number of the fluid molecules.

2.3 Results

2.3.1 Evidence for a phase transition

A gradually increased area density over a two-phase coexistence region at constant temperature should show a region of instability in the system's surface pressure. The plot (Figure 8A) of the surface pressure versus the area density of the system shows a decrease over a density range of about 0.70 – 0.76 $(\sigma^*)^{-2}$, which is an indication of the phase transition region. Use of the orientational order parameter to classify lipids as gel or fluid shows that the two phases coexist over this range of area densities, as shown in Figure 8B.

2.3.2 Permeability across the phase transition

Figure 8A shows that the average crossing rate of a permeant (permeation rate) exhibits a plateau rather than a continuous decrease within the phase transition range, as the average density is increased. According to the "leaky interface" hypothesis, such a plateau is expected to be the result of an enhanced permeation rate at the gel-fluid interface, which as expected appears and disappears over the course of the phase transition (Figure 8B).

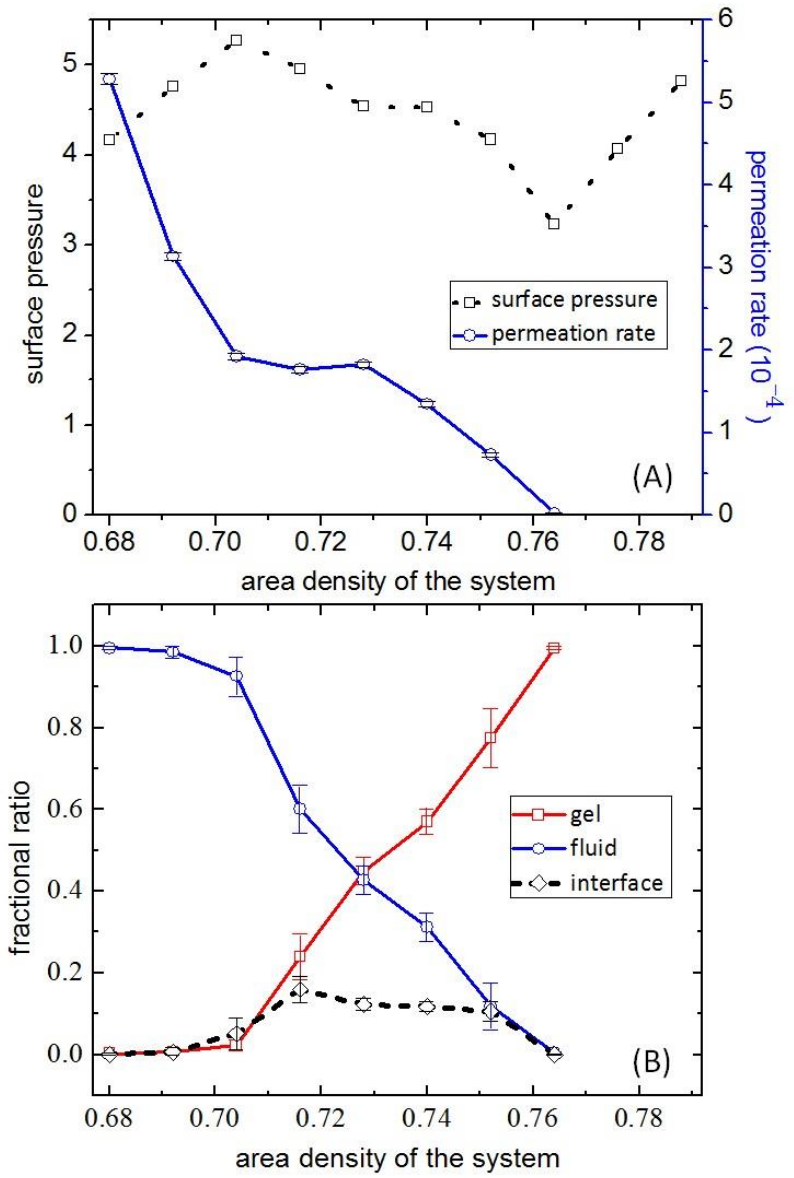

Figure 8. (A) The average crossing rate of a permeant (circles, blue lines) and the surface pressure versus area density (squares, dotted black lines). (B) The mole fraction of gel phase (squares, red lines), fluid phase (circles, blue lines) and interfacial (diamonds, dashed lines) lipids versus area density. All quantities are in reduced units.

2.3.3 Quantitative test of the "leaky interface" hypothesis

To test whether this hypothesis explains the behavior of the current model system, the local lipid environment (gel phase, fluid phase or interface) at each permeation event

was recorded. Since the fraction of each phase is known, the normalized permeation rate at each phase can be calculated by totaling the statistics of the crossing events at that phase. The results of four independent simulations with densities located within the two-phase coexistence range are shown in Figure 9. As expected, the local permeation rate of the gel phase is very small. However, at all four area densities simulated, there was no indication of a preference for the permeant to cross the membrane through the interface rather than through the fluid phase. Even if only the fraction of interface whose order is liquid-like is included, the local permeability of the bulk fluid is still approximately twice as high as that in the interface. Therefore, the plateau in permeation observed during compression with this model does not arise from an enhancement of permeation local to the interface.

As is also indicated in Figure 9, the local permeation rate of the fluid phase undergoes an increase with the system's area density increase. This may suggest that the proximity to the interface is enhancing the permeation processes, even though the permeation is not localized in the interface. Therefore, the effects of coexistence with the gel phase on the properties of the fluid phase need scrutiny.

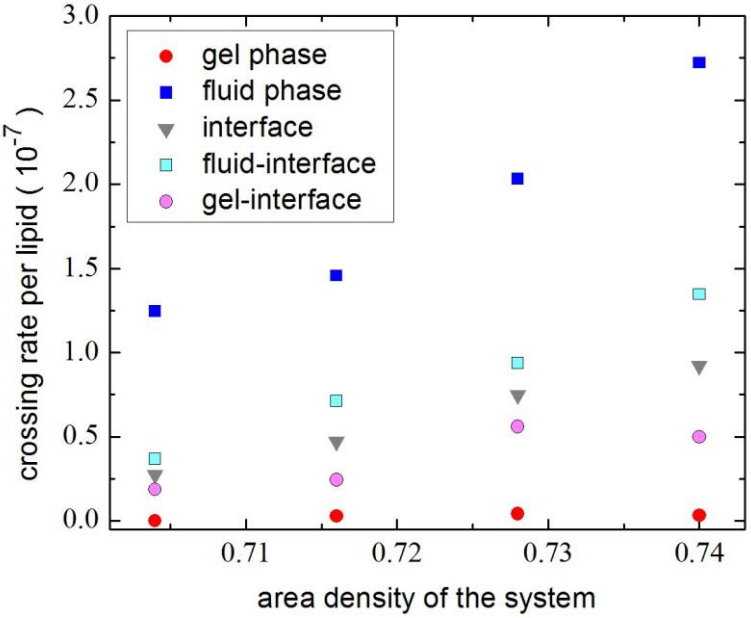

Figure 9. Permeation rate through each phase, normalized to the average number of lipids in that phase, at constant total area $A_{tot} = 50\sigma^* \times 50\sigma^*$.

2.3.4 Area per lipid of the fluid phase

In general, the total permeation rate k_{tot} can be written in terms of the local permeation rate of each phase weighted by the area fraction of that phase: $k_{tot} = (A_{gel} / A_{tot}) \cdot k_{gel} + (A_{fluid} / A_{tot}) \cdot k_{fluid} + (A_{interface}/A_{tot}) \cdot k_{interface}$, where A_{tot} is the total area of the system and A_{phase} is the total area of that phase. This is because the probability for the permeant to interact with a phase is directly proportional to the phase's area, given the permeant's ability to move freely around the bilayer and not attach preferentially to any specific region. Since k_{gel} and $k_{interface}$ are both small compared to k_{fluid}, the expression of k_{tot} could be simplified to: $k_{tot} = (A_{fluid}/A_{tot}) \cdot k_{fluid}$. In Figure 10, the area fraction of the fluid phase A_{fluid}/A_{tot} has been plotted versus total density. The permeation rate drops over the area density range between 0.68 and 0.704, while the

fluid area fraction remains constant. As the area density is increased further, the fluid area fraction drops while the permeation rate plateaus, indicating a compensating increase in local fluid-phase permeation rate, consistent with Figure 9. The local area per lipid in the fluid phase presents the exact same trend as the local fluid phase permeation rate during the phase transition. A likely explanation is that the expanded area per lipid in the fluid phase lowers the free energy barrier to permeation in that local area by allowing more free room during the permeation process.[51] Such an effect should be sensitive to the permeant's size.

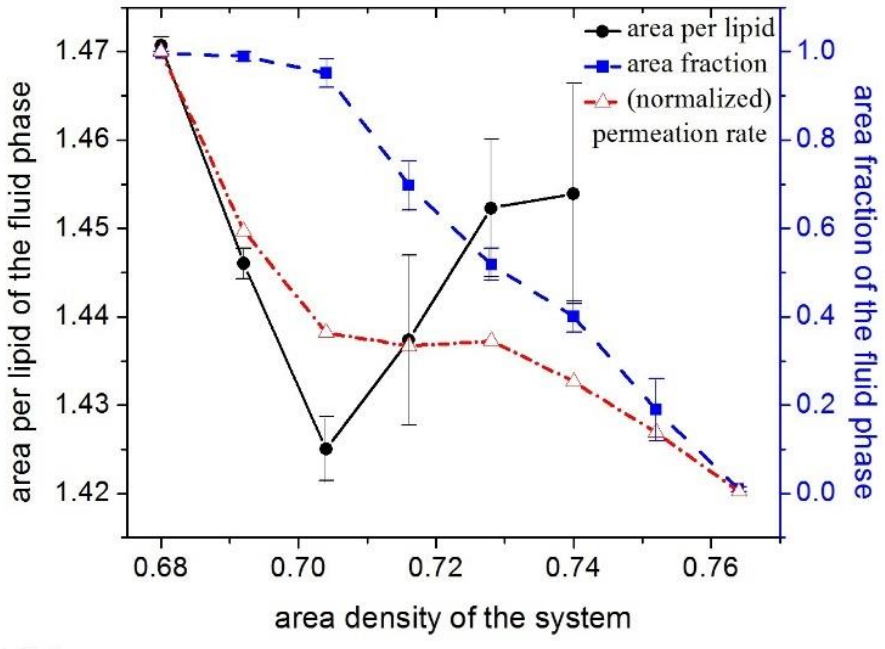

Figure 10. Changes in the fluid phase area fraction (squares with dashed blue lines) and fluid phase area per lipid (circles with black lines) with total lipid area density. The trend in total permeation rate (triangles with dot-dashed red lines) is shown for reference.

2.3.5 Permeant size effect

In Figure 11, the influence of the permeant's size on the permeation rate is shown. When the L-J radius of the permeant is increased, the absolute permeation rate decreases, as expected. However, as the permeant becomes larger, the anomalous trend of the permeation rate becomes more distinct, with an emergence of the plateau, then a small peak. As can be also seen from the graph, in the pure fluid phase (below area density of ~0.7) the permeation rate of a large permeant shows a steeper dependence on total area density. This is consistent with a larger anomaly in the permeation in the two-phase region, assuming that the effect is related to the decrease in local fluid phase area density during the phase transition.

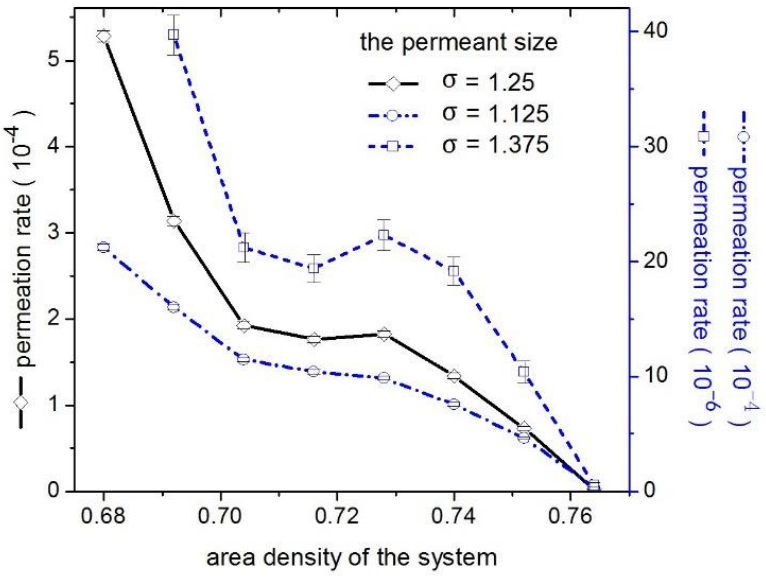

Figure 11. The permeation rate versus lipid area density at different permeant sizes: standard size (1.25 σ^*, diamonds with black lines), larger (1.375 σ^*, squares with dashed lines) and smaller (1.125 σ^*, circles with dot-dashed lines). Note that y-axes are scaled to accommodate the approximately 50-fold variation in the total permeation rate.

2.3.6 System size effect

In addition to the size effect of the permeant, the system size's effect on permeation rate is shown in Figure 12, where the average crossing rate of a permeant with density has been plotted at different system sizes. While the crossing rate is insensitive to system size in the pure fluid phase region, it shows a distinct increase with larger systems in the phase transition region. In order to understand the trend in terms of system size, the mole fraction of the fluid phase has been calculated at a certain system density. As shown in table 2, the average fluid mole ratio decreases with increasing system size during the early part of the compression, but increases with system size as the overall area density approaches the fully gel-phase limit.

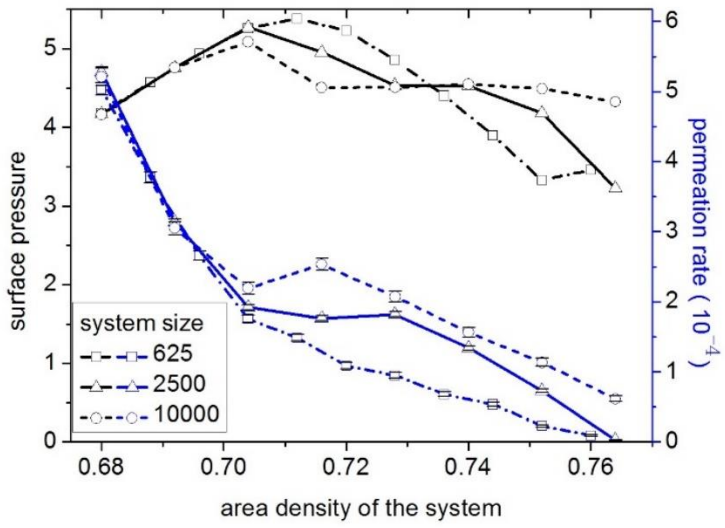

Figure 12. The crossing rates (blue lines) and surface pressure (black lines) vs. density at different system areas: (A_{tot}=25σ^*×25σ^*, squares with dot-dash lines; A_{tot}=50σ^*×50σ^*, triangles with solid lines; A_{tot}=100σ^*×100σ^*, circles with dashed lines).

System size	small	medium	large
$\chi(\alpha = \mathbf{0.716}\ \ \sigma^{*-2})$	0.73 ± 0.15	0.68 ± 0.06	0.64 ± 0.02
$\chi(\alpha = \mathbf{0.752}\ \ \sigma^{*-2})$	0.02 ± 0.01	0.15 ± 0.06	0.26 ± 0.02

Table 2. The fraction χ of molecules in the fluid phase and its standard deviation as functions of the system size (as defined in the caption to Figure 12) at two area densities.

2.4 Discussion

Our first goal in this discussion is to explain the observations from the simulations. Then we will turn to the question of whether they are relevant to the experimentally observed anomalous permeability, and how that phenomenon might be modeled semi-quantitatively.

2.4.1 Model to understand gel-fluid coexisting phase

In a system at fixed total area and fixed total number of lipids containing a mole fraction and domain area x_f and A_f, optimization of the total system free energy produces a difference in surface pressure between gel and fluid domains as predicted by the two-dimensional Young-Laplace equation:

$$\left[\frac{\partial F(A_f, x_f)}{\partial A_f}\right]_{x_f} = 0 = p_g - p_f + \Lambda\sqrt{\frac{\pi}{A_f}} \tag{29}$$

with interfacial energy $2\pi r\Lambda = 2\Lambda\left(\pi A_f\right)^{1/2}$ based on an assumed circular domain shape.

As the lipid components of the two domains can interchange, their chemical potentials must be equal at equilibrium:

$$\left[\frac{\partial F(A_f, x_f)}{\partial x_f}\right]_{A_f} = N_{tot}(\mu_f - \mu_g) = 0 \tag{30}$$

From the Gibbs-Duhem equation at constant temperature we may write, for either pure phase:

$$d\mu/dp = a \tag{31}$$

where $a = A/N$ is the area per lipid. Defining p_0 as the pressure where the phases are at coexistence in the absence of interfacial effects,

$$\mu_f(p_0) = \mu_g(p_0) \tag{32}$$

we can express the chemical potentials of the phases at pressures near p_0 as:

$$\mu_g(p_g) \approx \mu_g(p_0) + a_g \cdot (p_g - p_0) \tag{33}$$

$$\mu_f(p_f) \approx \mu_f(p_0) + a_f \cdot (p_f - p_0) \tag{34}$$

Combining equations (30), (31), and (32-34) yields the following equations:

$$p_f = p_0 - \Lambda \frac{a_g}{a_f - a_g}\sqrt{\frac{\pi}{A_f}} \tag{35}$$

for a fluid domain of area A_f embedded in a gel, and

$$p_g = p_0 - \Lambda \frac{a_f}{a_f - a_g}\sqrt{\frac{\pi}{A_g}} \tag{36}$$

for a gel domain of area A_g embedded in a fluid.

2.4.2 Interpreting the simulation results

The results suggest strongly that the plateau or peak in permeability during the

compression of the membrane comes from the competing effects of two trends: the fluid phase area per molecule increases as the total fluid phase area fraction goes down. The second trend violates the "lever rule" for phase coexistence, according to which the intrinsic properties of coexisting phases will remain constant throughout the transition. The source of this violation is the interface, whose contribution to the system's free energy is to a first approximation given by a line tension multiplied by the length of the interfacial boundary. (In the treatment of bulk phase separation leading to the lever rule, the interfacial free energy is assumed to be zero.)

A simple model for the effect of the line tension Λ on the pressures of coexisting phases at constant area yields the prediction that the surface pressure p_f inside the domain is lower than the pressure p_0 of the phases at coexistence in case of negligible interfacial effects:

$$p_f = p_0 - \Lambda \frac{a_g}{a_f - a_g} \sqrt{\frac{\pi}{A_f}}; p_g = p_0 - \Lambda \frac{a_f}{a_f - a_g} \sqrt{\frac{\pi}{A_f}} \quad (37)$$

with a_f and a_g the areas per lipid of fluid and gel phases. For a gel domain embedded in a fluid membrane, a similar expression is obtained:

$$p_g = p_0 + \Lambda \frac{a_f}{a_f - a_g} \sqrt{\frac{\pi}{A_g}}; p_f = p_0 + \Lambda \frac{a_g}{a_f - a_g} \sqrt{\frac{\pi}{A_g}} \quad (38)$$

The predictions of this model are qualitatively consistent with the observed trends in fluid phase area per lipid, which will increase with decreasing p_f. In the early stages of compression within the two-phase system, the gel domain area A_g grows, decreasing

p_f and increasing the area per lipid of the phase. In the late stages of compression, the fluid domain area A_f shrinks, again decreasing p_f and increasing the area per lipid of the fluid phase.

We can rationalize this behavior by considering the effect of "turning on" the line tension within a system of two coexisting phases at constant total area. The phase with the lower total area will form a single circular domain to minimize the interfacial length. Then, to further reduce the interfacial energy by shrinking the domain, lipids from the domain may join the surrounding phase. If the area per lipid in the domain is greater than that of the surroundings, this transition will free up area and reduce the pressure in both phases. Conversely, if the area per lipid is less than in the surroundings, this adaptation to the line tension will decrease the available area and increase surface pressure.

The correlation between increased area per lipid in the fluid phase and increased permeability is natural: at higher areas, there is greater free volume in the membrane to permit permeation. Considered from a thermodynamic rather than a structural perspective, the free energy barrier associated with inserting a molecule into the bilayer will contain some component of a work of area expansion, scaling as surface pressure multiplied by the effective permeant area.

We note that a correlation between the anomalous permeability and the total length of the interface has been noted previously in support of the leaky interface hypothesis.[43] The simulations and the simple thermodynamic model both point to a key role for the gel-fluid interface in promoting permeability; however, rather than being the site of enhanced permeation itself, the interface makes the whole fluid phase domain leakier through the action of its line tension. The effect depends on permeant size; as larger particles are observed to have a more sensitive dependence on lipid area density than small particles.

The effect of system size on permeability (shown in Figure 12) is more complicated to explain. At small system size, domain formation of the minor phase is suppressed (as the high ratio of interfacial length to domain area destabilizes the phase-separated state with respect to the state of uniform density). From Table 2 it can be seen that when the fluid is the majority phase (at area density 0.716), the mean fluid area fraction is greater for small systems than for larger systems, leading to fluid phases with higher area density (consistent with the higher pressure seen in the smaller system.) At a more compressed state (area density 0.752) the fluid phase is suppressed almost entirely in the smallest system, producing a gel phase with a higher area per lipid (consistent with the surface pressure that is lower than for the larger system). Both effects tend to reduce permeability at the smaller system sizes.

2.4.3 Comparison of simulation model to true lipid bilayers

The primitive simulation model reproduces the first-order transition between an approximately impermeable phase, which displays strong orientational order and regular packing, and a more permeable disordered phase with a higher area per molecule. The ratio of disordered phase to ordered phase area per lipid is about 1.1 in the simulation model, as opposed to ~1.25 or greater in experiment. (Due to the effectively fixed bilayer thickness in the present model, the area ratio reflects the volume ratio of the chains. The 10% increase in volume upon melting is consistent with the ratio of about 1.08 of the experimentally derived volumes of tail CH_2 groups in the fluid[66] and gel phases[67].) Like an actual lipid bilayer, the simulation model shows an increase in area compressibility within the two-phase region, as the surface pressure shows a plateau or a decrease with increasing compression (Figure 13). One structural difference between the simulation model and the experimental system is the presence of only one leaflet instead of two. As neither main explanation for the anomalous permeability invokes the presence of two leaflets, the symmetric monolayer nature of the current model should not disqualify it as a way to explore the phenomenon. Another difference is that the present model is constrained to maintain the same thickness whether in the gel or the fluid phase, eliminating any features of the interface that might arise from the "hydrophobic mismatch" between the phases. A further difference is that the simulations are performed using flat systems at fixed area with periodic boundaries, while most experimental results have been obtained using curved vesicles, whose areas are not constrained. Simulations performed at constant

pressure using the present model moved rapidly toward uniform all-fluid or all-gel structures, and remained uniform over the duration of the trajectories.

In the present simulations, we have observed a peak in permeability in a small model membrane patch, held at constant area over each trajectory, as system area density was varied at fixed temperature across a phase transition. It is not obvious whether the phenomena observed here are relevant to experiments performed under a completely different set of constraints, where anomalous permeability is observed upon varying temperature in systems containing self-assembled vesicles. Finite-size effects are evident in the present simulation results, although the anomaly does not appear to vanish with increased system size. A greater limitation is the constraint of fixed area: vesicles at thermal equilibrium are not constrained to a fixed surface area, and are typically considered to exist in a state of zero surface tension.[68]

One special case that can be treated as a constant-area system over the course of a permeation event is that of a fluid patch embedded in a larger gel domain. The gel is expected to act as an effectively rigid outer shell that will not expand or compress in response to changing stresses in its interior. In this case one can predict that introducing the permeant will lower the perimeter of the fluid domain, thereby reducing the effective free energy barrier to permeation by an amount equal to the reduction in interfacial energy, *i.e* the line tension Λ times the reduction in perimeter.

Consider a permeant of area A_p passing through a circular fluid-phase domain of area A_0. (A_p here represents the area increase of a fluid-phase bilayer at zero surface tension upon embedding the permeant at its midplane.) We will assume that the permeant does not contact the gel phase directly, so the contribution to the free energy barrier from direct permeant-lipid interaction is not affected by the presence of the surrounding gel phase. At the midpoint of the permeation event, when the center of mass of the permeant is located at the bilayer midplane, the area available to lipids has been decreased by A_p. To accommodate this intrusion (subject to constant total area enforced by the rigid gel surroundings), a number of lipids must undergo a transition from fluid to gel. Since each lipid's transition frees up an area equal to the difference Δa in area per lipid in fluid and gel states, the number of lipids (per leaflet) that change states is $N_{switch}=A_p/(a_f-a_g)$. The resulting patch of fluid (including the embedded permeant; see cartoon representation in Figure 13) has area $A_0+A_p-N_{switch}\times a_f$, or A_0-cA_p, with $c=a_g/(a_f-a_g)$. A typical ratio of gel and fluid-phase lipid areas $a_g/a_f\approx$0.75-0.8 produces values for c between 3 and 4. The fluid phase domain containing the permeant will thus have its area reduced by 3 to 4 times the area of the permeant (down to a minimum of A_p). The interfacial free energy of the shrunken fluid domain, which is proportional to its radius, is therefore reduced to $(1-cA_p/A_0)^{1/2}$ of its original value. This decrease in interfacial free energy at the "transition state" lowers the effective permeation barrier compared with what a

permeant would encounter in passing through a pure fluid phase. In other words, the line tension helps pull the permeant into the fluid domain via the reduction in surface pressure presented in equation (37).

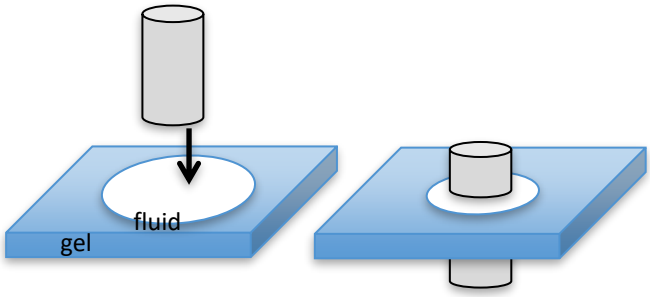

Figure 13. Cartoon representing the introduction of a permeant into a fluid domain (white) embedded in a gel region (blue). To accommodate the permeant's area within the rigid gel environment, fluid phase lipids join the gel phase. The outer radius of the fluid domain is reduced, the decrease in gel-fluid interfacial energy compensating in part for the free energy penalty of inserting the permeant in the fluid phase.

For example, assuming c=3, a fluid domain whose area is four times that of the permeant ($A_0 = 4\ A_p$) will experience a 75% reduction in total area and a decrease in perimeter by 50%. If the original domain has a total interfacial energy of $4k_BT$ (for instance, a domain of radius 4.5 nm at a line tension of 0.6 pN at 310 K) then the gel-fluid interfacial free energy would decrease by 2 k_BT at the midpoint of permeation. This effectively lowers the permeation free energy barrier (relative to the barrier in a pure fluid membrane) and would be expected to increase the permeation rate through that domain by a factor of $\exp(2k_BT/k_BT) \approx 7$, relative to the same sized fluid patch in a single-phase system.

Qualitatively, the enhancement via this mechanism is expected to become stronger for larger permeants, as their permeation through a fluid domain will reduce the gel-fluid interface by a larger absolute length than will a small permeant. Any peak in permeability vs. temperature would also be expected to become narrower with increasing permeant size, as sufficiently large fluid-phase domains surrounded by gel would only be expected to exist very close to T_m. Assessing whether this effect could account for the experimentally observed increase in the total permeation rate through a vesicle across a phase transition would depend on the overall distribution of domain sizes vs. temperature, which is beyond the scope of this article.

The line tension-assisted enhanced permeation effect described above cannot explain the experimentally reported persistence of the anomaly at temperatures slightly above T_m, where the area fraction of gel domains is small and the likelihood of a permeant encountering a fluid region embedded in gel is low. Above T_m, if the creation or growth of compact gel domains (or transient ordered regions[69]) is involved in accommodating lipids displaced by permeants, in general the interface will be expanded, not reduced. Line tension effects would raise the effective barrier to permeation. In this regime, there may be more general effects related to the enhanced surface compressibility and area fluctuations that influence permeability, stemming from the thermodynamically and kinetically accessible reservoir of positive and

negative area fluctuations made available by the facile interconversion of gel and fluid phases. Further work is necessary to test this concept, and may yet reveal a reconciliation of the competing explanations for anomalous permeability, in that the interfaces between gel and fluid domains do promote leakiness, but do so by mediating the exchange of area characteristic of a highly compressible surface.

2.5 Conclusions

A simple model simulation system for transmembrane permeation produces an anomaly (a plateau or a peak, depending on conditions) in permeation rate as the membrane is compressed across a phase transition analogous to the fluid-gel transition in lipid bilayers. The enhanced permeation is not localized to the interface regions, but rather appears to be influenced by the interfacial line tension, which produces an increasing trend in lipid-phase area per headgroup across the transition to the gel phase. The competing effects of increasing area per lipid in the fluid phase and decreasing fluid phase area fraction yield the plateau or the peak in total permeability. The trend in area per lipid can be interpreted using a simple thermodynamic model for the free energy of the mixed-phase bilayer at constant area, under the influence of the interfacial line tension.

In an effort to extrapolate from the simulation results to larger permeants and larger systems, a model is developed to predict the degree to which interfacial line tension

would lower the effective free energy barrier for permeation through a fluid domain embedded in a gel domain. In general, these results suggest that the gel-fluid interface, while not "leaky" in the sense originally suggested of being the site of localized defects,[34] may enhance permeability through their effects on surface pressure and/or a means to free up area to accommodate lipids temporarily displaced by the permeant. Such mechanisms are closely related to the phenomenon of enhanced compressibility and area fluctuations near the transition temperature, which has also been invoked to explain the anomalous permeability at the transition.[44]

Chapter 3

The line-tension-assisted membrane permeation at the transition temperature in mixed gel-fluid bilayers*

The umbrella sampling method has been used to evaluate the free energy profile for a large permeant moving through a lipid bilayer, represented using a coarse-grained simulation model, at and below its gel-fluid transition temperature. At the lipid transition temperature, determined to be 302 *K* for the MARTINI 2.0 model of DPPC, the permeation barrier for passage through an enclosed fluid domain embedded in a patch of gel was significantly lower than for passage through a fluid stripe domain. In contrast, permeation through a fluid domain in a stripe geometry produced a free energy profile nearly identical to that of a gel-free fluid bilayer. In both cases, insertion of the permeant into a fluid domain coexisting with the gel phase led to a shift in phase composition, as lipids transitioned from fluid to gel to accommodate the area occupied by the permeant. In the case of the enclosed fluid domain, this transition produced a decrease in the length of the fluid-gel interface as the approximately circular fluid domain shrank. The observed decrease in the apparent permeation barrier, combined with an approximation for the change in interfacial length, enabled estimation of the interfacial line tension to be between 10 and 13 *pN* for this model. The permeation barrier was shown to drop even further in simulations

* Adapted from reference [70].

performed at temperatures below the transition temperature. The results suggest a mechanism to explain the experimentally observed anomalous peak in the temperature-dependent permeability of lipid bilayers near their transition temperatures. The contribution of this mechanism toward the permeability of a gel phase containing a thermal distribution of fluid-phase domains is estimated using a simple statistical thermodynamic model.

3.1 Backgrounds

A curious property of lipid bilayer permeability is that it exhibits an anomalous peak, rather than a continuous increase, as temperature is raised across the bilayer main chain order/disorder transition temperature T_m.[34] Although the permeability anomaly is a general property among bilayers, experimental studies have shown that the magnitude of the anomaly depends on both the permeant and the type of lipids.[12, 41] The permeability properties of bilayers near their transition temperatures are relevant to the performance of thermo-sensitive liposomes designed to encapsulate drugs and release them at the desired locations (e.g. tumors) upon local application of elevated temperatures.[27] Liposomal systems primarily composed of dipalmitoylphosphatidylcholine (DPPC) bilayer, whose T_m is only several degrees above the body temperature,[32] are under active development as thermally activated drug delivery agents.[30, 71]

While it is not surprising that the ordered low-temperature lipid bilayer phases are much less permeable than the fluid high-temperature phases, it is not obvious why bilayers at temperatures near the transition, where domains of both phases may be expected to coexist, should have greater permeability than either pure phase. Two main explanations have been given for the anomalous permeability peak. The "leaky interface" model suggests a much greater local permeability to the interfacial regions between the gel and fluid domains.[34, 39] This model is consistent with the overall permeability trend with temperature.[43] Alternatively, the anomaly can be explained by the peak in lateral compressibility (or equivalently, in area density fluctuations) also seen around T_m.[44-45] In our recent study[5] investigating the permeability of a simple coarse-grained membrane model across an ordering transition, achieved through lateral compression at constant temperature, a weak anomaly in the permeability was observed. Tracking the position of each permeation event (fluid, gel or interface), allowed the "leaky interface" explanation to be ruled out as an explanation for that specific model.

Instead, our results implied a line-tension-assisted effect in lowering the free energy barrier of the permeant, which becomes more apparent with a larger permeant.[5] For a state in which a fluid domain is embedded in bulk gel, conversion of lipids from the fluid to the gel state provides a source of excess area. A positive surface pressure induced by the insertion of a permeant will push lipids at the edge of a fluid domain to

join the adjacent gel. The expected result is that the length of the interface between the gel and fluid domains shrinks during the insertion process, producing a negative free energy contribution whose magnitude is the product of the interfacial line tension and the decrease in interface length. This contribution may partially counterbalance the permeability free energy barrier, and so increase the rate of transport across the membrane. Without the loss of generality, this proposed explanation should be applicable to more realistic lipid models. In this chapter, we have used umbrella sampling methods to calculate the free energy barrier for passage of a large particle across the DPPC bilayer, as represented using the coarse-grained MARTINI 2.0 forcefield,[53, 72] in fluid and mixed gel-fluid states at temperatures near the transition temperature.

In an attempt to observe a strong line tension effect, a large permeant was designed for this study. The middle of this permeant was approximately a cylinder with a height of 3.5 *nm*, and a radius of 3 *nm*, which will ensure a large excluded area across the bilayer when in the center. The cylinder was attached to two identical cone-shaped parts, to promote a smooth change in the lipid structure during its insertion into bilayer, and thus avoid sharp features in the free energy profile.

The permeability free energy barrier was consistently lower for passage through a fluid domain embedded in a gel-phase bilayer, in which shrinking of the fluid domain

was observed as expected when the permeant was introduced, than for passage through a pure fluid domain. The difference broadened as temperature was decreased. This temperature-dependent trend can be attributed to the favorable free energy of the bulk fluid-gel transition at temperatures below T_m. The isolation of the effect of interfacial line tension from this bulk effect was achieved in two steps. First, stripe domain melting kinetics simulations[46] were performed to identify the transition temperature T_m as between 302 and 303 *K*. Next, at 302 *K*, the permeation free energy barriers presented by a uniform fluid bilayer, an enclosed fluid domain surrounded by gel, and a continuous fluid stripe domain (fixed at constant area) were all compared. Since insertion of the permeant produces about the same change in the area of the fluid domain for both enclosed and stripe domain systems, but a much more pronounced change in interfacial length in the enclosed domain, the difference between the barriers calculated for these two systems was used to obtain the line tension. The value of 10-13 *pN* obtained is consistent with the value recently obtained using a different approach for the same forcefield by Katira.[73-74] These results confirm the importance of line tension effects on bilayer permeability, and pave the way for a statistical thermodynamic treatment of the temperature dependence of permeability near the phase transition temperature.

3.2 Simulation Methods

3.2.1 Construction of the system

A dipalmitoylphosphatidylcholine (DPPC) bilayer as represented by the coarse-grained MARTINI[53, 72] forcefield was used to study the permeation rate anomaly. Molecular dynamics simulations, including those with external umbrella potentials, were performed using Gromacs[64] version 4. The system's temperature was control by the velocity rescaling[55] method, with a time constant of 1.0 *ps*. The pressure was maintained at 1 bar using the Berendsen pressure coupling method, with a time constant of 2.5 *ns*. The uniform fluid and enclosed fluid systems employed anisotropic pressure coupling with a compressibility of 5×10^{-5} bar^{-1} in all three directions. For the stripe fluid however, the compressibility was set to 0 for *x* and *y* directions, to maintain a constant area. The Lennard-Jones cut-off was 1.2 *nm*, with the switch function started to apply at 0.9 *nm*. The time step used for this study was 25 *fs*.

A permeant with an approximately 3 *nm* radius was constructed from a close-packed lattice of neutral Lennard-Jones sites, bonded to their nearest neighbours through a harmonic potential with a minimum distance of 0.470 *nm* and force constant of 12500 $kJ{\cdot}mol^{-1}{\cdot}nm^{-2}$. The hydrophilicity pattern on the surface (Figure 14) was chosen and adjusted to prevent water from moving into the bilayer with the permeant when it enters, to prevent lipids from sticking to it when it leaves, and to be repulsive enough to the lipids that the permeant will spontaneously and quickly leave the bilayer if all perturbations are removed. The details of the permeant's topology and interactions are

given in Table 3 and Figure 14. Gromacs topology files for the permeant are provided as Supporting Information.

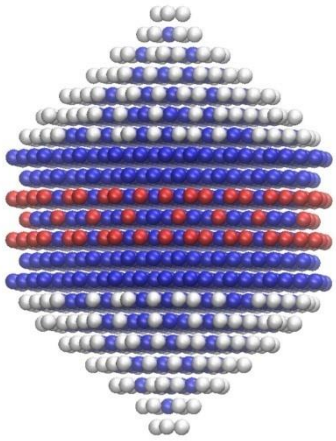

Figure 14. Side view of a permeant particle. The molecule is composed of 1717 sites, with its corresponding L-J interactions to each colour given in Table 3.

	blue site	White site	Red site
Water or antifreeze	Semi attractive	Intermediate	Semi attractive
Lipid headgroup	Intermediate	Intermediate	Intermediate
Lipid backbone	Almost intermediate	Intermediate	Almost intermediate
Lipid tail	Semi repulsive	Intermediate	Almost intermediate

Table 3. The L-J potential of the permeant.

The description of the levels of L-J interaction is the same as in reference [72]. Semi attractive: ε = 4.0 kJ/mol, σ = 0.47 nm; intermediate: ε = 3.5 kJ/mol, σ = 0.47 nm; almost intermediate: ε = 3.1 kJ/mol, σ = 0.47 nm; semi repulsive: ε = 2.7 kJ/mol, σ = 0.47 nm.

Table 4 lists the parameters of the following three types of simulation system: uniform fluid bilayer, continuous stripe fluid, enclosed fluid domain surrounded by gel. Snapshots of each system are given in Figure 15.

System	Uniform fluid	Stripe fluid	Enclosed fluid
N_{DPPC}	3000	3930	4096
Hydration level (water #/lipid)	102.7	78.37	75.20
Average box dimension (nm^3)	30.4×30.5×15.2	32.4×32.4×14.5	31.7×32.0×15.1
Ensemble	NPT	NP_zAT	NPT

Table 4. The parameters of three types of fluid systems.

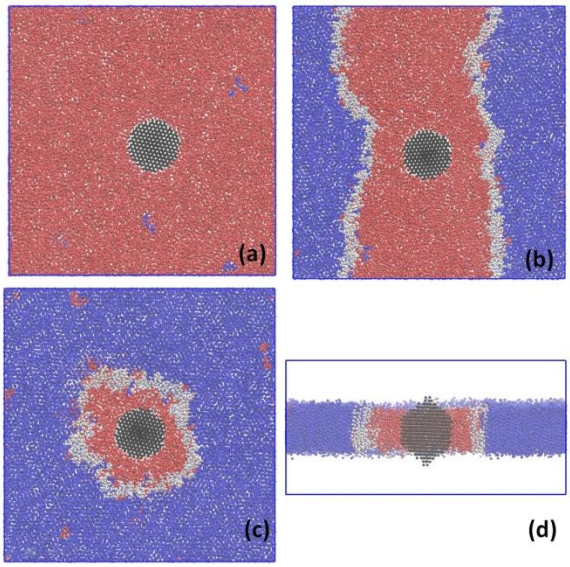

Figure 15. Simulation systems. The top view of: (a) a uniform fluid bilayer; (b) a continuous fluid stripe; (c) an enclosed fluid domain surrounded by gel. (d) The side (cut) view of (c). (Red: fluid phase; blue: gel phase; light blue or light pink: interface; black: permeant.)

3.2.2 Quantifying the phase composition and its corresponding area per lipid

A chain order parameter was used to assign lipids to gel or fluid phases of each molecule at any time in the simulation. As the gel phase lipid only has a small tilt under the MARTINI model,[75] for each lipid membrane molecule, its order parameter is defined as:

$$S_{chain} = \frac{1}{2}(3\langle cos^2\theta\rangle - 1) \quad (39)$$

where θ is the angle between the vector joining two next nearest-neighbor beads (pairs 1/3 and 2/4 of the tail beads in each tail) and the membrane surface normal (z direction). According to the distributions of S_{chain} at different phase compositions, S_{chain} = 0.90 (with its corresponding θ = 15°) was selected as the dividing point between the ordered and disordered lipid molecules.

After each lipid was assigned as either gel or fluid according to S_{chain}, a neighbour list analysis was performed to identify the boundary regions between these two phases, which is the interface. For this calculation, the *PO4* site of each lipid was used, and a radius of 1.8 nm was chosen to allow an average of 20 neighbours within the cutoff. If the neighbor population composition of a lipid is close to equal in both phases (the fractional ratio of either phase is between 0.3 and 0.7), then that lipid is defined as an interface molecule.

For both the phase separation and the area per lipid calculation, we used a python script which incorporated the pyhull package for Voronoi diagram analysis. Two

lateral planes were defined for the bilayer, one for each leaflet, using the two C_1 lipid cites (C_1A and C_1B). The average z component of C_1 sites within 5 *nm* of the center of the permeant was calculated. Permeant sites with z component within 0.235 *nm* of that average were then used to account for the excluded volume of the permeant on that lateral plane. These two collections of points were put together to perform "Delaunay triangulation" in the *x*-*y* plane. The area per lipid of each phase was calculated by averaging the occupied areas of all lipid molecules that were assigned to that phase. Finally, the areas per lipid of each phase for the upper and lower leaflet were averaged again to obtain that for the bilayer. The excluded area of the permeant was calculated in a similar manner.

3.2.3 Determining the phase transition temperature (T_m)

Following previously reported procedures,[46] a fully-hydrated DPPC bilayer (4096 DPPC molecules) with alternating gel and fluid domains was equilibrated at 302 K for 200 ns, under the constant area condition. The fractional ratio of each phase stayed approximately the same. The final structure was used as an initial configuration to perform a 500 ns MD run using anisotropic pressure coupling, under different temperatures (299-306 K). The expansion or shrinking of the gel domain indicates whether the temperature is below or above T_m.

3.2.4 Calculation of the free energy barrier of the permeant

To greatly improve the sampling of inaccessible configurations and accurately

calculate the free energy barrier of the permeant across the bilayer, umbrella sampling and weighted histogram analysis method (WHAM) were applied.[76] Umbrella potentials were defined as quadratic functions of the distance along the bilayer normal direction (z) between the center site of the permeant and the center of a cylindrical section of the DPPC bilayer. The position of this cylinder was defined through an average over all lipid sites within a lateral distance of 5 *nm* from the permeant's center, and gradually decreasing weighted contributions from lipid sites in a range above 5 nm that switches to zero by 6 *nm*. To prevent the wobbling of the permeant (a slow orthogonal degree of freedom that would tend to hinder convergence) angle restraints of 500 $kJ{\cdot}mol^{-1}{\cdot}rad^{-2}$ with respect to the bilayer surface normal (along the *z* axis) were applied between the top three sites and their corresponding bottom three sites.

The harmonic constant for each sampling window was 500 $kJ{\cdot}mol^{-1}{\cdot}nm^{-2}$. To construct a free-energy curve of the permeant from the outside of the bilayer (6 nm) to the center of the bilayer (0 *nm*), at least 31 windows were needed at a 0.2 *nm* interval of the harmonic potential minima. Each window had an 80 *ns* run time while the starting configuration was pre-equilibrated for 50 *ns*. The convergence of each sampling window[77] and the total sampling coverage along the Z coordinate were carefully checked. More simulation windows were added as necessary until all umbrella windows were fully converged and all positions were sufficiently sampled. The bootstrapping method of complete histograms was used for error estimates of

free-energy barriers.[60]

3.2.5 Dynamics of release of the permeant from the center

To examine the dynamics of the permeant moving out of the bilayer, ten configurations were randomly chosen for each type of system from the umbrella sampling window centered at z = 0 *nm* to be the initial structures. The umbrella potential was removed, and the center of mass position of the permeant was recorded as a function of time during a constant-temperature MD trajectory, performed under the same pressure-coupling conditions as the umbrella sampling calculations. The time it took for the permeant center to first reach its free-energy minimum was saved. This time should be related to the rate of the permeant retreating ($k_{retreat}$). By approximating this process to be reversible, the rate of the insertion $k_{insertion}$ could be calculated using the following equation:

$$\frac{k_{insertion}}{k_{retreat}} = exp\left(-\frac{\Delta G^{\neq}}{k_B T}\right) \tag{40}$$

where $\Delta G^{\neq}$ is the free-energy barrier of the permeant across the bilayer.

3.2.6 The correlation between the fractional ratio of gel phase and position

For all of the umbrella sampling windows, the average position of the permeant is saved every 1 *ns*, and so is the fractional ratio of gel phase. Using this data, the mean fraction of gel phase was calculated over 0.2 *nm* increments along *z*.

3.2.7 Calculation of Δh

A small system (512 DPPC molecules, 28.56 water molecules/lipid), whose size prevents the formation of stable coexisting fluid-gel domains, was used for the estimation of Δh, the enthalpy per lipid of the gel-fluid transition. A near-uniform gel configuration (no distinct fluid domains) was pre-equilibrated at 273 *K*. The uniform fluid initial structure was prepared by melting this configuration at 343 *K*. These two structures were then set to run at 302 *K* for 200 *ns*, within which the last 100 ns trajectory was used for the enthalpy study. Here, only the chain order parameter was used to characterize the lipid molecules as either gel or fluid phase. The total number of gel molecules was counted for each system, to obtain ΔN_{gel} (the number of molecules whose phase had shifted). Δh is then calculated by scaling the total enthalpy difference ΔH to ΔN_{gel} of these two systems. The calculation result is listed in Table 5.

N_{gel} (Uniform gel)	N_{gel} (Uniform fluid)	ΔH (kJ/mol)	Δh (kJ/mol)
446 ± 26	0	11504 ± 16	25.8 ± 1.5

Table 5. Calculation results of systems with 512 DPPC molecules and 28.56 water molecules/lipid at 302 *K*.

3.3 Results

3.3.1 Pinpointing the phase transition temperature (T_m)

The thermodynamics of any process involving a phase transition will be sensitive to the system temperature relative to the transition temperature. In a bilayer system

formed from alternating gel and fluid stripes, the influence of the line tension on the phase transition direction can be neglected to first order because changing the widths of the stripes does not change the length of their borders. In that case, the growing or shrinking of the gel fraction at a certain temperature should indicate whether it is below or above T_m. Simulations of stripe systems at various temperature show (Figure 16) that the gel fraction undergoes a decrease at or above 303 K, and an increase at or below 302 K. This clearly supports that T_m is between 302 K and 303 K. The apparent diffusion of the gel/fluid boundary at 302 K indicates that it is very close to T_m. Therefore, we assume T_m = 302 K for further analysis.

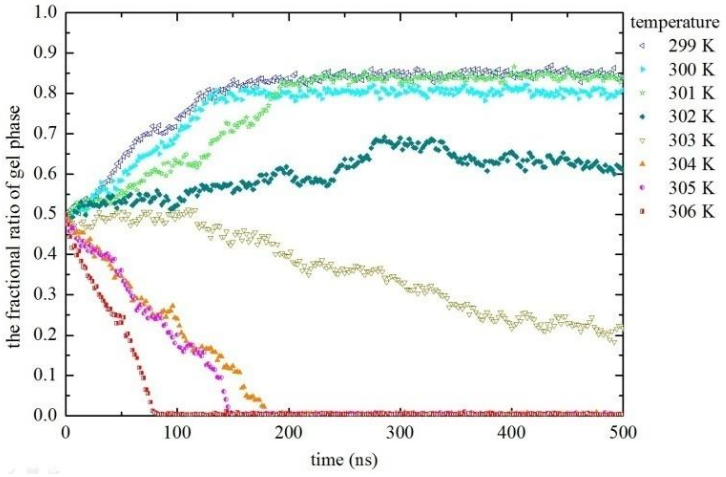

Figure 16. The change in the fractional ratio of gel phase of an alternating DPPC bilayer system at different temperatures.

Another feature of Figure 16 is that the gel fraction plateaus at around 0.8 when the temperature is below T_m, unlike higher temperatures, where the fluid domain ends up

occupying the entire system. An explanation can be seen in the "bridging effect" evident in snapshots of the system undergoing an increase in gel phase content at $T = 302\ K$ (Figure 17), and also observed in recent atomistic simulations.[78] When a "gel bridge" first forms within a slim "fluid stripe" (Figure 17c), the fact that the solid-like gel phase is percolating through the periodically repeating system will prevent further reduction in area, effectively blocking any further freezing. The subsequent gel-fluid exchange will minimize the line tension, forming compact fluid domains inside a bulk gel (Figure 17d). This is a meta-stable state that extends at least several degrees below T_m. In umbrella sampling calculations on stripe-geometry systems, changes to the width of the fluid phase regime were prevented by applying constant surface area (NP_zAT) conditions.

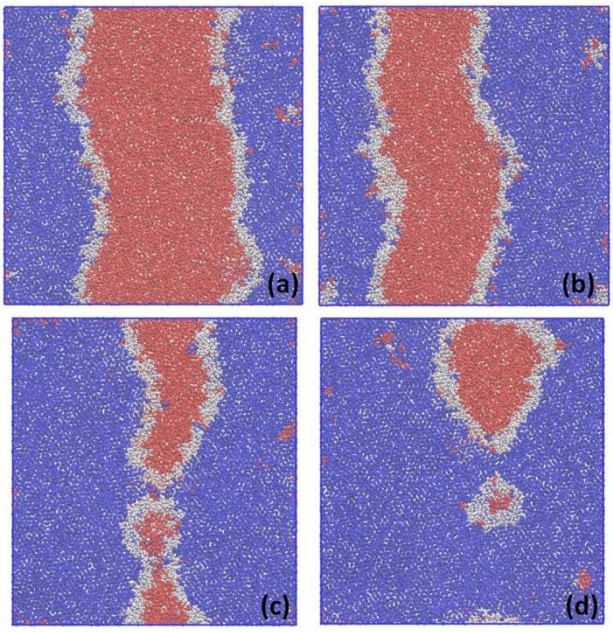

Figure 17. Snapshots of (a) the starting configuration (for all different temperatures) of a continuous fluid stripe bilayer; (b) the final structure at T = 302 K after 500 ns; (c) the structure at T = 301 K after 196 ns when the gel bridge started to form; (d) the final structure at T = 301 K after 500 ns. The colouring scheme is the same as described in Figure 15.

3.3.2 The free energy comparison

At 302 *K*, three types of system as described before were stable for at least hundreds of nanoseconds, enabling their comparison through umbrella sampling. The calculated free energy profile obtained from each system is shown in Figure 18, with the position z = 0 representing the bilayer midpoint. The reference point (G = 0 *kJ/mol*) is set to z = 6 *nm*, which corresponds to the position where the permeant is outside of the bilayer. Permeation across the uniform fluid and the fluid region of a two-phase system arranged in a stripe geometry follow essentially identical free energy profiles, with maxima at 413 ± 3 *kJ/mol*, and 419 ± 5 *kJ/mol*. In contrast, the enclosed fluid domain surrounded by gel has a distinctly lowered free energy barrier with a maximum of 344 ± 3 *kJ/mol*.

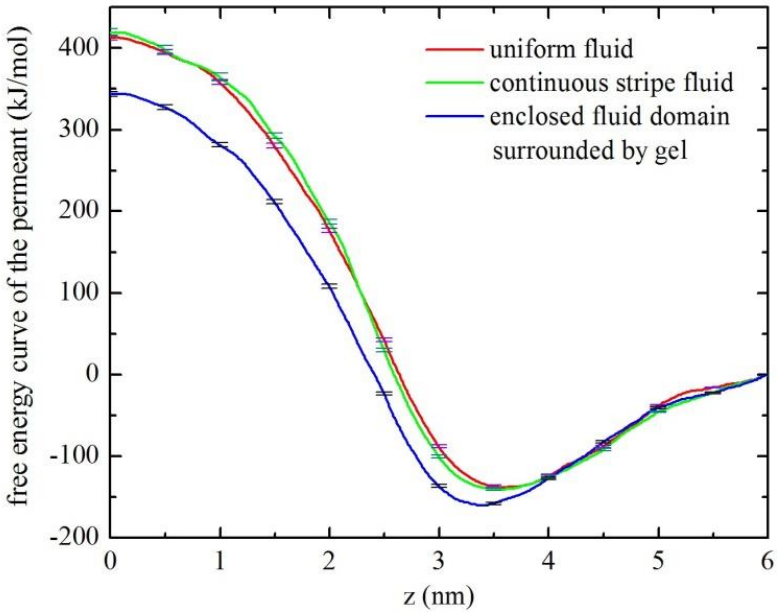

Figure 18. The free energy barrier of the large permeant across the fluid phase of three types of systems. (Here, $z = 0$ corresponds to that the permeant is located in the middle of the bilayer.

3.3.3 Phase change during permeation

To quantify the anticipated changes in phase composition when the permeant enters or leaves the bilayer and the total area is not free to adapt, the fraction of lipids in the fluid phase is plotted against the permeant's position in Figure 19. When the permeant is inserted into the bilayer (from $z_{permeant}$ = 6 to 0 *nm*), the fluid ratio undergoes a decrease for both mixed-phase systems. In the stripe system the change in fluid phase fraction is from 0.491 ± 0.008 to 0.386 ± 0.013, while in the enclosed fluid domain surrounded by gel the change is from 0.185 ± 0.008 to 0.086 ± 0.006. The total fraction change is the same within the error bars, 0.105 ± 0.021 for the stripe fluid and 0.099 ± 0.014 for the fluid domain surrounded by gel, and the shapes of the curves are very similar as well. As anticipated, changes in equilibrium lipid phase composition

appear to simply be a function of how deeply the permeant is inserted, presumably depending on the averaged cross-sectional area of the inserted region.

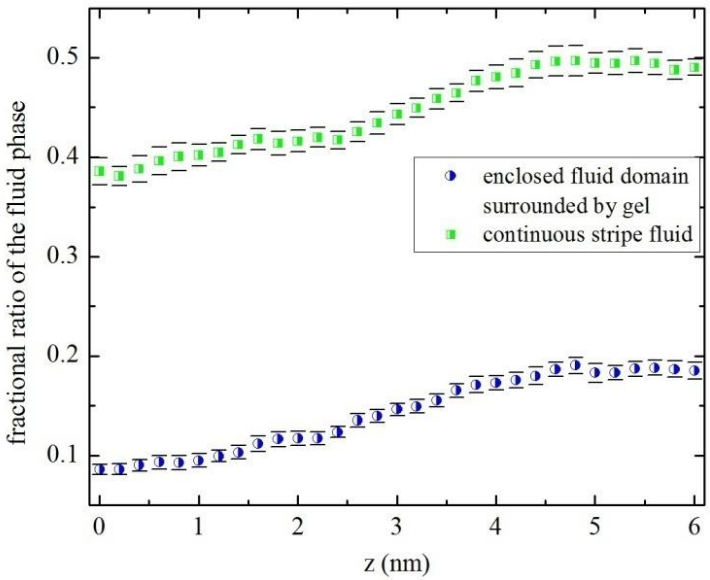

Figure 19. The fractional ratio of the fluid phase vs. the permeant's position.

3.3.4 Temperature dependence

The free energy curve for permeation through an enclosed fluid domain surrounded by gel has been determined at temperatures below T_m, as shown in Figure 20. The barrier drops progressively with temperature, by about 28 *kJ/mol* per degree K. The barrier for a metastable fluid phase bilayer at 298 *K* changes by only 1 *kJ/mol* relative to its value at 302 *K* (data not shown).

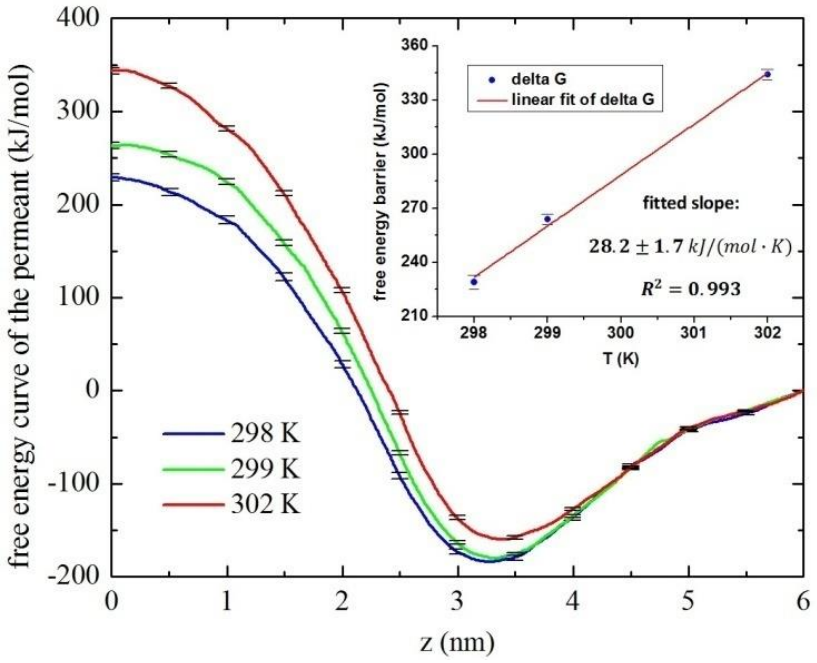

Figure 20. The free energy curve of an enclosed fluid domain surrounded by gel at different temperatures. (Inset figure). fitted free energy barrier change with temperature.

3.3.5 The dynamics of the permeant leaving the bilayer

Since the unbiased insertion of the permeant is far too rare an event for our trajectory times, the dynamics of leaving the bilayer have been studied. Figure 21 displays permeant position vs. time after removal of all restraints from 10 independent trajectories. Average times of arrival at its position of free-energetic minimum were 58 ± 16 *ns* for the uniform fluid bilayer, 51 ± 19 *ns* for the stripe fluid domains, and 76 ± 24 *ns* for the embedded fluid domain. The probability of the permeant coming out from either side was approximately the same.

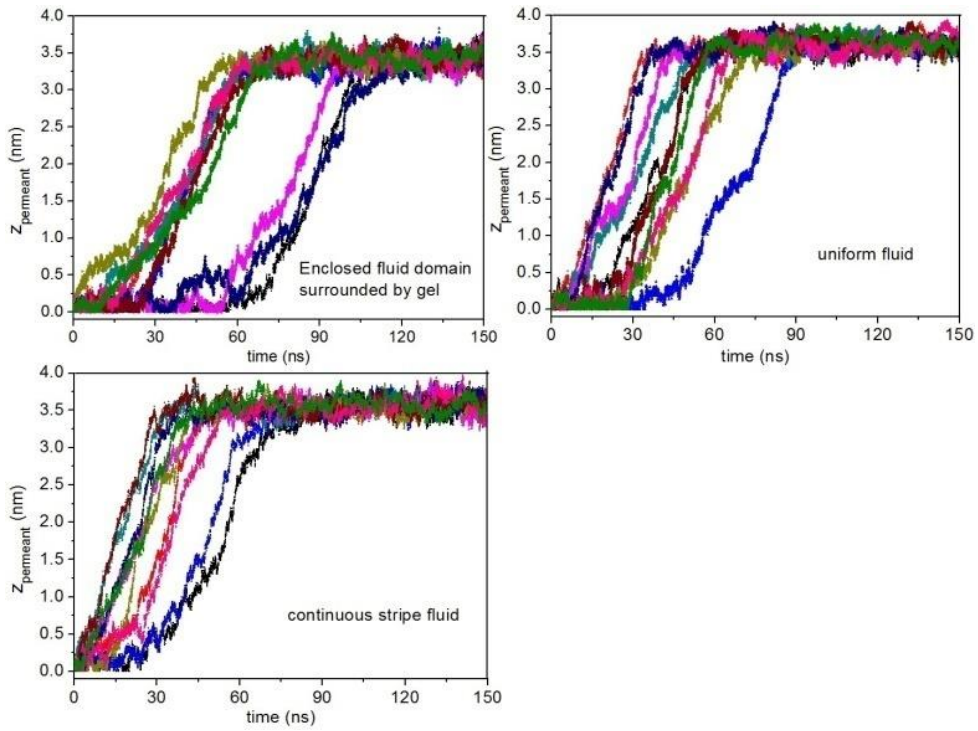

Figure 21. The change of the permeant's center distance with respect to the bilayer center with time.

3.4 Discussions

Umbrella sampling results (Figures 18 and 20) show that the free energy barrier of permeation of a large permeant through a region of fluid lipid bilayer depend, in a temperature-sensitive manner, on the presence and geometry of coexisting gel-phase domains. In the following discussion, we will attempt to explain these results under the assumption that the direct interactions between the permeant and the bilayer are not significantly perturbed by the presence of multiple phases, but rather that the variability reflects the free energy change associated with lipids changing phase in response to the occupation of area by the permeant. This discussion will analyze the

evidence for this hypothesis, and finally address implications for the experimentally observed phenomenon of anomalous bilayer permeability near the transition temperature.

3.4.1 Phase transition temperature

Since free energy changes depend sensitively on the difference between the simulated temperature and the transition temperature T_m, it is important to determine T_m precisely. The originally reported T_m of DPPC bilayer within the MARTINI forcefield was 295 ± 5 K,[75] based on the temperature range of stability of gel-phase domains. That method is subject to some influence from the interfacial line tension, which can resist domain growth even when the bulk free energy for growth is favorable. In this paper, in an attempt to minimize the influence of the line tension, we used a stripe domain geometry,[46] obtaining T_m = 302 ± 1 K. Part of the difference in T_m may be a result of the different versions of MARTINI forcefield.[53, 72] We note that other researchers have also found the phase transition to take place in the 300-305 K range.[51]

3.4.2 Response of phase composition to permeant insertion

The assumption of our previous work[5] based on a course-grain monolayer membrane model is that $N_{switch} = A_P/(a_f - a_g)$, where A_p is the excluded area of the permeant, and $a_f - a_g$ is the area per lipid change of fluid-gel transition. Similarly, for the MARTINI bilayer model, $N'_{switch} = 2A_P/(a_f - a_g)$. For the system of enclosed fluid domain

surrounded by gel, the calculated a_f = 0.589 ± 0.005 nm^2; a_g = 0.4675 ± 0.0003 nm^2; and $A_P = \pi \times 3.017^2$ = 28.6 ± 0.4 nm^2. Therefore, N'_{switch} = 471 ± 20. The simulated N_{switch} = 406 ± 57, using previous analysis (Figure 19). The result agrees relatively well with the assumption.

3.4.3 The origin of difference in free energy barrier

In order to understand the origins in the variations in the free energy barriers in Figure 18, a mesoscale thermodynamic description of the contributions is useful. The free energy of a gel-phase bilayer containing a fluid domain at a certain temperature T in the absence of the permeant can be expressed as:

$$G(L_{out}, T) = N_{f-out} \cdot \mu_f(T) + \left(N_{tot} - N_{f-out}\right) \cdot \mu_g(T) + \Lambda \cdot L_{out} \tag{41}$$

where $N_{f\text{-}out}$ is the total number of the fluid phase molecules when the permeant is outside the bilayer, N_{tot} is total molecule number of the system, Λ is the line tension, L_{out} is the total interfacial length between gel and fluid phase lipids, and $\mu_f(T)$ and $\mu_g(T)$ are the chemical potentials of the fluid phase and gel phase, respectively.

Similarly, the free energy of the configuration where permeant is in the bilayer center can be expressed as:

$$G(L_{in}, T) = N_{f-in} \cdot \mu_f(T) + \left(N_{tot} - N_{f-in}\right) \cdot \mu_g(T) + \Lambda \cdot L_{in} + G_{pore-insert} \tag{42}$$

where $N_{f\text{-}in}$ is the number of lipids remaining in the fluid phase after the permeant is inserted, L_{in} is the interfacial length after insertion, and $G_{pore\text{-}insert}$ denotes the

combined free energy associated in forming a bilayer pore and inserting a permeant into a fluid-phase region of the bilayer.

By subtracting equation (41) from (42), the free energy barrier of the permeant insertion can be written as:

$$\Delta G(L_{out} \rightarrow L_{in}, T) = \left(N_{f-out} - N_{f-in}\right)\left[\mu_g(T) - \mu_f(T)\right] - \Lambda(L_{out} - L_{in}) + G_{pore-insert} \quad (43)$$

As is indicated in equation (43), the first term is a bulk contribution term. At T_m, where fluid and gel phases in the bulk coexist at equal chemical potential, this term equals zero. The second term comes from a line tension contribution, which depends on the change in length of the interface. In all three systems modeled, the permeant only contacts lipids in the fluid phase; the third term, $G_{pore\text{-}insert}$ should be approximately the same. Although for ΔG_{stripe}, the total number of molecules that switched phases N_{switch} = $N_{f\text{-}out}$ - $N_{f\text{-}in}$ is significant in Figure 19, the chosen temperature is very close to T_m, which results in $\Delta\mu_{g\text{-}f} = \mu_g(T) - \mu_f(T) \approx 0$. Also, $L_{out} \approx L_{in}$ for the continuous stripe fluid, as the fluid stripe domain can change in area without changing its interfacial length, causing the line tension term to be also ≈ 0. Therefore, the observation that the free energy of insertion at 302 K is nearly the same for 2-phase and uniform fluid systems at 302 K ($\Delta G_{stripe} - \Delta G_{uniform}$ = 6 ± 6 kJ/mol, as shown in Figure 18) is consistent with equation 43.

Furthermore, comparing ΔG_{stripe} to $\Delta G_{enclosed}$, the bulk term influence should be minimal because N_{switch} is approximately the same in the two geometries, as shown in Figure 19. In contrast, the interfacial energy term has a large influence on $\Delta G_{enclosed}$ but not on ΔG_{stripe}. Here, we will use the differences between the permeability barriers to estimate the line tension. We adopt an approximation by treating the shape of interface as circular (see Figure 22). Therefore,

$$\Delta G_{stripe} - \Delta G_{enclosed} = \Lambda \cdot 2\pi(R_1 - R_2) \tag{44}$$

In order to estimate R_1 and R_2, the total circular area is calculated using the following equation:

$$\pi R^2 = \frac{1}{2}\left(N_{fluid} \cdot a_{fluid} + N_{fluid-interface} \cdot a_{fluid-interface}\right) + \pi R_{permeant}^2 \tag{45}$$

where "a" and "N" denote the average area per lipid and the total molecule number of a phase, respectively. Fluid-interface denotes the part of interface that was originally designated as fluid, $R_{permeant}$ denotes the radius of excluded area of the permeant. These parameters were calculated as described in the Methods section and are given in Table 4. By substituting the numbers in equation (44), the line tension is estimated to be:

$$\Lambda = \frac{(75 \pm 6)\times 10^3 J}{N_A \cdot 2\pi(1.98 \pm 0.24)\times 10^{-9} m} = 10.0 \pm 1.5 \ \ pN \tag{46}$$

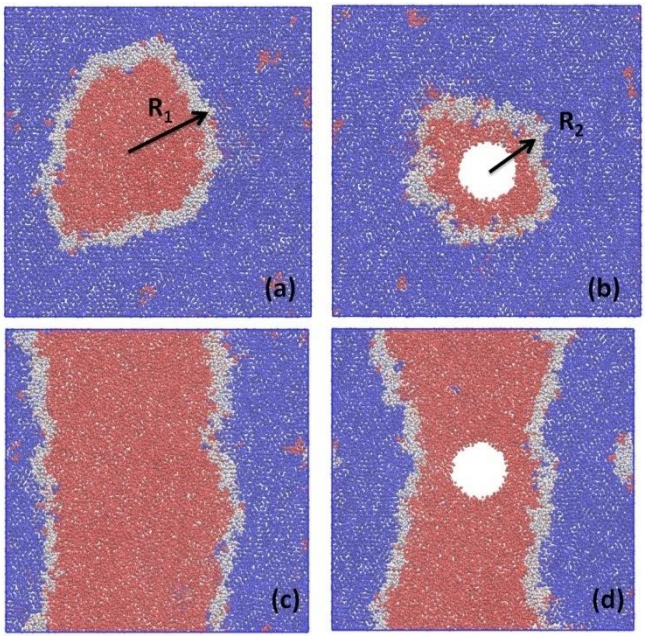

Figure 22. The snapshots of an enclosed fluid domain surrounded by gel at (a) $z_{permeant}$ = 6.0 *nm*, (b) $z_{permeant}$ = 0 *nm*; and a continuous stripe fluid at (c) $z_{permeant}$ = 6.0 *nm*, (d) $z_{permeant}$ = 0 *nm*. (The permeant is not shown. The colouring scheme is the same as described in Figure 15.)

For the above calculation, the irregular shape of the interface has been ignored. Here, we present another method to estimate the line tension constant, which approximates the width of the interface to be the same for all systems. We use the y dimension of the continuous stripe fluid system to scale the interfacial length through the following equation:

$$L = 2L_{y,stripe} \cdot \frac{\langle N_{interface} \rangle_{enclosed}}{\langle N_{interface} \rangle_{stripe}} \tag{47}$$

where $L_{y,stripe}$ = 32.4 *nm*, $N_{interface}$ denotes the average number of interface molecules (determined at 10 *ns* intervals) and $\langle \cdots \rangle$ denotes the ensemble average. Table 6 also lists the parameters used for this calculation. Using those numbers, the calculated L_{out}

- L_{in} = 9.3 ± 3.2 nm. The line tension is then estimated to be:

$$\Lambda = \frac{(75 \pm 6)\times 10^{3} J}{N_A \cdot (9.3 \pm 3.2)\times 10^{-9} m} = 13 \pm 5 \ \ pN \tag{48}$$

By comparing equation (46) to (48), one can see that although these two methods give similar average values, the second estimate has a much larger error bar, due to large fluctuations of the interfacial length, and the deviation of the interfacial shape from a perfect circle. Our estimate is higher than the previously reported value (3 ± 2 pN) by Marrink and co-workers[75] (obtained using an older version of the Martini forcefield[53]), but matches a recent estimate (11.5 ± 0.5 pN) obtained by analysis of the fluctuations of the gel-fluid interface.[74]

Method 1→ equation (46)		
Umbrella window	$z_{permeant}$ = 6 nm	$z_{permeant}$ = 0 nm
$a_{fluid}(nm^2)$	0.592 ± 0.005	0.586 ± 0.008
N_{fluid}	770 ± 33	351 ± 23
$a_{fluid\text{-}interface}(nm^2)$	0.532 ± 0.008	0.533 ± 0.009
$N_{fluid\text{-}interface}$	173 ± 12	143 ± 11
$R_{permeant}$ (nm^2)	0	3.017 ± 0.021
$A_{total}(nm^2)$	274 ± 10	170 ± 8
$R(nm)$	R_1 = 9.34 ± 0.17	R_2 = 7.36 ± 0.17
Method 2 → equation (46)		
$\langle \boldsymbol{N_{interface}} \rangle_{\boldsymbol{stripe}}$	$\langle \boldsymbol{N_{interface}} \rangle_{\boldsymbol{enclosed}}$ ($z_{permeant}$ = 6 nm)	$\langle \boldsymbol{N_{interface}} \rangle_{\boldsymbol{enclosed}}$ ($z_{permeant}$ = 0 nm)
409 ± 8	339 ± 12	280 ± 16

Table 6. Parameters for estimating the change of interfacial length for the system of enclosed fluid domain surrounded by gel.

In shifting temperature below T_m, we should be able to can re-introduce the bulk contribution. For small variations in temperature, $\Delta\mu_{g\text{-}f}$ can be estimated to be:

$$\Delta\mu_{g-f} = \Delta s \cdot \Delta T = \frac{\Delta h}{T_m} \cdot \Delta T \tag{49}$$

where Δs and Δh are the entropy and enthalpy per lipid of the gel-fluid transition and $\Delta T = T - T_m$.

We find Δh = 25.8 *kJ/mol*, leading to $\Delta\mu_{g\text{-}f}$ = 0.085 ± 0.005 *kJ/mol* (when ΔT = 1 *K*). Given the number of lipids that undergo the fluid-gel transition upon insertion of permeant (N_{switch}), is approximately 400, we expect a favourable bulk contribution for inserting the permeant of 34 *kJ/mol* per degree below T_m. The simulations, as shown in Figure 18, showed a somewhat weaker, but comparable temperature dependence to the barrier of 28.2 ± 1.7 *kJ/mol*.

The similar timescales required for the permeant to move from the peak of the free energy barrier to the free energy well in the fluid and mixed-phase cases (Figure 19) suggest that the rate of interconversion between phases, necessary to accommodate the change in available area, has at most a modest slowing effect on the dynamics of permeant passage. The effect of the coexisting phases on permeation rate is therefore dominated by the difference in the free energy barriers. The difference of 75 kJ/mol (30 k_BT) in free energy barriers for this example is enormous and translates into a difference in local permeability of many orders of magnitude. This particular example

is unrealistic for a system at thermal equilibrium, because the total interfacial energy of the original domain is even greater than this, and so equilibrium probability is vanishingly rare. The same principle will be at play, however, for smaller permeants in systems characterized by a smaller interfacial line tension, in which case thermal fluctuations can allow a significant presence for fluid phase domains with interfacial energies several times k_BT. At temperatures slightly below T_m, the favorable bulk effect will further contribute to lowering the permeability barrier (while also simultaneously decreasing the probability that a large fluid domain will appear through an equilibrium thermal fluctuation). Future work to obtain numerical predictions of permeability vs. temperature near T_m will require combining estimates of the fluid domain size distributions based on statistical thermodynamics with the estimated permeation enhancement factors (from both interfacial and bulk contributions) outlined here.

The possibility should be noted that this mechanism may play a role via *non*-equilibrium persistent fluid-phase domains, analogous to the fluid-phase island shown in Figure 17d, which is very slow to transition to the gel phase because of the rigidity of its surroundings. A vesicle undergoing the fluid-gel transition is not subject to the same constraints as a periodically repeating simulation box, but nonetheless relaxation of fluid-phase regions surrounded by rigid gel may still be slow under some conditions. Finally, we should acknowledge that neither this nor other treatments of

this anomaly address the possible involvement of the ripple phase.[79]

3.4.4 Implications for permeability through a single fluid domain

The simulation results show that the free energy profile for the permeation of a large particle, at or below T_m, is significantly reduced when the permeation takes place in a fluid domain embedded in an ordered phase with lower area per lipid. The discussion above relates the magnitude of this shift to the changes in interfacial and bulk free energies that stem from the reduction in the domain's perimeter and area. Here we consider more specifically the implications for the permeability of an embedded fluid domain relative to that of the pure fluid phase.

As presented by Marrink and Berendsen[19], the inverse permeability (or permeation resistance) can be related to an integral over the normal (z) dimension of the bilayer of the Boltzmann weight over the diffusivity:

$$P^{-1} = \int_{-z_0}^{z_0} \frac{exp(F(z)/RT)}{D(z)} dz \tag{50}$$

where $F(z)$ is the free energy relative to the solute in bulk water and $D(z)$ is a local diffusivity of the solute normal to the bilayer. One aspect of equation (50) to note is that the integral will be dominated by the value of F (the free energy relative to that in the bulk) at and near the barrier maximum. It may be surprising that this value, and not the height of the barrier relative to its value at the free energy minimum where the permeant is adsorbed to the bilayer, is most important. Although the barrier to

crossing faced by a permeant is increased by the presence of this minimum (reducing its average rate of passage over the barrier by a factor of exp (F_{min}/RT) within the transition-state theory approximation), the concentration of adsorbed permeants in the well is enriched at equilibrium over the bulk concentration by the same factor. To a first approximation, therefore, only changes to the barrier maximum (relative to the bulk) and not changes to the local minima need to be considered in estimating changes to permeability.

We have not attempted to calculate the local diffusion rate $D(z)$, which might be expected to be affected by the coupling of the normal motion of the permeant to the changes in phase composition observed in the two-phase systems. The observation that the mean times needed for the permeant to exit the bilayer once released at the midplane were in rough (within 50%) agreement suggests that the effective diffusivities do not differ too strongly. So, it is a good first approximation to say that the permeability of an embedded fluid domain will be increased over the permeability of a pure fluid patch of bilayer by a factor corresponding to the ratio of their Boltzmann weights at the maximum:

$$\frac{P_{embedded}}{P_{purefluid}} = \frac{exp[-F_{embedded}(0)/RT]}{exp\left[-F_{pure\ fluid}(0)/RT\right]} \tag{51}$$

The difference in free energy barriers of 75 *kJ/mol* (30 k_BT) for this example is enormous and translates into a difference in local permeability of many orders of magnitude.

3.4.5 Implications for permeability through an ensemble of domains

This particular example is unrealistic for a system at thermal equilibrium for several reasons. For one, the total interfacial energy of the original domain is even greater than this, and so the probability that it would exist at equilibrium is vanishingly rare. For another, the absolute value of the barrier to permeation is so large that the permeation rates even through the lowered barrier would be vanishingly small. The same influences of line tension will be at play, however, for smaller permeants in systems characterized by a smaller interfacial line tension. The essential question is whether domains large enough to accommodate the permeant will have interfacial energies low enough to be produced by typical thermal fluctuations. To show that this question can plausibly be answered in the affirmative, we have used a simple statistical thermodynamic model for the equilibrium distribution of fluid domains under the influence of a given line tension while taking into account the excluded area between domains within the second virial approximation.

3.4.6 Statistical thermodynamic model for distribution of domain sizes

A circular fluid domain with s lipids in each leaflet has area $s \times a_{fl}$ and circumference $(4\,\pi a_{fl} s)^{1/2}$. It is convenient to define a dimensionless line tension λ as:

$$\lambda = \sqrt{4\pi a_{fl}}\Lambda / k_B T \tag{52}$$

so that the interfacial free energy of the domain equals $\lambda s^{1/2}$ in units of $k_B T$. Given reasonable choices (a_{fl} = 0.65 nm^2, T=310 K), λ corresponds to the actual line tension

Λ in piconewtons divided by 1.5. At T=T_m, the free energy per domain does not depend directly on domain area s because the chemical potentials of gel and fluid lipids are equal.

Using a lattice model approximation for the entropy of mixing, *i.e.* assuming that there are M distinct choices (corresponding to the sites of M lipids on the gel-phase lattice) for the positions of the center of each fluid domain, the free energy at T_m of a system where each size s is represented by N_s domains is:

$$F/k_BT = \sum_{s=s_{min}}^{\infty} N_s(-ln\, M + ln\, N_s - 1) + N_s\lambda s^{1/2} \tag{53}$$

where interactions (including excluded area, or overlaps) between domains have been neglected. The model is therefore only applicable at low surface coverage of fluid domains. Dividing by the total lattice size M gives a free energy per lipid f:

$$f/k_BT = \sum_{s=s_{min}}^{\infty} c_s\left(ln\, c_s - 1 + \lambda s^{1/2}\right) \tag{54}$$

with $c_s = N_s/M$ as the concentration of domains of size s. Minimizing f with respect to each c_s yields:

$$c_s = exp\left(-\lambda s^{1/2}\right) \tag{55}$$

The total area fraction Θ_{fluid} associated with domains of all sizes can be approximated by treating s as a continuous variable and integrating $s \times c_s$ from s_{min} to ∞, yielding:

$$\Theta_{fluid} \approx \frac{2e^{-\lambda {s_{min}}^{\frac{1}{2}}}}{\lambda^4}\left(6 + 6\lambda {s_{min}}^{\frac{1}{2}} + 3\lambda^2 s_{min} + \lambda^3 {s_{min}}^{\frac{3}{2}}\right) \tag{56}$$

The ideal approximation is not very good at area fractions greater than 5-10%, so we

treat excluded area interactions using the second virial approximation.[80] An additional "excluded area" term is added to the free energy of equation (53):

$$\frac{f_{xv}}{k_B T} = \sum_{s=s_{min}}^{\infty} c_s \sum_{s'=s_{min}}^{\infty} c_{s'} b_{ss'} \tag{57}$$

where $b_{ss'}$ is the second virial coefficient for the interactions of a hard disk with scaled area s and one with scaled area s':

$$b_{ss'} = \frac{1}{2} a_f \left(s + 2\sqrt{s}\sqrt{s'} + s' \right) \tag{58}$$

Adding the excluded volume contribution to equation (54) and proceeding to optimize the free energy per unit area with respect to c_s gives:

$$c_s = exp(-s\Sigma_1)\, exp\left[-(\lambda + \Sigma_2)s^{1/2}\right] exp(-\Sigma_3) \tag{59}$$

where the summations are introduced:

$$\Sigma_1 = \sum_{s'=s_{min}}^{\infty} c_{s'} \,;\, \Sigma_2 = \sum_{s'=s_{min}}^{\infty} 2\sqrt{s'} c_{s'} \,;\, \Sigma_3 = \sum_{s'=s_{min}}^{\infty} s' c_{s'} \tag{60}$$

The values of c_s in equation (59) need to be solved self-consistently with the summations in equation (60). We have done this through numerical iteration, explicitly calculating the Σ values in equation (60) as discrete sums over s' and then refining the estimates of $c_{s'}$ using equation (59).

The results are quite sensitive to the choice of s_{min}. This minimum domain size should not be confused with a critical nucleation threshold for domain stability[75] (which diverges at T=T_m) but rather is the minimum number of lipids needed to even define a local fluid phase region. To define s_{min} as a lower bound to domain size implies that the free energies of domains smaller than s_{min} deviate sharply upwards from the

proportionality to $s^{1/2}$ that governs larger domains. The physical justification for this deviation is that the stability of the fluid phase (relative to the gel phase) arises from the conformational freedom of the lipids, which is largely restricted in the confined environment of a very small domain. It is clearly nonsensical to define a fluid domain containing a single lipid, so $s_{\min} > 1$, but there is no obvious choice for the demarcation. Here we will follow Kharakoz and Shlyapnikova, who find good fits to a number of experiments assuming a minimum domain size of 7 for gel-in-fluid domains[81] (even though the minimum for the fluid-in-gel case need not be the same).

3.4.7 Calculation of permeability from domain size distribution

The number of fluid-phase lipids per leaflet that must join the gel phase to free up enough area A_p to accommodate the permeant, as discussed above, is $N_{switch} = A_p/(a_{fl}-a_{gel})$. The final area enclosed by the fluid domain that contains s lipids before insertion of the permeant is $A_p + (s - N_{switch})\, a_{fl}$. If s_p is the permeant area in units of a_{fl}, this final area simplifies to $s - \alpha\, s_p$ in the same units, where we have defined:

$$\alpha = a_{gel}/(a_{fl} - a_{gel}) \tag{61}$$

Since the final area cannot be less than s_p, the smallest size domain s_0 that will permit permeation will be:

$$s_0 = (1 + \alpha)s_p \tag{62}$$

Since the gel/fluid interfacial energy F_{int} is given by $\lambda s^{1/2}\, k_B T$, its change upon from insertion of the permeant is:

$$\Delta F_{int}/k_B T = \lambda\left(\sqrt{s - \alpha s_p} - \sqrt{s}\right) \quad (63)$$

The enhancement of the rate of permeation is, we assume, $\exp(-\Delta F_{int}/k_B T)$. So, summing over the area fraction ($s \times c_s$) occupied by of domains of size s, weighted by the permeability of that size domain relative to the pure fluid phase, we can find the overall rate of permeation through the fluid-in-gel phase relative to the pure fluid phase:

$$\frac{P}{P_{fluid}} = \sum_{s=s_0'}^{\infty} s c_s e^{-\beta \Delta F_{int}(s)} \quad (64)$$

The lower bound to the summation, s_0', should be defined as the greater of s_{min} and s_0.

3.4.8 Predictions from statistical thermodynamic theory

Figure 23 shows the predicted permeability of the fluid-in-gel phase relative to that of the pure for three values of the scaled line tension λ. The curves show cusps at $s_p = s_{min}/(1+\alpha)$, *i.e.* where the minimum domain size present in the mixture matches the minimum domain size that can accommodate the permeant. The sharpness of the peak is an artefact of enforcing a sharp lower cut-off in the domain size distribution, but the peak itself reflects real physical trends: the enhancement due to line tension increases with permeant size whereas the fraction of fluid domains that are large enough to accommodate the permeant decreases with permeant size. At λ=2.4 (corresponding to Λ= 3.6 *pN*, as derived from acoustic measurements on DPPC[81]), the permeability only reaches at most about 75% that of the pure fluid, but is still greatly enhanced compared to the fluid domain area fraction of 4.2%. At somewhat lower line tensions

of λ=2.0 and 1.6 (corresponding to Λ= 3.0 *pN* and 2.4 *pN*, and generating fluid domain area fractions of 11.5 and 25.1% respectively) an absolute enhancement over pure-fluid phase permeability is predicted over a range of permeant areas. The equations used to find these values contain many approximations, any of which might either enhance or suppress this apparent anomalous permeability if treated in greater detail, but the order of magnitude of the effect shown in Figure 23 is enough to show that line tension is definitely one contributor to anomalous permeability, and could be its most important cause.

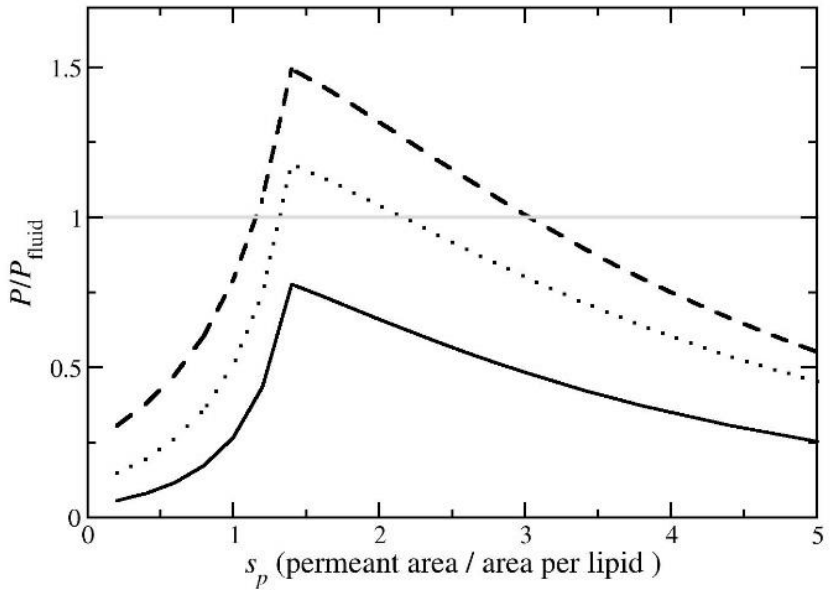

Figure 23. Permeability of a gel phase containing embedded fluid domains at T_m, relative to pure fluid bilayer permeability, evaluated using equation (64) as a function of scaled permeant area s_p. Minimum domain size is assumed to be s_{min} = 7. As defined in equation (61), α=4. Solid, dotted, and dashed curves correspond to scaled line tension values λ = 2.4, 2.0, and 1.6, which yield fluid area fractions of Θ_{fluid}= 0.042, 0.115, and 0.251 respectively.

3.4.9 Complicating factors

A number of confounding factors may be at play that are not captured in the simple thermodynamic treatment of the phenomenon presented above. One is the possibility of non-equilibrium effects. At temperatures below T_m, the favourable free energy of the fluid- to-gel transition for lipids throughout the domain (the bulk contribution of eq. 11) will further contribute to lowering the permeability barrier – although it will also reduce the probability that a large fluid domain will appear through an equilibrium thermal fluctuation. If some fluid-phase domains persist out of equilibrium as temperature decreases, this bulk effect may become quite large. We see this persistence in the simulations, as in the case of the fluid-phase island shown in Figure 17(d), which is very slow to transition to the gel phase because of the rigidity of its surroundings. A vesicle undergoing the fluid-gel transition in an experiment is not subject to the same constraints as a bilayer patch in a periodically repeating simulation box; nonetheless, relaxation of fluid-phase regions surrounded by rigid gel may still be slow under some conditions and so non-equilibrium effects may play a role below T_m.

Other complicating factors include curvature, which in the case of small vesicles in particular may have significant influence on domain structure and transition temperatures.[82] In multi-component bilayers (including nominally uniform bilayers with small amounts of impurity) the changing composition of the fluid phase over the course of the phase transition can produce an important enhancement of

permeability.[83] Finally, we should acknowledge that the ripple phase,[79] intermediate in structure between gel and fluid, may play a role that is not accounted for in the present two-phase picture.

3.5 Conclusions

The barrier to passage of a large permeant through the fluid phase of a bilayer containing coexisting fluid and gel regions can be strongly influenced by the presence of the coexisting phases, even when the permeant only interacts with the fluid phase, if its passage promotes a shift in phase composition. A reduction of the barrier that depends on the dimension and geometry of the fluid phase region and the temperature relative to T_m can be related to bulk and/or interfacial contributions from the change in domain size. Analysis of these contributions led to an estimate of the line tension at the gel/fluid interface of about 10-13 pN for the Martini model DPPC bilayer, close to an independently calculated value.[73-74] Similarly, both the permeation free energy results and stripe domain growth simulation results are in agreement on a gel-fluid transition temperature of 302 K for this model. The effects discussed here provide a framework for relating the experimentally known phenomenon of enhanced permeability near T_m to a few thermodynamic and structural parameters. A simple statistical thermodynamic model confirms the plausibility of this explanation. In particular, the model predicts that, using parameters leading to a thermal distribution of fluid domains covering 11-25% of the area of a mostly impermeable gel-phase

bilayer, the average permeability of the mixed phase exceeds that of a pure fluid bilayer over a range of permeant sizes.

Chapter 4

The 2d-umbrella sampling of a sodium ion across the bilayer

The free energy calculation of a sodium ion across a DPPC bilayer has been performed with molecular dynamics simulations to elucidate the path of permeation processes that involves a distinct change in the bilayer structure. The proposed transition structure for ion permeation is a symmetric "double-dimple" structure in the bilayer when the sodium ion is in the middle of the bilayer. 2d-umbrella sampling simulations have suggested a reaction path to form this structure and estimated the relative free energy changes. This method provides a reasonable estimate of the free energy barrier for the ion permeation.

4.1 Backgrounds

A longstanding goal of lipid bilayer studies has been the elucidation of bilayer permeabilities for a group of substances.[12-13, 15, 19, 35, 84-90] Several experiments have been performed to study the permeation process of water or ions.[12-13, 15, 35, 88-90] The experimental permeability of the water across a DPPC bilayer (T = 308 K) lies in the range: $1.3\times10^{-3} - 4\times10^{-2}\ cm/s$.[12-13, 15, 88-89] The sodium ion permeability is measured to be $10^{-14} - 10^{-12}\ cm/s$.[35, 90], much smaller than the water permeability. Considering the inhomogeneity of the DPPC membrane interior,[91-92] Marrink and Berendsen performed a simulation to calculate the water permeability to

be $(7 \pm 3)\times10^{-3}\ \ cm/s$ at 350 K.[19] Using a combination of different methods, the calculated free energy barrier of this process was 26 *kJ/mol*.[19] Different from the water molecule, accurate free energy calculations are relatively scarce in literature for the ion because of the known convergence problem.[6]

The aim of this study is to develop an effective method to calculate the free-energy barrier of a sodium ion and relate the results with experiments.[93-95] Permeation processes of the sodium ion are complicated because a large change in the bilayer structure is accompanied with it. Simulations have revealed that an aqueous indentation (dimple structure) on one side of the bilayer is formed as the ion penetrates into the bilayer center.[96] This dimple structure formation is known to reduce the free energy to a great extent by just using a simple continuum dielectric model[97] in which the bilayer and the bulk water are characterized by different dielectric constants and separated with a flat boundary. The formation and the disappearance of the dimple structure is a slow process which will cause convergence problem in umbrella samplings. In particular, the transition of the dimple from one leaflet to the other, whether through a symmetric or asymmetric transition state, presents a barrier that is orthogonal to the default 1-d reaction coordinate along the bilayer normal. A simulation time of 50 *ns* for each umbrella sampling window is still not yet enough to achieve convergence when the charged particle is near the bilayer center.[6] This difficulty in using 1d-umbrella sampling calls for a new approach. The

accurate free energy calculation for ions requires a more realistic, reversible path. According to the symmetry of the DPPC bilayer, a reasonable transition structure formation should cost the same free energy when the sodium ion penetrates from either side of the bilayer. Such a structure could be a double aqueous indentation (double dimple structure) on both leaflets where the sodium ion is right in the center. This structure agrees with literatures[84, 98] which propose the "pore-mediated" mechanism for ion transportation. A study of sodium ion penetration has been performed in a pure fluid DPPC bilayer system using 2d-umbrella sampling method to incorporate both the ion and lipid coordinates.

4.2 Simulation methods

4.2.1 Simulation system set up

The molecular dynamics method was used for the ion permeation study using Gromacs[64] version 4.5.4 and Berger force field.[99] The simulation system contains a sodium ion, a chloride ion, 128 DPPC molecules and 3653 water molecules. The simple point charge model was applied to the water molecules by using SETTLE algorithm.[100] All systems were run using isobaric-isothermal (NPT) ensemble, with the control of Berendsen temperature coupling and Berendsen anisotropic pressure coupling[101] which allows the bilayer to expand or contract independently in all dimensions. The reference temperatures of all groups were set to 308 *K* (apparent T_m value for the Berger force field DPPC bilayer systems)[46] by a time constant of 0.2 *ps*.

The reference pressures of all groups were 1 bar with all compressibilities set to $4.5\times10^{-5}\ bar^{-1}$ with a time constant of 2 ps. Neighbor lists, van der Waals radii and Coulombic cutoffs were all set to 1 nm. Particle Mesh Ewald sums[102] were used in electrostatics calculation with a $0.12\ nm$ of Fourier spacing and a 4^{th} order (cubic) interpolation. The time step used for all the simulations was 2 fs.

4.2.2 2d-umbrella sampling

The free energy calculations which used 1d-umbrella sampling and WHAM algorithm has been discussed in the **Main Introduction, section 1.8.4**.[59-60] Similar to the set-up of 1d-umbrella sampling, a series of harmonic potentials was applied to the sodium ion with their minima distributed along the bilayer surface normal (Z direction). The sodium coordinate (Z^{Na}) was defined as the Z-axis position of the center of mass of the sodium ion, relative to that of the DPPC bilayer. In terms of the phosphate coordinate (Z^{P}), five phosphate atoms from the upper leaflet that are laterally closest to the sodium ion were chosen. Z^{P} was defined as the Z coordinate of their center of mass, relative to that of the DPPC bilayer (Figure 24). Another set of harmonic potentials were used to bias Z^{P}. The full expressions for 2D-WHAM are:

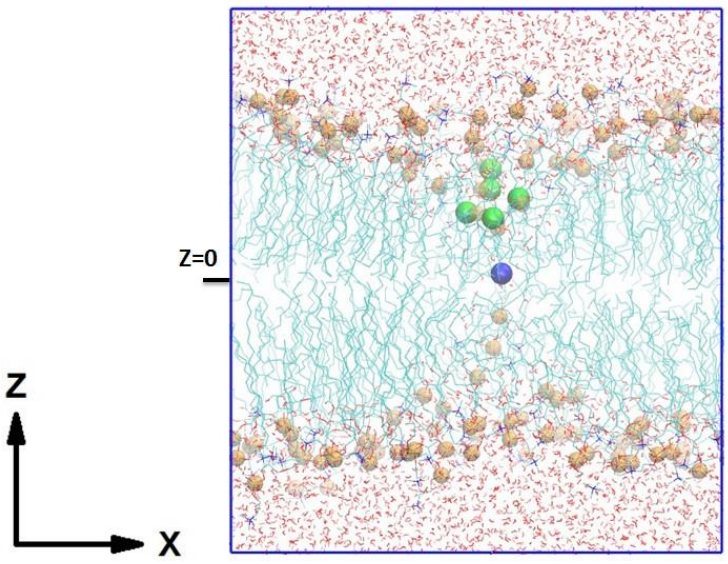

Figure 24. Side view (X-Z plane) of a sodium ion (blue sphere) around the lipid center. Orange spheres: all phosphates; green spheres: phosphates used as lipid coordinate Z^P.

$$p(z^{Na}, z^P) = \frac{\sum_{i=1}^{N} \boldsymbol{h_i}(z^{Na}, z^P)}{\sum_{j=1}^{N} \boldsymbol{n_j} f_j \, exp\left\{-\beta\left[\frac{1}{2}K_j^{Na}\left(z^{Na} - z_j^{Na}\right)^2\right]\right\} exp\left\{-\beta\left[\frac{1}{2}K_j^{P}\left(z^{P} - z_j^{P}\right)^2\right]\right\}} \tag{65}$$

$$\frac{1}{f_j} = \sum_{z^{Na}} \sum_{z^P} p(z^{Na}, z^P) \, exp\left\{-\beta\left[\frac{1}{2}K_j^{Na}\left(z^{Na} - z_j^{Na}\right)^2\right]\right\} exp\left\{-\beta\left[\frac{1}{2}K_j^{P}\left(z^{P} - z_j^{P}\right)^2\right]\right\} \tag{66}$$

where N is the total number of umbrella histograms used; $p(Z^{Na}, Z^P)$ is the unbiased probability distribution; $\frac{1}{2}K^{Na}{}_j\left(Z^{Na} - Z^{Na}{}_j\right)^2$ and $\frac{1}{2}K^{P}{}_j\left(Z^{P} - Z^{P}{}_j\right)^2$ are the biasing potentials of the sodium ion and the phosphates in the j^{th} simulation respectively; $\boldsymbol{h}_i(Z^{Na}, Z^P)$ is the number of data points of histogram i at position (Z^{Na}, Z^P); $\mathbf{n}_j$ is the total number of data points of histogram j and f_j is a normalization factor for the biased probability distribution of the j^{th} simulation. The

WHAM equations should be solved iteratively until reaching self-consistency. After solving $\mathrm{p}(\mathrm{Z}^{\mathrm{Na}}, \mathrm{Z}^{\mathrm{P}})$, the free-energy surface is constructed by choosing a reference position $(\mathrm{Z}^{\mathrm{Na}}{}_0, \mathrm{Z}^{\mathrm{P}}{}_0)$:

$$\Delta G(Z^{Na}, Z^{P}) = G(Z^{Na}, Z^{P}) - G(Z^{Na}{}_0, Z^{P}{}_0) = -k_B T \ ln\frac{p(Z^{Na}, Z^{P})}{p(Z^{Na}{}_0, Z^{P}{}_0)} \qquad (67)$$

1D-WHAM data was plotted using the program g_wham[60] while 2D-WHAM data was plotted using a self-written code in Labview. The uncertainty is estimated from the umbrella histograms using bootstrap analysis[60, 103], which is a method to generate random hypothetical observations based on current data.

The simulation time of the MD run in each of the umbrella sampling window is 5 ns. The parameters used for this study is: K_i^{Na}=1000 or 500 *kJ/mol*; ΔZ_i^{Na}=0.1 or 0.15 *nm*; K_i^{P}=500 *kJ/mol*; ΔZ_i^{P}=0.1 *nm*, where ΔZ denotes the gap between the harmonic potential minima.

4.3 Results and discussions

4.3.1 1d-umbrella sampling

The free energy curve of the sodium ion across a DPPC bilayer is shown in Figure 25 (Left). This calculation is based on 1-d umbrella sampling in which only the sodium ion coordinate (Z^{Na}) is used. Specifically, Z^{Na} is the center of mass position in the Z axis of the sodium ion with respect to that of the DPPC bilayer. The calculated free energy barrier is 61 ± 2 (kJ/mol) for the sodium ion to go from the lipid

headgroup region to the bilayer center. A snapshot when the sodium ion is in the middle of the bilayer is also given in Figure 25 (Right). A clear dimple structure is observed with the sodium ion being partly solvated. The free energy of the sodium ion undergoes a continuous increase in the region of $\mathrm{Z^{Na}} = 0.0 - 0.4\ nm$, with a corresponding dimple structure continuously growing on the lower leaflet. At the position $\mathrm{Z^{Na}} = 0.4\ nm$, starting configurations with the opposite dimple side yield completely different umbrella histograms in a 5ns MD simulation (results not shown). This hysteresis may come from the slow relaxation in degrees of freedom orthogonal to the chosen reaction coordinate of the sodium ion.[77, 104]

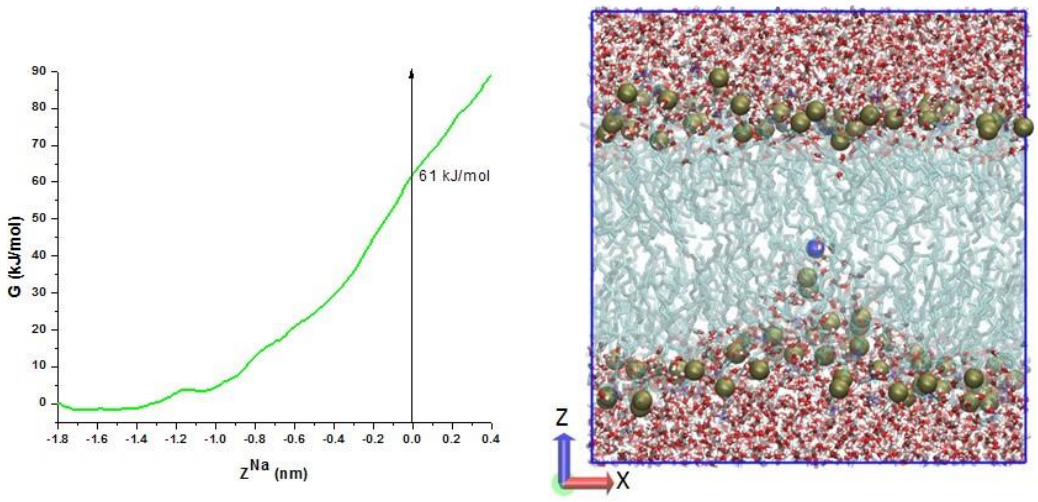

Figure 25. **Left:** free energy curve of the sodium ion across a pure fluid DPPC bilayer using 1d umbrella sampling with harmonic constants $K_i^{Na} = 1000\ kJ/(mol \cdot nm^2)$; the spacing between harmonic potential minima $\Delta Z_i^{Na} = 0.1\ nm$. Sodium ion coordinate Z^{Na} denotes the center of mass position in Z axis of the sodium ion with respect to that of the DPPC bilayer, $G_{Z^{Na}=0nm} - G_{Z^{Na}=-1.8nm} = 61 \pm 2\ (kJ/mol)$.

Right: side view of a sodium ion located in the middle of the bilayer with a dimple structure formed on one side.

4.3.2 2d-umbrella sampling

The 2d-umbrella sampling windows were chosen to sample the area along the reaction coordinate. The calculated free energy surface in terms of both the sodium coordinate (Z^{Na}) and the phosphate coordinate (Z^{P}) is shown in Figure 26. The position of $Z^{Na} = 0nm$ corresponds to the bilayer center while $Z^{Na} \approx -1.5\ nm$ corresponds to the headgroup region of the lower leaflet. The flat structure of the upper leaflet corresponds to $Z^{P} \approx 1.8\ nm$ and a symmetric double dimple structure corresponds to $Z^{P} \approx 1.0\ nm$, $Z^{Na} \approx 0.0\ nm$ (see Figure 24). The contour plot in Figure 26 shows a minimum energy path for ion permeation from $Z^{Na} = -1.5\ nm$ to $Z^{Na} = 0.0\ nm$ that corresponds to $Z^{P} \approx 1.8\ nm$. The lowest free energy is located when the sodium ion is in the lipid headgroup region, as shown in the pink shaded area. Assuming Z^{P} remains unchanged, the free energy cost for the sodium ion to go from the headgroup region to the lipid center is approximately $60\ kJ/mol$ which matches with the 1D-umbrella sampling data. Interesting to note is that the cost of free energy is not too high (around $10\ kJ/mol$) to bring in another dimple structure from the upper leaflet. Particularly, in the region where Z^{Na} is around $0.0\ nm$ and $Z^{P} = 1.0 - 1.3\ nm$, which corresponds to the structure of a fully formed dimple on the lower side and a smaller dimple on the upper side, the free energy surface becomes nearly flat. The reason for this might be that the strong attractions between the sodium

ion and the upper headgroups compensates the free energy cost of the curvature change and the reorientation of lipid tails involved in the complete formation of the upper dimple. The overall free energy cost for the sodium ion to go into the center and to form a double dimple structure is approximately $65 - 70\ kJ/mol$. However, it remains to be proven that the current double-dimple structure is at a maximum in the free energy landscape where it would have equal probability of crossing to the opposite side or returning to the lower side.

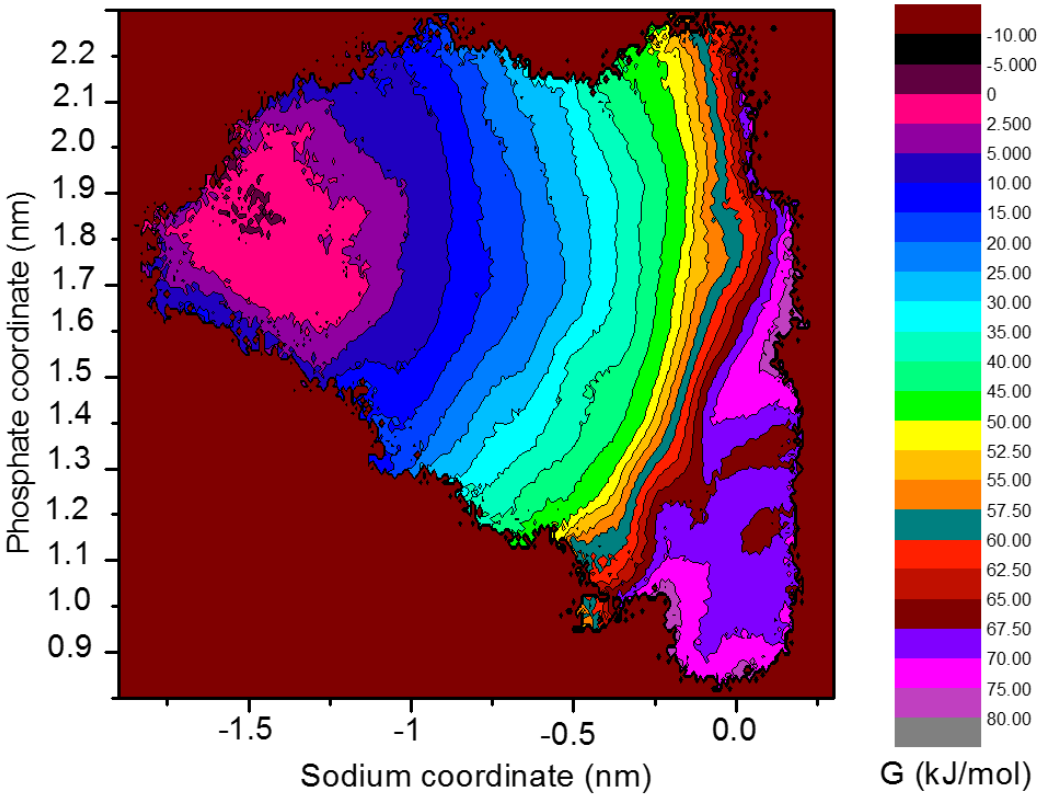

Figure 26. Free energy surface of the sodium ion in terms of both the sodium and phosphate coordinates. (K_i^{Na}=1000 or 500 *kJ/mol*; ΔZ_i^{Na}=0.1 or 0.15 *nm*; K_i^P=500 *kJ/mol*; ΔZ_i^P=0.1 *nm*)

4.3.3 The reverse process sampling

For the retreating process of the double dimple structure, the phosphate coordinate was defined in terms of five phosphate atoms of the lower leaflet that are laterally closest to the sodium ion. Since the coordinate is flipped to the lower side, we add a negative sign to the coordinate. The free energy landscape of the sodium ion retreating from the bilayer center to the upper leaflet is shown in Figure 27 (right). For comparison, the color scheme set the same at the symmetric double dimple position ($\mathrm{Z^P} \approx -1.0\ nm,\ \mathrm{Z^{Na}} \approx 0.0\ nm$) as that ($\mathrm{Z^P} \approx 1.0\ nm,\ \mathrm{Z^{Na}} \approx 0.0\ nm$) in Figure 27 (Left). The free energy has decreased to ≈50 *kJ/mol* at $\mathrm{Z^P} \approx -1.8\ nm,\ \mathrm{Z^{Na}} \approx 0.5\ nm$. However, the insertion process of the sodium ion at $\mathrm{Z^P} \approx 1.8\ nm,\ \mathrm{Z^{Na}} \approx 0.5\ nm$ gives a free energy of ≈30 *kJ/mol*. Therefore, we do observe an approximately 20 *kJ/mol* hysteresis. A more direct comparison can be made by positioning the sodium ion in the center ($\mathrm{Z^{Na}} \approx 0.0\ nm$) and moving the dimple structure away (from $\mathrm{Z^P} \approx -1.0\ nm$ to $\mathrm{Z^P} \approx -1.8\ nm$), and an extra ≈10 *kJ/mol* free energy cost is need. A possible explanation could be that during the sodium ion insertion and the upper dimple formation process, although the sodium ion provides a strong attraction to the lipid headgroups, the two dimples are under some repulsion state since they are not fully formed. Once the two dimples meet each other, lipids reorient themselves to optimize the curvature of both sides, entering into an attraction

state. Although these two types of states may present similar structures, the intrinsic free energy is different. Unfortunately, the selected coordinates cannot equilibrate such processes within the simulation time scale.

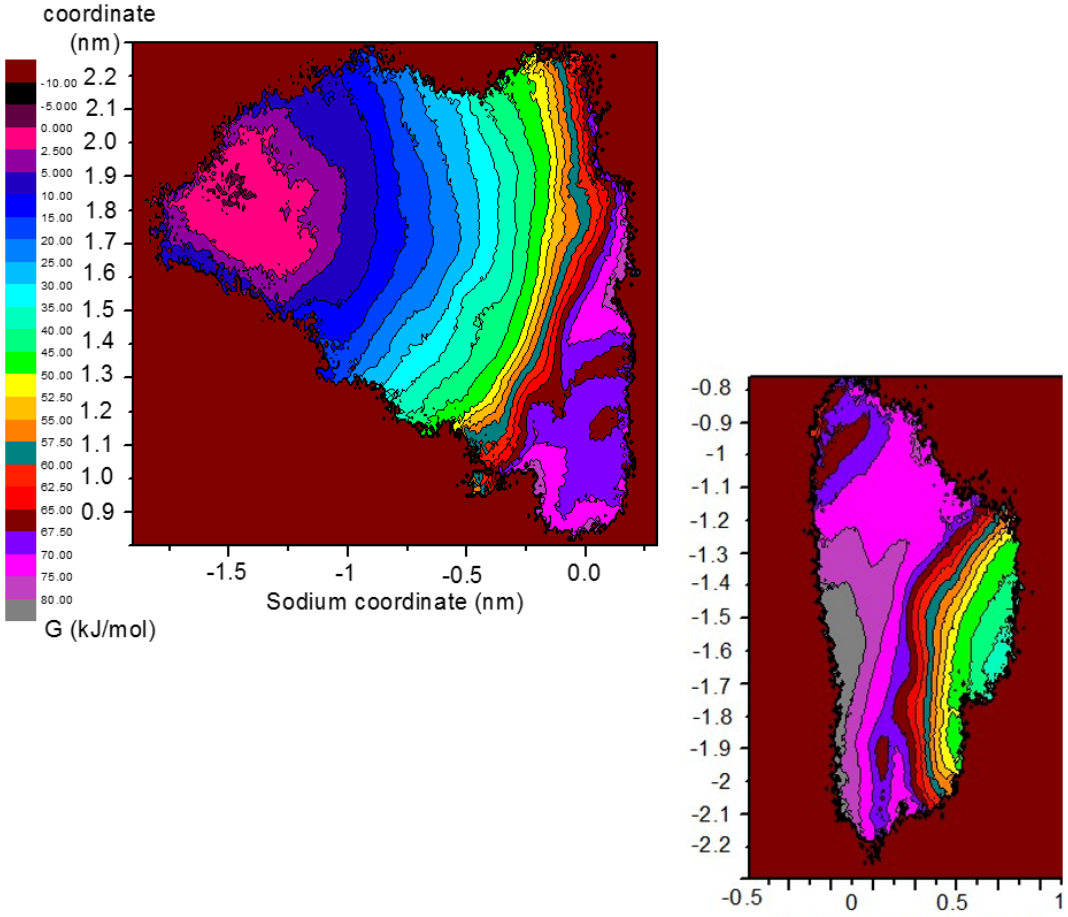

Figure 27. Left: copy of Figure 26. Right: The free energy contour plot of the retreat process of a double dimple structure. (Both the sodium coordinate and the phosphate coordinate have reversed sign, indicating the other side.)

4.4 Conclusions

Both the 1-d and 2-d umbrella sampling data suggests that the free energy cost for the sodium ion to go from the DPPC headgroup region to the lipid center is approximately 60 *kJ/mol*. With the sodium ion at around the bilayer center, the formation of a double-dimple structure from a one-dimple structure costs approximately 10 *kJ/mol* of free energy. Its reverse process also costs approximately 10 *kJ/mol* of free energy, indicating a 20 *kJ/mol* of hysteresis. Such a hysteresis is most likely to be originated from the different attraction states between the dimple structures. Considering the symmetry, the double dimple structure is still likely to be the transition structure which should yield a reversible path. A much longer simulation of the double-dimple structure may yield better statistics when the sodium ion can "jump" between the two dimples several times. Also, another type of simulation could be performed in the future to provide another evidence for the transition structure. After forming a double-dimple structure, a long simulation could be performed with a strong restraint of the sodium ion in $\mathrm{Z}^{\mathrm{Na}} = 0\ nm$ and a lateral position restraint of both dimples. After which, a series of configurations extracted from the trajectory could be chosen to represent the transition structure. Finally, after removing the strong restraint of the sodium ion and slowly increasing the distance between the two dimples, the ion may bind to either side of the bilayer and therefore, provide an estimated probability.

Chapter 5

The pore closure dynamics of lipid membranes

This chapter is an extension study of Chapter 3. In chapter 3, the free energy barrier of a specially designed large permeant across the membrane was studied. And in **section 3.5.5**, the time for the permeant leaving the bilayer was also shown. In this chapter, we create a permeant-free condition for the pore, and focus on the dynamics of pore closure. Similarly, the study is carried out by developing a theory that can simultaneously explain the results of a uniform fluid and an enclosed fluid surrounded by gel.

5.1 Backgrounds

The transient pores can be generated using the laser ablation technique.[105] When a pore is introduced, lipids near the edge undergo structure reorientation to minimize the exposure of their hydrophobic chains to the aqueous environment, forming a cylindrical rim.[106] Such a structural change will lead to an excess in free energy. This free energy cost per unit length is the thermodynamic definition of line tension: $\tau = -\frac{\partial F}{\partial l}$. Line tension, a fundamental mechanical property of cell membranes, is essentially a weak force that is working against the surface tension to enable pore-closing. In simulations, a ribbon-like membrane can be used to estimate the line tension using the pressure tensor.[8] Consider a ribbon membrane in which its surface

normal is along z direction, and the membrane-water interface is along y direction, the line tension can be calculated as:[8]

$$\Lambda = \frac{1}{2}\langle L_x L_z [\frac{1}{2}(P_{xx} + P_{zz}) - P_{yy}]\rangle \quad (68)$$

Where L_x and L_z are the box dimensions of x and z direction, and P_{xx}, P_{yy} and P_{zz} are the diagonal elements of the pressure tensor.

The significance of transient pores together with its edge tension has been studied experimentally using model systems such as vesicles. The outer stress that could lead to the pore formation includes temperature, surface tension and electrochemical gradient.[107-110] Usually, these experiments provide estimates in pore size as well as its change with time. For example, Srividya and Muralidharan[105] used laser ablation technique to generate transient pores (with diameters around 1 μm) on giant vesicles (with diameters around 20 μm) and determined its closing time is in the range of several seconds to a few minutes, depending on the type of lipids. Laser ablation is a process of that involves using strong laser beams to remove materials from a solid or liquid surfaces. By absorbing strong heat, the local material will evaporate. Although the vesicle got relaxed on room temperature, it is extremely difficult to measure or even estimate the local temperature due to the ablation. Since a portion of lipids has been removed, lipids may rearrange themselves to achieve optimal packing, causing the size of the vesicle to be smaller, and introducing flux through the pore. Srividya and Muralidharan[105] focused on the quasi-static leakout limit,[111] upon which the

leakage of the inner fluid is very slow, and the size of vesicles can be treated constant. The theory they used to predict the pore size change with time is discussed by Brochard-Wyart[111] and Rodriguez.[112] The change of the radius of the pore (r_{pore}) is a competition effect between the line tension τ and the surface tension σ.

$$\frac{dr_{pore}}{dt} = \frac{r_{pore}(t)}{2\eta}\left[\sigma(t) - \frac{\tau}{r_{pore}(t)}\right] \tag{69}$$

where η is the surface viscosity of the lipid membrane. By treating the radius of the vesicle (R) as constant, the surface tension is also constant. The line tension can be estimated using the following equation:[105]

$$R^2\, ln\left(r_{pore}\right) \approx -\frac{2\tau}{3\pi\eta_w} t \tag{70}$$

where η_w is the bulk viscosity of water. However, unlike DLPC, DPPC, DOPC and Egg-PC, whose $R^2 ln(r_{pore})$ can be fitted into a straight line, DSPC presents an anomaly on this quantity.[105] The pore closure for DSPC is significantly slower and presents two distinct stages. Srividya attributes this anomaly to the different behavior in shear viscosity, which is time-dependent for DSPC.[105] Among these lipids, DSPC and DPPC are in the gel state at room temperature, which nominally is the conditions at the experiments, and DSPC has a phase transition temperature that is even higher than DPPC. Therefore, a possible explanation could be that the ablation triggers some partial melting and brings the system temperature to be above T_m, and the subsequent refreezing processes affects the dynamics at some points.

To elucidate the dynamics of pore-closure under the phase-coexisting condition, we

simplify the model by choosing a planar lipid bilayer, represented using represented using the coarse-grained MARTINI 2.0 forcefield.[53, 72] The phase transition temperature (T_m) of this forcefield is determined as between 302 and 303K by performing stripe domain melting kinetics simulations.[46] Two types of initial configurations were equilibrated at T_m, a uniform fluid bilayer and an enclosed fluid domain surrounded by gel. After removing the lipids whose center of mass are located within a circle of radius 3.5 *nm*, the remaining lipids were strongly restrained to allow water molecules filling in the hole. The starting time is set when the strong restraint is removed from an equilibrated structure (when the water fully occupies the hole). In the beginning, lipids near the edge will quickly reorient themselves to form a pore. The pore radius is calculated by scaling the total water number inside the pore with respect to that of time zero.

For the enclosed fluid domain surrounded by gel, the line tension of the fluid-gel interface is working against the pore closure. This is due to the increase in the interfacial lengths, since a portion of gel lipids will melt to join the adjacent fluid domain to compensate the excess area of the pore. Also, the melting process will also down the dynamics of pore-closing, compared to the uniform fluid. We aimed at developing a theory that could give a quantitative prediction for these processes.

5.2 Simulation methods

5.2.1 system construction

A DPPC bilayer as represented by the coarse-grained MARTINI[53, 72] forcefield was used to study the dynamics of pore closure. Molecular dynamics simulations, including those under position restraints, were performed using Gromacs[64] version 4. The system's temperature was control at 302 K (the tested apparent T_m for this forcefield) by the velocity rescaling[55] method, with a time constant of 1.0 ps. The pressure was maintained at 1 bar using the Berendsen pressure coupling method, with a time constant of 2.5 ps. The uniform fluid and enclosed fluid systems employed semi-isotropic pressure coupling with a compressibility of 5×10^{-5} bar^{-1} in both z and x-y directions. The constant area simulations were carried out by setting the compressibility in x-y direction to be 0. The Lennard-Jones cut-off was 1.2 nm, with the switch function started to apply at 0.9 nm. The time step used for this study was 25 fs.

5.2.2 Pore generation and pore radius estimation

A cylinder pore with a 3.5 nm radius was generated from a fully equilibrated lipid membrane by removing lipids whose center of mass is laterally located within a 3.5 nm radius with respect to the membrane center. After that, each lipid atom was applied a strong position restraint in both x and y directions, with a force constant of 2000 $kJ{\cdot}mol^{-1}{\cdot}nm^{-2}$. The system was then equilibrated under the constant area condition until the water molecules fully filled the cylinder pore. By choosing a series of starting configurations from those equilibrated structures, and by removing all the

position restraints of lipid atoms and setting t=0, the pore closure can be studied as a function of time. To estimate the pore radius at a certain time (r_t), the total number of water molecules inside the pore (N_t) is used to scale with respect to that at t=0 (N_0).

$$r_t = 3.5nm \times \sqrt{\frac{N_t}{N_0}} \tag{71}$$

The upper or lower boundary of the pore was defined as the average Z position of C_1A and C_1B of the upper or lower layer of lipids that is laterally within a 5 *nm* radius to the center. Any water molecule whose center of mass is within these boundaries was counted. Usually, N_0 lies in the range of 2500-2800.

5.2.3 The size-dependent study

A system that contains 2048 DPPC molecules and 64000 water molecules was chosen as the smallest size one (before the pore generation). Other systems were made twice as bigger, 4 times bigger, 9 times bigger and 16 times bigger, by extending periodic configurations in the x-y plane. The temperature of these systems was set to 300 K. Two type of ensembles were used to compare the difference, NPT and NP_zAT (constant area). The pore generation and pore radius estimation have already been described previously. The end time is defined as when the number of water molecules inside the pore is consistently below 20.

5.2.4 Other simulation details

The way to quantify the phase composition and its corresponding area per lipid, and the method to determine the phase transition temperature of the system have already been described in **Chapter 3**, **section 3.2.2** and **section 3.2.3**.

5.3 Results

5.3.1 The size-dependent study

The pore closing time under the different system size is listed in Table 7. For the NP_zAT ensemble, the closing time is significantly larger for the smallest system, but comparable for the rest of the systems. For the smaller system, the area per lipid of the membrane must expand more to compensate for the excess area of the pore. Such a process will build up surface tension, and slow down the pore closure. Since the system size beyond 34.98 × 34.98 nm^2 gives similar pore closing time, it can be concluded that this size is large enough that the area change is small enough when the pore closes, so that surface tension is approximately zero. For the NPT ensemble, all sizes of systems have similar closing time.

Box dimensions (nm^3)	Closing time (ns) → NP_zAT	Closing time (ns) → NPT
25.34 × 25.34 × 7.05	120 ± 50	8.7 ± 0.7
34.98 × 34.98 × 7.20	10.9 ±1.7	9.2 ± 0.6
50.68 × 50.68 × 7.24	10.8 ± 1.5	9.6 ± 0.2
76.03 × 76.03 × 7.25	10.3 ± 1.3	11.6 ± 1.0
101.37 × 101.37 × 7.26	10.2 ± 0.5	12.4 ± 0.6

Table 7. The pore closing time under different system sizes (for NP_zAT ensemble and NPT ensemble). The average size of the initial configuration at t=0 is listed. The temperature of the system is 300 *K*, 2°C below the T_m.

5.3.2 The pore closure of a uniform fluid bilayer

The result of the pore closure of a uniform fluid bilayer at T_m is shown in Figure 28 (a). In the first 1*ns*, the pore radius for both sets of data undergoes a sharp drop, transitioning to a smoother decrease. This is due to the fast rearrangement of lipids that is near the edge of the interface, which will minimize the exposure of their hydrophobic chains to the aqueous environment. After 1 *ns*, the pore with a shape of cylindrical rim is formed, as is indicated in the snapshot of Figure 29. As the line tension works its way to close the pore, the time it takes for the pore radius of the NPT ensemble to reach 0.5 *nm* is 5.5 *ns*, while that of the constant area ensemble is 6.6 *ns*. The pore closure for the NP_zAT ensemble is somewhat slower, although the system size has already reached the limit to ignore surface tension effect. An interesting observation is that the pore radius of both ensembles follows a trend of a linear decrease (although from the data, the linear decrease is just an approximation, we are fitting it to a line at this point for the purpose of this study) after the first 1*ns*. In Figure 28 (b), the radius data after the pore is fully formed is chosen to perform a linear fit. The slope for the NPT ensemble is -0.502 ± 0.008 *nm/ns*, while the slope for the NP_zAT ensemble is -0.419 ± 0.007 *nm/ns*. In the later discussion, we will relate this slope to the edge tension and the viscosity of the lipid membrane.

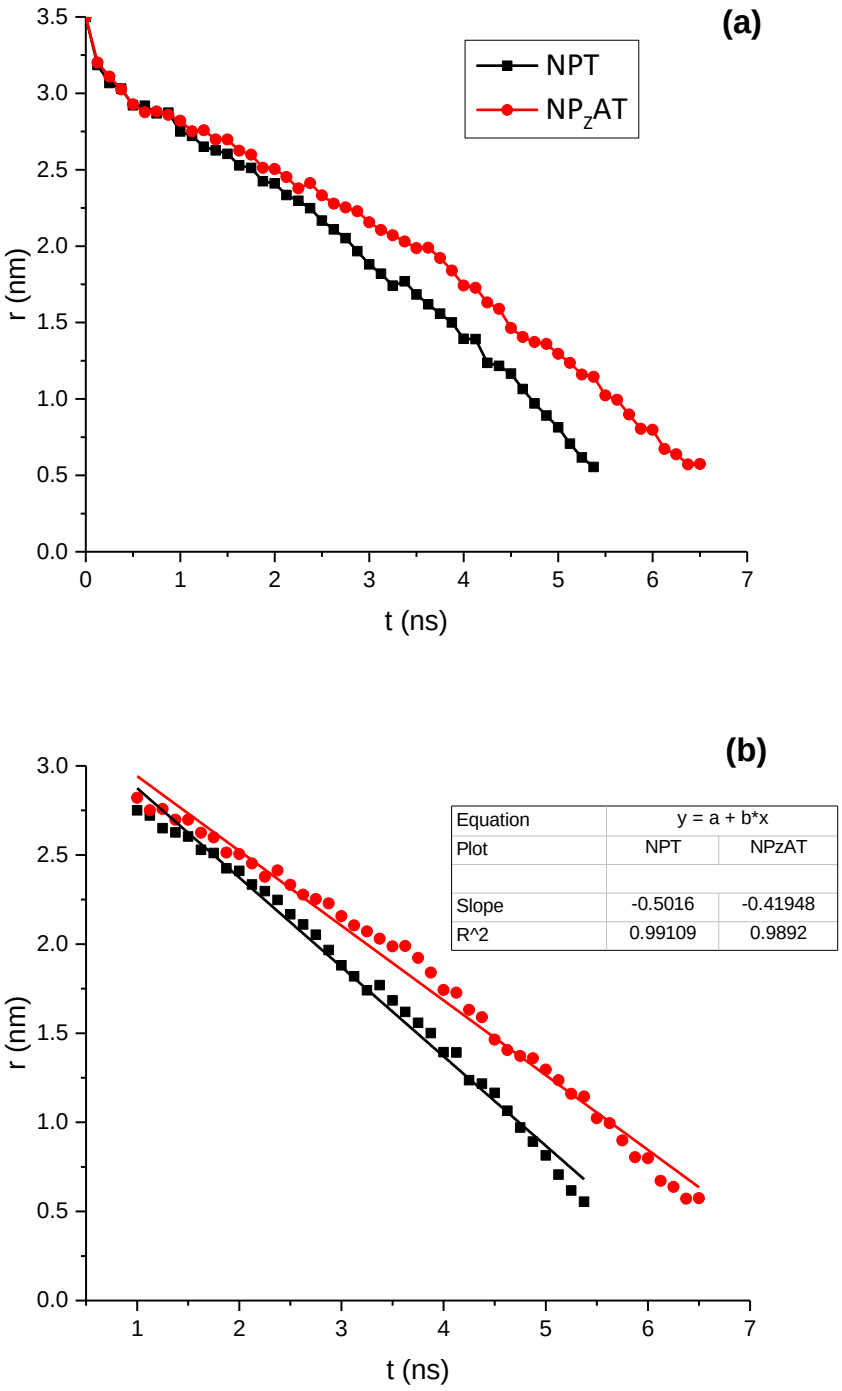

Figure 28. **a)** The pore radius of a uniform fluid vs. time using the NPT ensemble and NP$_z$AT ensemble. (Each set of data is averaged over 6 trials.) **b)** The linear fit of each data set (with portions of data after t=1 *ns*).

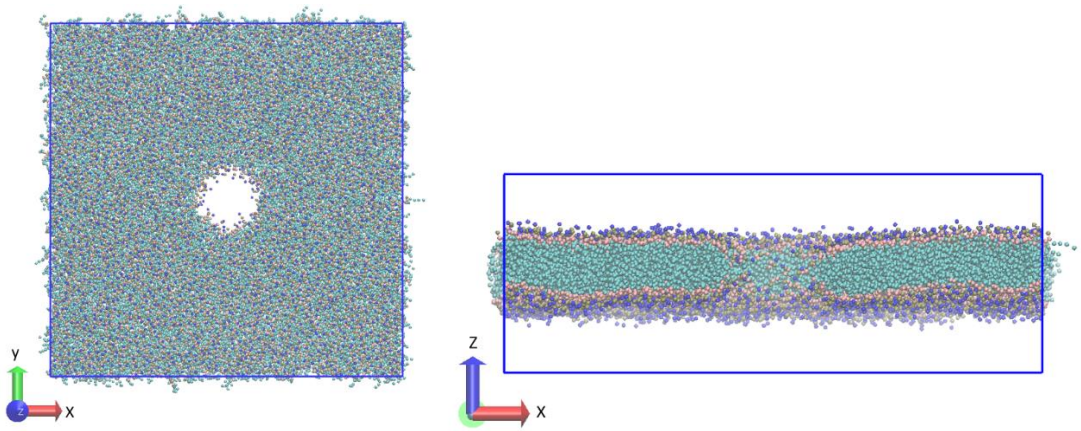

Figure 29. The top and the front cut view (lipid atoms with y>15.5nm are shown) of a DPPC bilayer that consists of 3962 lipid molecules and 320000 water molecules. This configuration is chosen from a trial of an NPT ensemble simulation at t = 1*ns*.

5.3.3 The pore closure of an enclosed fluid bilayer surrounded by gel

For an enclosed fluid bilayer surrounded by gel (set at T_m), the pore closure is a competing effect between the edge tension and the line tension between the gel domain and fluid domain. As the edge tension tries to close the pore, a portion of gel phase lipids near the interface will join its adjacent fluid phase, compensating for the area decrease. This effect will expand the fluid-gel boundary lengths, which is a process that will be resisted by the line tension of the gel-fluid interface. A snapshot representation is shown in Figure 30. The pore closure dynamics of the enclosed fluid is shown in Figure 31. The sharp decrease of the pore radius in the beginning stage is also captured, as the same as the uniform fluid. However, unlike the uniform fluid, the decrease rate of both ensembles is approximately the same in the subsequent time scale. This is because the bulk gel is rigid, and the box dimension of the NPT

ensemble is nearly unchanged. Therefore, the number of lipids that undergoes phase shift to compensate the same excess area is approximately the same. The time for the pore to shrink to a radius of 0.5 *nm* is approximately 12 *ns*, distinctly longer than that of the uniform fluid. Another interesting feature to note is that the decrease rate of the radius shows a somewhat increase as the pore gets smaller. This trend is less distinct for the uniform fluid, where an approximation of linear fit is applied.

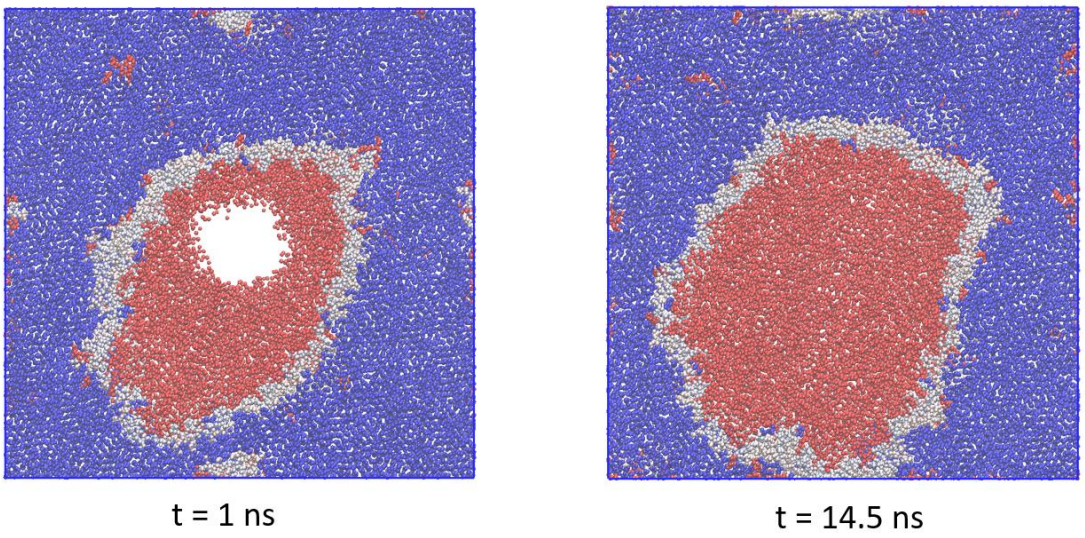

Figure 30. The top view of (Left): a pore formed after removing the position restraint for 1ns. (Right): The pore has closed with a growing area in the fluid domain. (Red: fluid phase; blue: gel phase; light blue or light pink: interface)

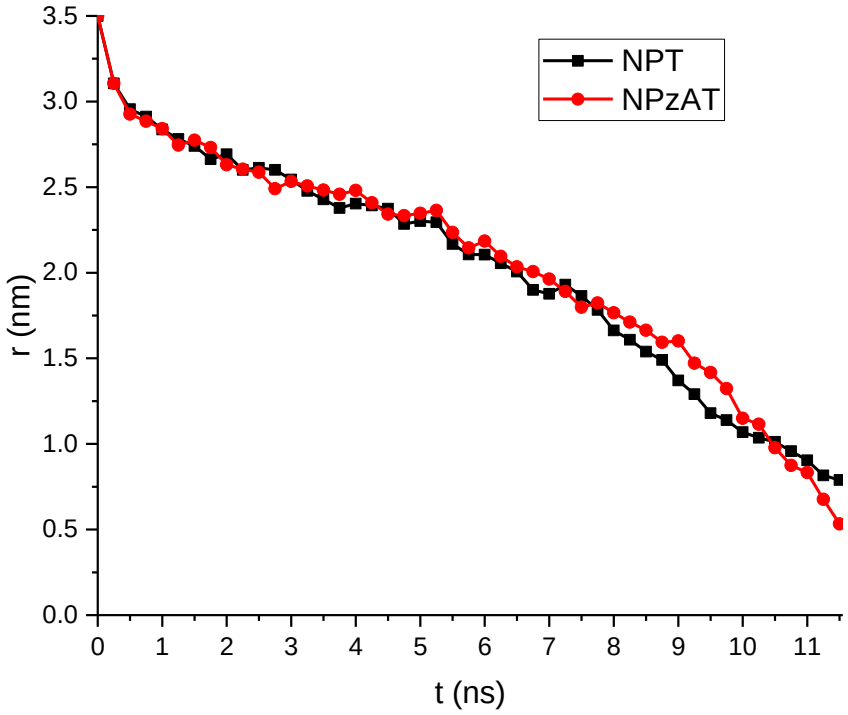

Figure 31. The pore radius of an enclosed fluid surrounded by gel vs. time using the NPT ensemble and NP_ZAT ensemble. (Each set of data is averaged over 6 trials.)

5.4 Discussion

5.4.1 Understanding the pore closure of uniform fluid systems

Consider a uniform fluid membrane (with a total area of A_{tot}) with a pore (the pore radius is denoted as r) located in the center, the free energy of the system can be written as:

$$G = \sigma(A_{tot} - \pi r^2) + \tau \cdot 2\pi r + const. \tag{72}$$

where σ is the surface tension of the system, and τ is the edge tension. The time derivative of the radius r satisfies the following equation:[113]

$$-\frac{\partial G}{\partial L} = 2\eta d \cdot \frac{dr}{dt} \tag{73}$$

where L is the perimeter of the pore, η is the surface viscosity of the lipid membrane, and d is membrane thickness. Equation (73) can be rewritten as:

$$-\frac{1}{2\pi} \cdot \frac{\partial G}{\partial r} = 2\eta d \cdot \frac{dr}{dt} \tag{74}$$

By substituting equation (72) into equation (74), the dynamics is expressed as:

$$2\eta d \cdot \dot{r} = \sigma r - \tau \tag{75}$$

Assuming that the system size is large enough that the area per lipid change is small enough when the pore closes, the surface tension is approximately zero. Then, equation (9) can be integrated to a simple expression as:

$$r = r_0 - \frac{\tau}{2\eta d} t \tag{76}$$

where r_0 is the initial pore radius. This equation provides an explanation to why the pore radius mostly follows a linear decrease with time for the uniform fluid. The slope equals to $-\frac{\tau}{2\eta d}$. A separate calculation using equation (68) estimates the edge tension τ to be 50 *pN*. Therefore, the denominator can be calculated and be used as a reference to compare with the values from the enclosed fluid domain surrounded by gel.

5.4.2 Understanding the pore closure of enclosed fluid systems

Consider a circular fluid domain (with radius R) that is enclosed by gel with a pore (radius r) located in the center (see Figure 32), the free energy of the system can be written as:

$$G = \sigma(\pi R^2 - \pi r^2) + \tau \cdot 2\pi r + \Lambda \cdot 2\pi R + const. \tag{77}$$

where σ is the surface tension of the system, τ is the edge tension and Λ is the line tension between the gel domain and fluid domain. If also assuming $\sigma = 0$ under the large system size limit, the free energy driving force has the form of:

$$-\frac{\partial G}{\partial L} = -\frac{\partial(\tau \cdot 2\pi r + \Lambda \cdot 2\pi R)}{\partial(2\pi r)} = -\tau - \Lambda\frac{\partial R}{\partial r} \tag{78}$$

The first term is a result of the edge tension, same to that of the uniform fluid. The second part comes from the line tension between the gel and fluid domains. Since the increase in the outer radius will result in a decrease of the pore radius, the second term will have an opposite effect towards closing the pore. Since the pore closing will facilitate gel to fluid phase transition, another resistance in terms of melting is also added. The pore radius change with time satisfies the following equation:

$$-\tau - \Lambda\frac{\partial R}{\partial r} = 2\eta d \cdot \frac{\partial r}{\partial t} - \gamma_m \cdot R \cdot \frac{\partial R}{\partial t} \tag{79}$$

where τ is the edge tension, Λ is the line tension between the gel and fluid domains, and γ_m is a melting rate constant of the gel to fluid phase transition. Here, the melting resistance has an additional radius term compared with that of the surface viscosity expression. This is because the melting is accompanied by an increase in the area per lipid. Since the gel phase is nearly incompressible, the additional sheer stress introduced by the increase in area per lipid needs to be relaxed through the fluid phase. During the stress relaxation time, the radius is increased again and this process iterates. As derived by Debregeas and Brochard-Wyart,[113] this effect is considered that the additional increase in the radius is proportional to the radius itself. Details of the melting rate constant derivation will be discussed in the subsequent section.

The area conservation of the system can be written in terms of the following two equations:

$$A_{tot} = \frac{1}{2} N_f a_f^{\ominus} + \frac{1}{2}\left(N_{tot} - N_f\right) a_g^{\ominus} + \pi r^2 \tag{80}$$

$$\pi R^2 = \frac{1}{2} N_f a_f^{\ominus} + \pi r^2 \tag{81}$$

where N_{tot} denotes the total number of lipids in the system which equals the summation of the number of fluid phase lipids N_f and the number of gel phase lipids, $a_f^{\ominus}$ and $a_g^{\ominus}$ are the standard area per lipid of the fluid and gel phase, respectively. Solving equation (80) and (81), the outer radius is expressed in terms of r.

$$R = \sqrt{-\frac{a_g^{\ominus}}{a_f^{\ominus} - a_g^{\ominus}} r^2 + \frac{2A_{tot} - N_{tot} a_g^{\ominus}}{a_f^{\ominus} - a_g^{\ominus}} \cdot \frac{a_f^{\ominus}}{2\pi}} \tag{82}$$

Here, we define $M_g = \frac{a_g^{\ominus}}{a_f^{\ominus} - a_g^{\ominus}}$ as the gel phase multiplier, and $A_{const} = \frac{2A_{tot} - N_{tot} a_g^{\ominus}}{a_f^{\ominus} - a_g^{\ominus}} \cdot \frac{a_f^{\ominus}}{2\pi}$ as an area constant, equation (13) can be simplified as:

$$R = \sqrt{-M_g r^2 + A_{const}} \tag{83}$$

The M_g is essentially a count of how many gel phase molecules are needed to transfer to fluid phase in order to compensate the area of a single gel phase lipid. Interesting to note is that $A_{const} - M_g \cdot r^2$ needs to be greater than zero. Since A_{const} is an area constant that is proportional to the membrane total area, the requirement is that the system has to be large enough to accommodate the pore size.

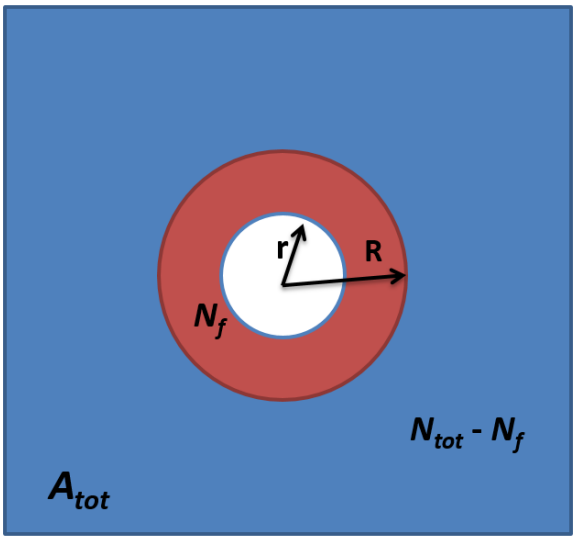

Figure 32. The cartoon representation of the area conservation of an enclosed fluid domain surrounded by gel.

Substituting equation (83) into equation (79) by rewriting $\frac{\partial R}{\partial t} = \frac{\partial R}{\partial r} \cdot \frac{\partial r}{\partial t}$, the whole expression can be written in terms of the pore radius:

$$-\tau - \Lambda \frac{-M_g \cdot r}{\sqrt{A_{const} - M_g \cdot r^2}} = 2\eta d \cdot \frac{\partial r}{\partial t} - \gamma_{melt} \sqrt{A_{const} - M_g \cdot r^2} \cdot \frac{-M_g \cdot r}{\sqrt{A_{const} - M_g \cdot r^2}} \cdot \frac{\partial r}{\partial t} \quad (84)$$

Through rearrangement of equation (84), the pore radius change has the form of:

$$\dot{r} = \frac{\partial r}{\partial t} = \frac{-\tau + \Lambda \frac{M_g \cdot r}{\sqrt{A_{const} - M_g \cdot r^2}}}{2\eta d + \gamma_{melt} \cdot M_g \cdot r} \quad (85)$$

The numerator is composed of two parts, a term from the edge tension, positively facilitating the pore closure, and a term originated from the line tension between the

gel and fluid domains, impeding the pore closure. In the denominator, the melting resistance effect is added to the viscosity term.

5.4.3 Calculating the melting rate constant

The melting rate constant γ_{melt} can be estimated from a bilayer system formed from alternating gel and fluid stripes. In a stripe system, suppose the width of the gel phase is *w*, and it is centered at *x*=0, then the position of the right-hand side interface is *x*/2. The definition of γ_{melt} is:

$$\gamma_{melt} \cdot dx/dt = -\frac{1}{L_y} \cdot dF/dx \tag{86}$$

where L_y is the box length of the y direction. The physical meaning is that the free-energy driving force exerted in the interface $-dF/dx$ per unit length equals the melting rate constant times the velocity of the moving interface.

The gel phase width change with time is written as:

$$\frac{d\omega}{dt} = \frac{d}{dt}\left(\frac{A_g}{L_y}\right) = \frac{d}{dt}\left(\frac{f_g N_{tot} a_g^{\ominus}}{L_y}\right) = \frac{N_{tot} a_g^{\ominus}}{L_y} \cdot \frac{df_g}{dt} \tag{87}$$

where A_g is the total area of gel phase, L_y is the box length of the y direction, and f_g is the fraction of lipids that are in the gel phase. Since the width change is twice as faster than the change of the right-hand side interface, we have:

$$\frac{dx}{dt} = \frac{1}{2} \cdot \frac{N_{tot} a_g^{\ominus}}{L_y} \cdot \frac{df_g}{dt} \tag{88}$$

The total number of the gel phase lipids can be written as the total area of the gel

phase divided by the standard area per lipid of the gel phase:

$$N_g = \frac{L_y x}{a_g^{\ominus}} \Rightarrow \frac{dN_g}{dx} = \frac{L_y}{a_g^{\ominus}} \tag{89}$$

The free energy change with x has the following form:

$$\frac{dF}{dx} = \Delta\mu_{g-f} \cdot \frac{dN_g}{dx} = \Delta\mu_{g-f} \cdot \frac{L_y}{a_g^{\ominus}} \tag{90}$$

where $\Delta\mu_{g-f}$ is the chemical potential to move a lipid from gel phase to fluid phase. After substituting equation (88) and equation (90) into equation (86), the expression of γ_{melt} can be obtained.

$$\gamma_{melt} = \frac{2L_y}{N_{tot}(a_g^{\ominus})^2} \cdot \frac{\Delta\mu_{g-f}}{-df_g/dt} \tag{91}$$

The data of the melting dynamics of stripe systems at various temperatures is shown in Figure 16. **Chapter 3, section 3.3.1** has a detailed discussion on identifying T_m. As the temperature is deviated away from T_m, the rate of the gel fraction change is increased. By approximating the ratio change as linear with respect to time, df_g/dt can be plotted at different temperatures (see Figure 33). For this study where the temperature range is narrow around the T_m, we fit these points to a line instead of the Arrhenius equation. The slope $(df_g/dt)/dT$ = -0.00112$ns^{-1} \cdot T^{-1}$. We use the parameters of the stripe system to estimate γ_{melt} through equation (91). The total number of lipids N_{tot} = 3930; the box length in the y direction L_y = 32.4 *nm*; and the standard area per lipid of the gel phase $a_g^{\ominus} = 0.4683nm^2$. At ΔT = 1*K*, $\Delta\mu_{g-f} = 0.085\ kJ/mol$, and df_g/dt = -0.00112ns^{-1}. Using all these numbers, $\gamma_{melt} = 9.47pN \cdot ns/nm^2$.

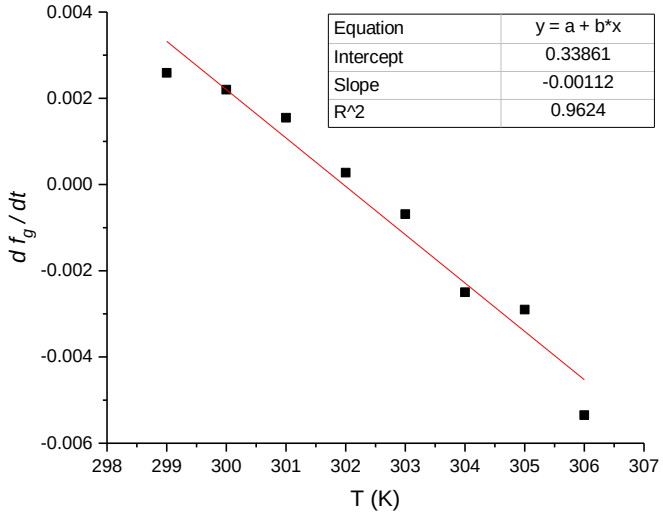

Figure 33. The change of the fractional ratio of gel phase with time at different temperatures.

5.4.4 Self-consistent check

From the uniform fluid simulations, we know that: $-\frac{\tau}{2\eta d} = -0.419\, nm/ns$ (NP_zAT ensemble). Since $\tau = 50pN$, $2\eta d = 119\, pN \cdot ns/nm$. From an area per lipid estimation (using the same method described at **Chapter 3, section 3.2.2**), $M_g = 4.367$, $A_{const} = 136.6nm^2$. Substituting all these numbers into equation (85), the predicted pore radius change can be plotted. The fitting result is shown in Figure 34. The prediction is successful in both the pore closing time, and the noticeable acceleration when the pore gets smaller. The closing time for the enclosed fluid is approximately twice as much as that for the uniform fluid. It can be inferred from equation (85), when r gets very close to 0, the closing rate will reach the same to that of the uniform fluid.

$$\lim_{r\to 0}\left(\frac{-\tau+\Lambda\frac{M_g\cdot r}{\sqrt{A_{const}-M_g\cdot r^2}}}{2\eta d+\gamma_{melt}\cdot M_g\cdot r}\right)=\frac{-\tau}{2\eta d} \tag{92}$$

To study how the pore closure rate is influenced by the melting, another prediction is provided when the melting term is set to 0, as shown in figure 34 (pink curve). The dynamics predicted almost matches that of the uniform fluid system under the NP_zAT ensemble, instead of the enclosed fluid system. We will seek evidence why this is the case from equation (85). Using the initial radius r = 2.81 *nm* at t = 1 *ns*, the second term in the numerator of equation (85) is approximately 12 *pN*, which is comparatively small to the edge tension contribution -50 *pN*. As discussed above, the contribution from the fluid-gel interfacial tension will continue to be smaller as the radius shrinks. Therefore, it is understandable that the interfacial tension will not introduce a distinct bias to the pore closure dynamics.

Finally, we acknowledge that fitting the dynamics of a uniform fluid to a straight line is an approximation. For the uniform fluid, although the acceleration of pore closure is not obvious, it is certainly noticeable. A possible explanation is that the local surface tension around the pore might not be exactly zero. If we assume it to be a very small constant, equation (75) can be integrated into the following form:

$$r=\frac{\tau}{\sigma}+\left(r_0-\frac{\tau}{\sigma}\right)\cdot e^{\frac{\sigma}{2\eta d}t} \tag{93}$$

where an exponential decay is predicted for r. Another possible source of

non-linearity is in how the radius is defined; as the curvature of the interface increases, the apparent radius becomes more sensitive to the precise definition. A different definition might eliminate the non-linearity in the pore closure dynamics.

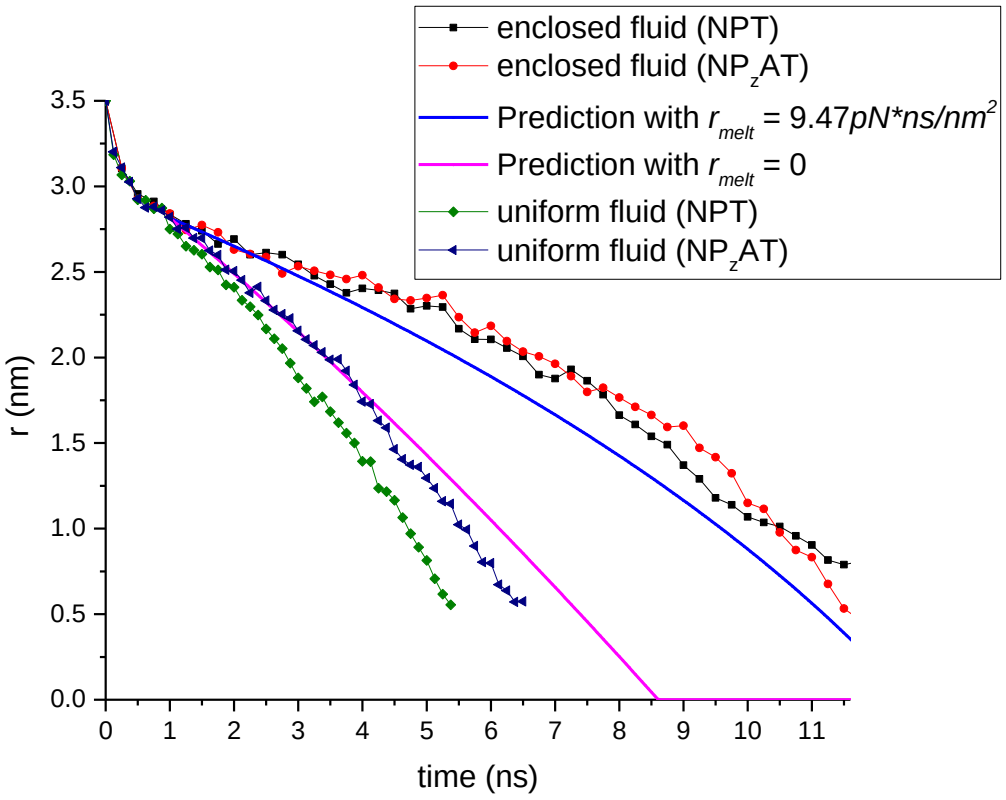

Figure 34. The predicted pore radius of an enclosed fluid surrounded by gel vs. time (blue curve). The fitting starts from t = 1 *ns*. The prediction without a melting term is also provided as the pink curve. The simulated data of both the enclosed fluid and uniform fluid at different ensembles is also shown.

5.5 Conclusion

At T_m, the pore closure dynamics of an enclosed fluid domain is strongly influenced

by the surrounding bulk gel, compared to that of the uniform fluid. Under the large system limit, the radius of the pore shows a linear decrease with time. For the enclosed fluid domain, since its size has been limited by the bulk gel, the pore closure needs to facilitate gel to fluid phase transition near the interface, to compensate for the area of the pore. The influence is composed of two parts. One is the resistance from the line tension between the gel and fluid domains, since the interfacial lengths are increased with the accompanying increase in fluid domain size. The other is the melting from the gel to fluid state, which is a time-dependent process. A stripe system with alternating gel and fluid domains has been used to estimate the melting rate constant. By using the surface viscosity of the membrane derived from the uniform fluid, and by substituting the melting rate constant, our theory fits well with the simulation results. According to the model, the dynamics of the conversion of gel to fluid plays a more important role in slowing down the pore closure than does the increase in interfacial energy due to gel-fluid line tension.

References

1. Subramaniam, S.; Fahy, E.; Gupta, S.; Sud, M.; Byrnes, R. W.; Cotter, D.; Dinasarapu, A. R.; Maurya, M. R., Bioinformatics and Systems Biology of the Lipidome. *Chem Rev* **2011**, *111*, 6452-6490.

2. Fahy, E.; Subramaniam, S.; Murphy, R. C.; Nishijima, M.; Raetz, C. R. H.; Shimizu, T.; Spener, F.; van Meer, G.; Wakelam, M. J. O.; Dennis, E. A., Update of the Lipid Maps Comprehensive Classification System for Lipids. *J Lipid Res* **2009**, *50*, S9-S14.

3. Wiggins, P. M., Role of Water in Some Biological Processes. *Microbiol Rev* **1990**, *54*, 432-449.

4. Blanazs, A.; Armes, S. P.; Ryan, A. J., Self-Assembled Block Copolymer Aggregates: From Micelles to Vesicles and Their Biological Applications. *Macromol Rapid Comm* **2009**, *30*, 267-277.

5. Yang, L.; Kindt, J. T., Simulation Study of the Permeability of a Model Lipid Membrane at the Fluid–Solid Phase Transition. *Langmuir* **2015**, *31*, 2187-2195.

6. Tieleman, D. P.; Marrink, S. J., Lipids out of Equilibrium: Energetics of Desorption and Pore Mediated Flip-Flop. *J Am Chem Soc* **2006**, *128*, 12462-12467.

7. Tristram-Nagle, S.; Nagle, J. F., Lipid Bilayers: Thermodynamics, Structure, Fluctuations, and Interactions. *Chem Phys Lipids* **2004**, *127*, 3-14.

8. Jiang, F. Y.; Bouret, Y.; Kindt, J. T., Molecular Dynamics Simulations of the Lipid Bilayer Edge. *Biophys J* **2004**, *87*, 182-192.

9. Cheng, C. Y.; Goor, O. J.; Han, S., Quantitative Analysis of Molecular Transport across Liposomal Bilayer by J-Mediated 13c Overhauser Dynamic Nuclear Polarization. *Anal Chem* **2012**, *84*, 8936-40.

10. Ramahaleo, T.; Morillon, R.; Alexandre, J.; Lassalles, J. P., Osmotic Water Permeability of Isolated Protoplasts. Modifications During Development. *Plant Physiol* **1999**, *119*, 885-96.

11. Jaber, A. M.; Moody, G. J.; Thomas, J. D.; Willcox, A., Radiotracer Studies on Ion-Selective Membranes Based on Poly(Vinyl Chloride) Matrices. *Talanta* **1977**, *24*, 655-7.

12. Carruthers, A.; Melchior, D. L., Studies of the Relationship between Bilayer Water Permeability and Bilayer Physical State. *Biochemistry-Us* **1983**, *22*, 5797-5807.

13. Andrasko, J.; Forsen, S., Nmr-Study of Rapid Water Diffusion across Lipid Bilayers in Dipalmitoyl Lecithin Vesicles. *Biochem Bioph Res Co* **1974**, *60*, 813-819.

14. Finkelst.A; Cass, A., Permeability and Electrical Properties of Thin Lipid Membranes. *J Gen Physiol* **1968**, *52*, S145-&.

15. Huang, C.; Thompson, T. E., Properties of Lipid Bilayer Membranes Separating 2 Aqueous Phases - Water Permeability. *J Mol Biol* **1966**, *15*, 539-&.

16. Fettiplace, R., Influence of Lipid on Water Permeability of Artificial Membranes. *Biochim Biophys Acta* **1978**, *513*, 1-10.

17. Hanai, T.; Haydon, D. A., Permeability to Water of Bimolicular Lipid Membranes. *J Theor Biol* **1966**, *11*, 370-&.

18. Trauble, H., Movement of Molecules across Lipid Membranes - Molecular Theory. *J Membrane Biol* **1971**, *4*, 193-&.

19. Marrink, S. J.; Berendsen, H. J. C., Simulation of Water Transport through a Lipid-Membrane. *J Phys Chem-Us* **1994**, *98*, 4155-4168.

20. Gupta, R.; Sridhar, D. B.; Rai, B., Molecular Dynamics Simulation Study of Permeation of Molecules through Skin Lipid Bilayer. *The Journal of Physical Chemistry B* **2016**, *120*, 8987-8996.

21. Kuczera, K.; Jas, G. S.; Elber, R., Kinetics of Helix Unfolding: Molecular Dynamics Simulations with Milestoning. *J Phys Chem A* **2009**, *113*, 7461-7473.

22. Vanden-Eijnden, E.; Venturoli, M.; Ciccotti, G.; Elber, R., On the Assumptions Underlying Milestoning. *J Chem Phys* **2008**, *129*.

23. Elber, R., A Milestoning Study of the Kinetics of an Allosteric Transition: Atomically Detailed Simulations of Deoxy Scapharca Hemoglobin. *Biophys J* **2007**, *92*, L85-L87.

24. West, A. M. A.; Elber, R.; Shalloway, D., Extending Molecular Dynamics Time Scales with Milestoning: Example of Complex Kinetics in a Solvated Peptide. *J Chem Phys* **2007**, *126*.

25. Faradjian, A. K.; Elber, R., Computing Time Scales from Reaction Coordinates by Milestoning. *J Chem Phys* **2004**, *120*, 10880-10889.

26. Cardenas, A. E.; Jas, G. S.; DeLeon, K. Y.; Hegefeld, W. A.; Kuczera, K.; Elber, R., Unassisted Transport of N-Acetyl-L-Tryptophanamide through Membrane: Experiment and Simulation of Kinetics. *J Phys Chem B* **2012**, *116*, 2739-2750.

27. Allen, T. M.; Cullis, P. R., Liposomal Drug Delivery Systems: From Concept to Clinical Applications. *Adv Drug Deliver Rev* **2013**, *65*, 36-48.

28. Blum, R. H.; Carter, S. K., Adriamycin - New Anticancer Drug with Significant Clinical Activity. *Ann Intern Med* **1974**, *80*, 249-259.

29. Chang, H. I.; Yeh, M. K., Clinical Development of Liposome-Based Drugs: Formulation, Characterization, and Therapeutic Efficacy. *Int J Nanomed* **2012**, *7*, 49-60.

30. Mills, J. K.; Needham, D., Lysolipid Incorporation in Dipalmitoylphosphatidylcholine Bilayer Membranes Enhances the Ion Permeability and Drug Release Rates at the Membrane Phase Transition. *Bba-Biomembranes* **2005**, *1716*, 77-96.

31. Yacoub, T. J.; Reddy, A. S.; Szleifer, I., Structural Effects and Translocation of Doxorubicin in a Dppc/Chol Bilayer: The Role of Cholesterol. *Biophys J* **2011**, *101*, 378-385.

32. Demel, R. A.; Dekruyff, B., Function of Sterols in Membranes. *Biochim Biophys Acta* **1976**, *457*,

109-132.

33. Chowdhry, B. Z.; Lipka, G.; Dalziel, A. W.; Sturtevant, J. M., Multicomponent Phase-Transitions of Diacylphosphatidylethanolamine Dispersions. *Biophys J* **1984**, *45*, 901-904.

34. Papahadjopoulos, D.; Jacobson, K.; Nir, S.; Isac, T., Phase-Transitions in Phospholipid Vesicles - Fluorescence Polarization and Permeability Measurements Concerning Effect of Temperature and Cholesterol. *Biochim Biophys Acta* **1973**, *311*, 330-348.

35. Deamer, D. W.; Bramhall, J., Permeability of Lipid Bilayers to Water and Ionic Solutes. *Chem Phys Lipids* **1986**, *40*, 167-188.

36. Wunderlich, B.; Leirer, C.; Idzko, A. L.; Keyser, U. F.; Wixforth, A.; Myles, V. M.; Heimburg, T.; Schneider, M. F., Phase-State Dependent Current Fluctuations in Pure Lipid Membranes. *Biophys J* **2009**, *96*, 4592-4597.

37. Elmashak, E. M.; Tsong, T. Y., Ion Selectivity of Temperature-Induced and Electric-Field Induced Pores in Dipalmitoylphosphatidylcholine Vesicles. *Biochemistry-Us* **1985**, *24*, 2884-2888.

38. Tsong, T. Y., Effect of Phase-Transition on Kinetics of Dye Transport in Phospholipid Bilayer Structures. *Biochemistry-Us* **1975**, *14*, 5409-5414.

39. Marsh, D.; Watts, A.; Knowles, P. F., Evidence for Phase Boundary Lipid - Permeability of Tempo-Choline into Dimyristoylphosphatidylcholine Vesicles at Phase-Transition. *Biochemistry-Us* **1976**, *15*, 3570-3578.

40. Pownall, H. J.; Pao, Q.; Hickson, D.; Sparrow, J. T.; Kusserow, S. K.; Massey, J. B., Kinetics and Mechanism of Association of Human-Plasma Apolipoproteins with Dimyristoylphosphatidylcholine - Effect of Protein-Structure and Lipid Clusters on Reaction-Rates. *Biochemistry-Us* **1981**, *20*, 6630-6635.

41. Clerc, S. G.; Thompson, T. E., Permeability of Dimyristoyl Phosphatidylcholine/Dipalmitoyl Phosphatidylcholine Bilayer-Membranes with Coexisting Gel and Liquid-Crystalline Phases. *Biophys J* **1995**, *68*, 2333-2341.

42. Lawaczeck, R., Permeability of Water-Molecules across Vesicular Lipid Bilayers. *J Membrane Biol* **1979**, *51*, 229-261.

43. Cruzeiro-Hansson, L.; Mouritsen, O. G., Passive Ion Permeability of Lipid-Membranes Modeled Via Lipid-Domain Interfacial Area. *Biochim Biophys Acta* **1988**, *944*, 63-72.

44. Nagle, J. F.; Scott, H. L., Lateral Compressibility of Lipid Monolayers and Bilayers Theory of Membrane-Permeability. *Biochim Biophys Acta* **1978**, *513*, 236-243.

45. Doniach, S., Thermodynamic Fluctuations in Phospholipid Bilayers. *J Chem Phys* **1978**, *68*, 4912-4916.

46. Coppock, P. S.; Kindt, J. T., Determination of Phase Transition Temperatures for Atomistic Models of Lipids from Temperature-Dependent Stripe Domain Growth Kinetics. *J Phys Chem B* **2010**, *114*, 11468-11473.

47. Qin, S. S.; Yu, Z. W.; Yu, Y. X., Structural Characterization on the Gel to Liquid-Crystal Phase Transition of Fully Hydrated Dspc and Dspe Bilayers. *J Phys Chem B* **2009**, *113*, 8114-8123.

48. Leekumjorn, S.; Sum, A. K., Molecular Studies of the Gel to Liquid-Crystalline Phase Transition for Fully Hydrated Dppc and Dppe Bilayers. *Bba-Biomembranes* **2007**, *1768*, 354-365.

49. Hong, C.; Tieleman, D. P.; Wang, Y., Microsecond Molecular Dynamics Simulations of Lipid Mixing. *Langmuir* **2014**, *30*, 11993-12001.

50. Li, L. B. B.; Vorobyov, I.; Allen, T. W., The Role of Membrane Thickness in Charged Protein-Lipid Interactions. *Bba-Biomembranes* **2012**, *1818*, 135-145.

51. Winter, N. D.; Schatz, G. C., Coarse-Grained Molecular Dynamics Study of Permeability Enhancement in Dppc Bilayers by Incorporation of Lysolipid. *J Phys Chem B* **2010**, *114*, 5053-5060.

52. Winter, N. D.; Murphy, R. K. J.; O'Halloran, T. V.; Schatz, G. C., Development and Modeling of Arsenic-Trioxide--Loaded Thermosensitive Liposomes for Anticancer Drug Delivery. *J Liposome Res* **2011**, *21*, 106-115.

53. Marrink, S. J.; de Vries, A. H.; Mark, A. E., Coarse Grained Model for Semiquantitative Lipid Simulations. *J Phys Chem B* **2004**, *108*, 750-760.

54. Berendsen, H. J. C., Transport Properties Computed by Linear Response through Weak Coupling to a Bath. In *Computer Simulation in Materials Science: Interatomic Potentials, Simulation Techniques and Applications*, Meyer, M.; Pontikis, V., Eds. Springer Netherlands: Dordrecht, 1991; pp 139-155.

55. Bussi, G.; Donadio, D.; Parrinello, M., Canonical Sampling through Velocity Rescaling. *J Chem Phys* **2007**, *126*.

56. Torrie, G. M.; Valleau, J. P., Non-Physical Sampling Distributions in Monte-Carlo Free-Energy Estimation - Umbrella Sampling. *J Comput Phys* **1977**, *23*, 187-199.

57. Kim, I.; Allen, T. W., Bennett's Acceptance Ratio and Histogram Analysis Methods Enhanced by Umbrella Sampling Along a Reaction Coordinate in Configurational Space. *J Chem Phys* **2012**, *136*.

58. Roux, B., The Calculation of the Potential of Mean Force Using Computer-Simulations. *Comput Phys Commun* **1995**, *91*, 275-282.

59. Souaille, M.; Roux, B., Extension to the Weighted Histogram Analysis Method: Combining Umbrella Sampling with Free Energy Calculations. *Comput Phys Commun* **2001**, *135*, 40-57.

60. Hub, J. S.; de Groot, B. L.; van der Spoel, D., G_Wham-a Free Weighted Histogram Analysis Implementation Including Robust Error and Autocorrelation Estimates. *J Chem Theory Comput* **2010**, *6*, 3713-3720.

61. Walter, A.; Gutknecht, J., Permeability of Small Nonelectrolytes through Lipid Bilayer-Membranes. *J Membrane Biol* **1986**, *90*, 207-217.

62. Swift, R. V.; Amaro, R. E., Back to the Future: Can Physical Models of Passive Membrane Permeability Help Reduce Drug Candidate Attrition and Move Us Beyond Qspr? *Chem Biol Drug Des* **2013**, *81*, 61-71.

63. Parisio, G.; Stocchero, M.; Ferrarini, A., Passive Membrane Permeability: Beyond the Standard Solubility-Diffusion Model. *J Chem Theory Comput* **2013**, *9*, 5236-5246.

64. Van der Spoel, D.; Lindahl, E.; Hess, B.; Groenhof, G.; Mark, A. E.; Berendsen, H. J. C., Gromacs: Fast, Flexible, and Free. *J Comput Chem* **2005**, *26*, 1701-1718.

65. Van Gunsteren, W. F.; Berendsen, H. J. C., A Leap-Frog Algorithm for Stochastic Dynamics. *Mol Simulat* **1988**, *1*, 173-185.

66. Nagle, J. F.; Tristram-Nagle, S., Structure of Lipid Bilayers. *Bba-Rev Biomembranes* **2000**, *1469*, 159-195.

67. Sun, W. J.; Suter, R. M.; Knewtson, M. A.; Worthington, C. R.; Tristram-Nagle, S.; Zhang, R.; Nagle, J. F., Order and Disorder in Fully Hydrated Unoriented Bilayers of Gel-Phase Dipalmitoylphosphatidylcholine. *Phys Rev E* **1994**, *49*, 4665-4676.

68. Safran, S. A., *Statistical Thermodynamics of Surfaces, Interfaces, and Membranes*; Addison-Wesley, Reading, Massachusetts, 1994.

69. Murtola, T.; Rog, T.; Falck, E.; Karttunen, M.; Vattulainen, I., Transient Ordered Domains in Single-Component Phospholipid Bilayers. *Phys Rev Lett* **2006**, *97*.

70. Yang, L.; Kindt, J. T., Line Tension Assists Membrane Permeation at the Transition Temperature in Mixed-Phase Lipid Bilayers. *The Journal of Physical Chemistry B* **2016**, *120*, 11740-11750.

71. Needham, D.; Dewhirst, M. W., The Development and Testing of a New Temperature-Sensitive Drug Delivery System for the Treatment of Solid Tumors. *Adv Drug Deliver Rev* **2001**, *53*, 285-305.

72. Marrink, S. J.; Risselada, H. J.; Yefimov, S.; Tieleman, D. P.; de Vries, A. H., The Martini Force Field: Coarse Grained Model for Biomolecular Simulations. *The Journal of Physical Chemistry B* **2007**, *111*, 7812-7824.

73. Katira, S.; Mandadapu, K. K.; Vaikuntanathan, S.; Smit, B.; Chandler, D., The Order-Disorder Phase Transition in Lipid Bilayers Mediates a Force for Assembly of Transmembrane Proteins. *arXiv preprint arXiv:1506.04298* **2015**.

74. Katira, S.; Mandadapu, K. K.; Vaikuntanathan, S.; Smit, B.; Chandler, D., The Order-Disorder Transition in Model Lipid Bilayers Is a First-Order Hexatic to Liquid Phase Transition. *arXiv preprint arXiv:1506.04310* **2015**.

75. Marrink, S. J.; Risselada, J.; Mark, A. E., Simulation of Gel Phase Formation and Melting in Lipid Bilayers Using a Coarse Grained Model. *Chem Phys Lipids* **2005**, *135*, 223-244.

76. Kastner, J., Umbrella Sampling. *Wires Comput Mol Sci* **2011**, *1*, 932-942.

77. Neale, C.; Bennett, W. F. D.; Tieleman, D. P.; Pomes, R., Statistical Convergence of Equilibrium Properties in Simulations of Molecular Solutes Embedded in Lipid Bilayers. *J Chem Theory Comput* **2011**, *7*, 4175-4188.

78. Uppulury, K.; Coppock, P. S.; Kindt, J. T., Molecular Simulation of the Dppe Lipid Bilayer Gel Phase: Coupling between Molecular Packing Order and Tail Tilt Angle. *J Phys Chem B* **2015**, *119*, 8725-8733.

79. de Vries, A. H.; Yefimov, S.; Mark, A. E.; Marrink, S. J., Molecular Structure of the Lecithin Ripple Phase. *P Natl Acad Sci USA* **2005**, *102*, 5392-5396.

80. Ben-Shaul, A.; Gelbart, W. M., Statistical Thermodynamics of Amphiphile Self-Assembly: Structure and Phase Transitions in Micellar Solutions. In *Micelles, Membranes, Microemulsions, and Monolayers*, Gelbart, W. M.; Ben-Shaul, A.; Roux, D., Eds. Springer New York: New York, NY, 1994; pp 1-104.

81. Kharakoz, D. P.; Shlyapnikova, E. A., Thermodynamics and Kinetics of the Early Steps of Solid-State Nucleation in the Fluid Lipid Bilayer. *J Phys Chem B* **2000**, *104*, 10368-10378.

82. Patel, L. A.; Kindt, J. T., Coarse-Grained Molecular Simulations of the Melting Kinetics of Small Unilamellar Vesicles. *Soft Matter* **2016**, *12*, 1765-1777.

83. Risbo, J.; Jørgensen, K.; Sperotto, M. M.; Mouritsen, O. G., Phase Behavior and Permeability Properties of Phospholipid Bilayers Containing a Short-Chain Phospholipid Permeability Enhancer. *Biochimica et Biophysica Acta (BBA) - Biomembranes* **1997**, *1329*, 85-96.

84. Khavrutskii, I. V.; Gorfe, A. A.; Lu, B. Z.; McCammon, J. A., Free Energy for the Permeation of Na+ and Cl- Ions and Their Ion-Pair through a Zwitterionic Dimyristoyl Phosphatidylcholine Lipid Bilayer by Umbrella Integration with Harmonic Fourier Beads. *J Am Chem Soc* **2009**, *131*, 1706-1716.

85. Petrov, M.; Cwiklik, L.; Jungwirth, P., Interactions of Molecular Ions with Model Phospholipid Membranes. *Collect Czech Chem C* **2011**, *76*, 695-711.

86. Cruzeirohansson, L.; Mouritsen, O. G., Passive Ion Permeability of Lipid-Membranes Modeled Via Lipid-Domain Interfacial Area. *Biochim Biophys Acta* **1988**, *944*, 63-72.

87. Ketterer, B.; Neumcke, B.; Lauger, P., Transport Mechanism of Hydrophobic Ions through Lipid Bilayer Membranes. *J Membrane Biol* **1971**, *5*, 225-&.

88. Graziani, Y.; Livne, A., Water Permeability of Bilayer Lipid-Membranes - Sterol-Lipid Interaction. *J Membrane Biol* **1972**, *7*, 275-&.

89. Benga, G.; Pop, V. I.; Popescu, O.; Borza, V., On Measuring the Diffusional Water Permeability of Human Red-Blood-Cells and Ghosts by Nuclear-Magnetic-Resonance. *J Biochem Bioph Meth* **1990**, *21*, 87-102.

90. Nozaki, Y.; Tanford, C., Proton and Hydroxide Ion Permeability of Phospholipid-Vesicles. *P Natl Acad Sci-Biol* **1981**, *78*, 4324-4328.

91. Levine, Y. K.; Wilkins, M. H. F., Structure of Oriented Lipid Bilayers. *Nature-New Biol* **1971**, *230*, 69-&.

92. Egberts, E.; Marrink, S. J.; Berendsen, H. J. C., Molecular-Dynamics Simulation of a Phospholipid Membrane. *Eur Biophys J Biophy* **1994**, *22*, 423-436.

93. Papahadj.D; Jacobson, K.; Nir, S.; Isac, T., Phase-Transitions in Phospholipid Vesicles - Fluorescence Polarization and Permeability Measurements Concerning Effect of Temperature and Cholesterol. *Biochim Biophys Acta* **1973**, *311*, 330-348.

94. Degier, J.; Mandersl.Jg; Vandeene.Ll, Lipid Composition and Permeability of Liposomes. *Biochim Biophys Acta* **1968**, *150*, 666-&.

95. Singer, M. A.; Finegold, L., Permeability and Morphology of Low-Temperature Phases in Bilayers of Single and of Mixtures of Phosphatidylcholines. *Biochim Biophys Acta* **1985**, *816*, 303-312.

96. Li, L. B.; Vorobyov, I.; Allen, T. W., Potential of Mean Force and Pk(a) Profile Calculation for a Lipid Membrane-Exposed Arginine Side Chain. *J Phys Chem B* **2008**, *112*, 9574-9587.

97. Parsegia.A, Energy of an Ion Crossing a Low Dielectric Membrane - Solutions to 4 Relevant Electrostatic Problems. *Nature* **1969**, *221*, 844-&.

98. Wilson, M. A.; Pohorille, A., Mechanism of Unassisted Ion Transport across Membrane Bilayers. *J Am Chem Soc* **1996**, *118*, 6580-6587.

99. Berger, O.; Edholm, O.; Jahnig, F., Molecular Dynamics Simulations of a Fluid Bilayer of Dipalmitoylphosphatidylcholine at Full Hydration, Constant Pressure, and Constant Temperature. *Biophys J* **1997**, *72*, 2002-2013.

100. Miyamoto, S.; Kollman, P. A., Settle - an Analytical Version of the Shake and Rattle Algorithm for Rigid Water Models. *J Comput Chem* **1992**, *13*, 952-962.

101. Berendsen, H. J. C.; Postma, J. P. M.; Vangunsteren, W. F.; Dinola, A.; Haak, J. R., Molecular-Dynamics with Coupling to an External Bath. *J Chem Phys* **1984**, *81*, 3684-3690.

102. Essmann, U.; Perera, L.; Berkowitz, M. L.; Darden, T.; Lee, H.; Pedersen, L. G., A Smooth Particle Mesh Ewald Method. *J Chem Phys* **1995**, *103*, 8577-8593.

103. Efron, B., 1977 Rietz Lecture - Bootstrap Methods - Another Look at the Jackknife. *Ann Stat* **1979**, *7*, 1-26.

104. Neale, C.; Rodinger, T.; Pomes, R., Equilibrium Exchange Enhances the Convergence Rate of Umbrella Sampling. *Chem Phys Lett* **2008**, *460*, 375-381.

105. Srividya, N.; Muralidharan, S.; Okumu, W.; Tripp, B., Determination of the Line Tension of Giant Vesicles from Pore-Closing Dynamics. *J Phys Chem B* **2008**, *112*, 7147-52.

106. Litster, J. D., Stability of Lipid Bilayers and Red Blood Cell Membranes. *Phys Lett A* **1975**, *53*, 193-194.

107. Zhelev, D. V.; Needham, D., Tension-Stabilized Pores in Giant Vesicles: Determination of Pore Size and Pore Line Tension. *Biochim Biophys Acta* **1993**, *1147*, 89-104.

108. Akinlaja, J.; Sachs, F., The Breakdown of Cell Membranes by Electrical and Mechanical Stress. *Biophys J* **1998**, *75*, 247-54.
109. Melikov, K. C.; Frolov, V. A.; Shcherbakov, A.; Samsonov, A. V.; Chizmadzhev, Y. A.; Chernomordik, L. V., Voltage-Induced Nonconductive Pre-Pores and Metastable Single Pores in Unmodified Planar Lipid Bilayer. *Biophys J* **2001**, *80*, 1829-36.
110. Tekle, E.; Astumian, R. D.; Friauf, W. A.; Chock, P. B., Asymmetric Pore Distribution and Loss of Membrane Lipid in Electroporated Dopc Vesicles. *Biophys J* **2001**, *81*, 960-8.
111. Karatekin, E.; Sandre, O.; Guitouni, H.; Borghi, N.; Puech, P. H.; Brochard-Wyart, F., Cascades of Transient Pores in Giant Vesicles: Line Tension and Transport. *Biophys J* **2003**, *84*, 1734-1749.
112. Rodriguez, N.; Cribier, S.; Pincet, F., Transition from Long- to Short-Lived Transient Pores in Giant Vesicles in an Aqueous Medium. *Phys Rev E Stat Nonlin Soft Matter Phys* **2006**, *74*, 061902.
113. Debregeas, G.; Martin, P.; Brochardwyart, F., Viscous Bursting of Suspended Films. *Phys Rev Lett* **1995**, *75*, 3886-3889.